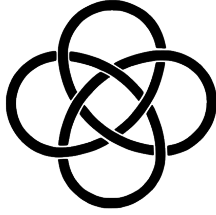


Page left intentionally blank.



The Inter-University Center for Astronomy and Astrophysics

Post Bag 4, Ganeshkhind, Pune, 411007, India

Solar Flares Across the Spectrum: Observations and Instrumentation

A dissertation presented

by

Soumya Roy | সৌম্য রায়

Supervisor: Prof. Durgesh Tripathi

to



Jawaharlal Nehru University, New Delhi, India

in partial fulfilment of the requirements

for the degree of

Doctor of Philosophy

November 2024

*"The first principle is that you must not fool yourself,
and you are the easiest person to fool."*

– Richard P. Feynman

Declaration from Candidate

I hereby declare that the material in the thesis is based on work done at the Inter-University Centre for Astronomy and Astrophysics, Pune. This original thesis has not been submitted previously for any academic cause. The work of other researchers we utilised has been properly cited.

Soumya Roy
IUCAA, Pune, India

Signature: 

Date: 24.11.2024

Declaration from Supervisor

This is to certify that this thesis titled 'Solar Flares Across the Spectrum: Observations and Instrumentation' is based on work done by Mr Soumya Roy at the Inter-University Centre for Astronomy and Astrophysics, Pune, under our supervision. To the best of our knowledge this thesis is original and has not been submitted previously for any academic cause.

Prof. Durgesh Tripathi
IUCAA, Pune, India

Signature: Durgesh Tripathi

Date: 26/11/2024

Declaration from the Head of the Institute

This is to certify that this thesis titled ‘Solar Flares Across the Spectrum: Observations and Instrumentation’ is based on work done by Mr Soumya Roy at the Inter-University Centre for Astronomy and Astrophysics, Pune. To the best of my knowledge this thesis is original and has not been submitted previously for any academic cause.

Prof. R. Srianand
Director, IUCAA, Pune, India



Signature:

Date: **26/11/2024**

R. SRIANAND
Director
Inter-University Centre for
Astronomy and Astrophysics
Pune - 411 007.

Solar Flares Across the Spectrum: Observations and Instrumentation

Abstract

Solar flares are the largest magnetic eruptions in the Solar system. The enigmatic magnetic eruptions have been studied for over a century. However, their complete spectral energy distribution is not yet derived. One of the main missing components is flare energetics in the photosphere and chromosphere. While there are many measurements of flare energetics in the extreme-ultraviolet (EUV), soft and hard X-rays, the measurements in other wavelength bands, especially in the near ultraviolet, are sparse. The Solar Ultraviolet Imaging Telescope (*SUIT*) on board Aditya-L1 by the Indian Space Research Organisation (ISRO) aims to fill the gap by observing the flares in the wavelength band 200 – 400 nm. Moreover, using the EUV and X-ray observations, there has been great progress in flare physics. However, there is a lack in our understanding of the evolution of thermal and non-thermal energy during the course of the evolution of flares and the partition between the thermal and non-thermal energy, including the conversion mechanism at play. This thesis is in two parts. In one part, we perform the initial preparatory analysis carried out for the *SUIT* instrument, including the throughput model, jitter estimation and its effect on imaging, the on-ground spectral and photometric validation, forward modelling of *SUIT* observations using the data obtained from realistic MHD simulations from MURaM, and the stellar calibration plan. We also carry out analysis with existing IRIS data in anticipation of *SUIT*, to comment on the effect of solar flares in the local environment. In the second part, we use the existing EUV and X-ray observations to study the thermal and non-thermal energy in solar flares and demonstrate the importance of volume estimation on the total thermal energy budget and, thereby, the efficiency of the conversion from non-thermal to thermal energy. We propose a triangulation method using existing tools and observations from different vantage points to estimate the volume of emitting plasma in flares as a function of time. Finally, we study two flares which are observed by *SUIT* in NUV combined with EUV, NUV, Soft and Hard X-ray spectroscopy and for the first time we discuss the flare observations and initial results in this broad wavelength coverage.

Contents

CONTENTS

List of Figures

LIST OF FIGURES

List of Tables

List of Publications

Refereed Journal Publications

- "Evolution of the Ratio of Mg II Intensities during Solar Flares", **Soumya Roy** and Durgesh Tripathi, 2024, ApJ, 964, 106, doi: [10.3847/1538-4357/ad2a46](https://doi.org/10.3847/1538-4357/ad2a46)*
- "Near and Mid-ultraviolet Observations of X-6.3 Flare on 2024 February 22 Recorded by the Solar Ultraviolet Imaging Telescope on board Aditya-L1", **Soumya Roy**, Durgesh, Tripathi, Sreejith, P, & Ramaprkash, A. N., et. al., 2024, ApJL, 981, L19, doi:[10.3847/2041-8213/adb0be](https://doi.org/10.3847/2041-8213/adb0be)*
- "Photometric Calibration & Spectral Validation of the Solar Ultraviolet Imaging Telescope onboard Aditya-L1", Janmejoy Sarkar, **Soumya Roy**, A. N. Ramaprkash,... 2024, J. Astron. Telesc. Instrum. Syst. 11(1), 014005 (2025), doi:[10.1117/1.JATIS.11.1.014005](https://doi.org/10.1117/1.JATIS.11.1.014005)*
- "Science Filter Characterization of the Solar Ultraviolet Imaging Telescope (SUIT) on board Aditya-L1", Janmejoy Sarkar, Rushikesh Deogaonkar, Ravi Kesharwani, ... **Soumya Roy**,... 2024, Exp. Astron., 59, 3 (2025), doi: [10.1007/s10686-024-09973-5](https://doi.org/10.1007/s10686-024-09973-5)
- "Solar Ultraviolet Imaging Telescope on board Aditya-L1", Durgesh Tripathi, A. N. Ramaprkash, Sreejith P,... **Soumya Roy**,... 2025, Sol. Phys., 300, 30, [10.1007/s11207-025-02423-1](https://doi.org/10.1007/s11207-025-02423-1)*
- "X-class flare on Dec 31, 2023, observed by the Solar Ultraviolet Imaging Telescope", **Soumya Roy**, Durgesh Tripathi, Sreejith P, & A. N. Ramaprkash, et. al., 2025, ApJL, 983, L6, [10.3847/2041-8213/adc387](https://doi.org/10.3847/2041-8213/adc387)
- "Test and Calibration of the Solar Ultraviolet Imaging Telescope (SUIT) on board Aditya-L1", Janmejoy Sarkar, Nived V. N., **Soumya Roy**, Rushikesh Deogaonkar et al., 2025, Accepted for publication in Sol. Phys.

Submitted Articles

- "Evolution of thermal and cumulative non-thermal energy in solar flares", **Soumya Roy**, Sophie Musset, Katharine K. Reeves, Durgesh Tripathi, Christopher S. Moore, 2024, Submitted to ApJ*

*Part of this thesis

CHAPTER 0. LIST OF PUBLICATIONS

- "Forward Modeling Observations of the Solar Ultraviolet Imaging Telescope (SUIT) on board Aditya-L1", **Soumya Roy**, L. S. Anusha, Durgesh Tripathi, et al. 2024, Submitted to ApJ*

Technical Documents

- Roy, S., et al., "Solar Ultraviolet Imaging Telescope (SUIT) Handbook", ISRO Aditya-L1 mission
- Roy, S., et al., "Estimation of Effects of Space-craft Jitter on SUIT Imaging", ISRO Aditya-L1 mission*

*Part of this thesis

List of Abbreviations

AIA	Atmospheric Imaging Assembly
SDO	Solar Dynamic Observatory
EUV	Extreme Ultra Violet
HMI	Helioseismic and Magnetic Imager
IRIS	Interface Region Imaging Spectrograph
EUI	Extreme Ultraviolet Imager
SUIT	Solar Ultraviolet Imaging Telescope
STIX	the Spectrometer/Telescope for Imaging X-ray
ISRO	Indian Space Research Organisation
URSC	U R Rao Satellite Centre
IMaX	Imaging Magnetograph eXperiment
SuFI	SUNRISE Filter Imager
QS	Quite Sun
CH	Coronal Hole
AR	Active Region
TR	Transition Region
DEM	Differential Emission Measure
EM	Emission Measure
LTE	Local Thermodynamical Equilibrium
FoV	Field of View
RoI	Region of Interest
LoS	Line of Sight
FWHM	Full Width Half Maxima
MURaM	MPS/ University of Chicago Radiative MHD
CME	Coronal Mass Ejection

Acknowledgments

The journey of a PhD is like a marathon. There are times when you feel like sprinting down the lane, full of energy, driven by small successes, getting stuck on something for a while, and finally finding that "eureka" moment. Other times, you feel out of breath, barely dragging your legs along, just trying to stand. I believe what matters most are the connections you make with people who push you and help you during those difficult moments because without them, I wouldn't be here writing this acknowledgment!

First, I would like to thank Durgesh; this thesis would not have been possible without his guidance. He gave me enough freedom to explore whatever I wanted, offering valuable suggestions along the way but never giving "orders." More importantly, he carefully considered any differing viewpoints I raised from the first day. Without this freedom, I probably wouldn't be as proud of my growth over the past five years. Very few people get the opportunity to contribute to one of their country's first major observatory-class missions. I am especially grateful for the confidence he and Ram placed not only in me but also in several other young students while realizing SUIT. While I worked on the project for only five years, I also want to thank everyone who was part of it before me without their hard work, I would not have been able to take over so easily.

Next, I would like to thank Kathy. Just like Durgesh, she also allowed me the freedom to explore the problems I was given, nudging me in the right direction whenever I got stuck. I also want to thank Chris. His enthusiasm in answering my questions and our discussions on various topics were invaluable. Working at CfA was a remarkable experience. I am grateful to Kathy, Durgesh, the Smithsonian Institution, and CfA for making this possible. Experiencing the life of a graduate student in two very different systems gave me insight into both the challenges and advantages of each. Beyond being a scientific opportunity, it was a profound lesson in becoming an independent person not just a "scientist". Leaving your country and loved ones after twenty-six years to live alone, work, cook, and function as an independent adult in a foreign country is not easy. But those one-and-a-half years helped me mature quickly.

Our memories of a place are deeply tied to the people and the experiences we share with them. I want to thank Tatiana and Chad specifically; I will forever cherish the fun we had in the chess club. Those library gatherings early on at CfA were something I looked forward to when I had not yet made many friends. Tatiana, you were a godsend! As someone who isn't very extroverted, you made it easy for me to open up to people at CfA. I also want to thank several people involved in the HSO-Connect project, with whom I had many fruitful academic and non-academic discussions: Sophie, Dana, Ritesh, Xiaoyan, Crisel, Dan, Sam, and Yeimy. Similarly, my time at IUCAA became equally memorable, thanks to many people whether we were traveling, hiking, playing board games and football, cooking together, or organizing Diwali celebrations for two years in a row.

CHAPTER 0. ACKNOWLEDGMENTS

In the early days, I spent a lot of time with Sunil and Sorabh playing FIFA in my room or on the pantry TV. It was a relief to know I wasn't the only one "wasting" time on "silly video games"! Tathagata, Suprovo, Sorabh, Sunil, Somak Da, Sourabh, Suraj, Dhruv, we spent so much time playing board games I had not even known existed. Ankush, Partha, Biku, Kavita, and Meenakshi, our cooking sessions and hangouts were respites I looked forward to. A special shout out to the football gang - Sunil, Sorabh, Somak Da, Sayak, and Soumil. Thanks to you all, we managed to follow football regularly, despite our busy schedules.

I also thank the solar group and its wonderful members for both academic and non-academic discussions over the years: Nived, Vishal, Janmejoy, Megha, Sneha, Rushikesh, Rahul, Sreejith, Abhishek, Deepak, Sargam, and Avyarthana. Megha and Anirban felt like older siblings I could always approach when needed.

A special shout-out to Nived! Although we didn't spend much time together, I had more scientific discussions with you than anyone else. I respected your opinions so much that I started running every crazy idea by you first. Your constant presence in my scientific journey has been invaluable.

Special thanks to Lindsay Glesener. Many people never realize the impact they can have on others. During the 2023 SF AGU meeting, Chris took me with his group to Berkeley to see the FOXSI-4 assembled. At the time, I was at a low point, doubting my ability to succeed in academia and considering leaving after my PhD. Lindsay shared how, as a PhD student, she accidentally destroyed the CCD hours before the FOXSI-1 launch, delaying it. Despite that, she went on to become the PI of FOXSI-4. Her story rekindled my confidence. Lindsay, I may never tell you this in person, but however long I stay in academia, your story will remain a key source of inspiration.

I am deeply grateful to my professors at Presidency University, Kolkata – Suchetana and Ritaban for their support during my bachelors and masters programs. Without them, I might not have pursued a PhD in astronomy.

This work would not have been possible without the support of my family and friends. I owe my career in physics to the enthusiasm and encouragement of my uncle, Maloy Kumar Roy, and my friend's father, Ranjan Basak. My uncle Shyamal Kumar Ray has been a constant companion, whether watching football or movies together. Aloke Mitra has been a lifelong pillar of support. Sayan Chakraborty, who started as my teacher, gave me the coding skills that became invaluable during my PhD.

Finally, I want to thank my parents. They gave me the freedom to explore whatever I wanted from a very early age. After high school, they supported my decision to pursue a career in basic science, even when friends and relatives were skeptical.

This thesis would not have been possible without the open data policies of several instruments. I acknowledge the use of data from AIA, HMI, IRIS, XRT, STIX, Chandrayaan-2/XSM, Stereo-A, GOES/XRS, and GOES/SUVI. I also thank the SUIT and Pegasus

CHAPTER 0. ACKNOWLEDGMENTS

servers at IUCAA for providing computational facilities.

*Dedicated to everyone who pushed me one step at a time,
every time I was about to give up!*

And to my younger self, who was brave enough to embark on this journey...

Chapter 1

Introduction

The Sun is our nearest astrophysical object, which serves as a natural laboratory for various branches of Physics - atomic physics, spectroscopy, turbulence, magneto-hydrodynamics, stellar evolution, dynamo and magnetism and plays a key role in space and terrestrial weather. The Sun is also the primary source of light and energy on Earth. So it is only natural that we try to understand the different physical processes involved in the energetics of the Sun, which directly affects life on Earth. In this chapter, I briefly introduce the Sun, various layers of its atmosphere and solar flares. Finally, we provide a motivation for the thesis and a brief outline.

1.1 The Sun

The Sun is a G2V star, with surface luminosity 3.86×10^{26} W and an effective temperature of ~ 5780 K. The Sun is mostly made out of Hydrogen (92.1%) and Helium (7.8%), along with negligible quantities of heavier elements C, N, O, Mg, Si, Ne and Fe, among others. The study of the Sun can be divided into three components, *viz.* the solar interior, the solar atmosphere and the Heliosphere. Fig. ?? shows a schematic diagram of various regions of the Sun. Below, we briefly describe these three regions.

1.2 The Solar Interior

Depending on various physical characteristics, the solar interior can be divided into three zones *e.g.* the core, radiative zone and convective zone. In the innermost zone, the core, the Sun has a temperature of about 15 MK and a density of 1.6×10^5 km.m⁻³. Here Hydrogen fuses into Helium primarily by p-p chain reaction (?) and to some extent by CNO cycle (?). Beyond the core, we have the optically thick radiative zone, where the Hydrogen and Helium are completely ionized due to very high density. The high energy γ -ray photons generated

in the core have a very small mean free path in this region, as they collide numerous times and propagate across this region. As we move radially outwards, temperature and density both decrease slowly due to gravitational equilibrium. Due to this reduction of temperature, there is a decrease in the thermal motion of the particles, and the hydrogen and helium start to recombine, giving rise to an increase in opacity at the top of the radiative zone. This change in opacity makes the propagation of photons via radiation less efficient, as photons get trapped and reabsorbed more. This creates a sharp temperature gradient due to the "photon pileup". This temperature gradient gives rise "convective instability". This is the convective zone where the energy from the inner layers of the Sun is transported adiabatically to the surface of the Sun.

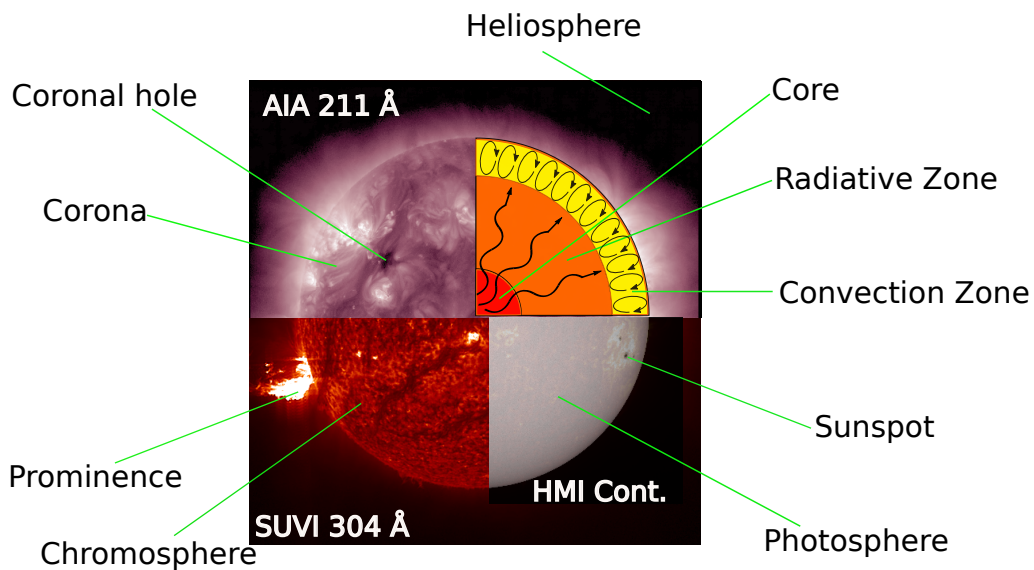


Figure 1.1: A schematic depiction of the different regions of the Sun, including some of the most prominent magnetic structures on the Sun e.g., Sunspot, prominence, coronal hole.

The core and the radiative zone of the Sun rotate as a solid body, whereas the convective zone rotates deferentially. The rotation period varies from ~ 25 days to ~ 35 days from the equator to the pole.

1.3 The Solar Atmosphere

The layers outside the convection zone together form the solar atmosphere and is further divided into different regions. The photosphere, which is also known as the Sun's surface, the chromosphere, the transition region and the corona. While we can define geometrical height or depths to define these layers, it is much more useful to define them using the local optical depths of various spectral lines, which are directly used to observe the layers. This also gives us an idea about which spectral features originate mainly from which portions

of the solar atmosphere. Fig. ?? shows the variation of temperature and number density across various layers of the solar atmosphere (?).

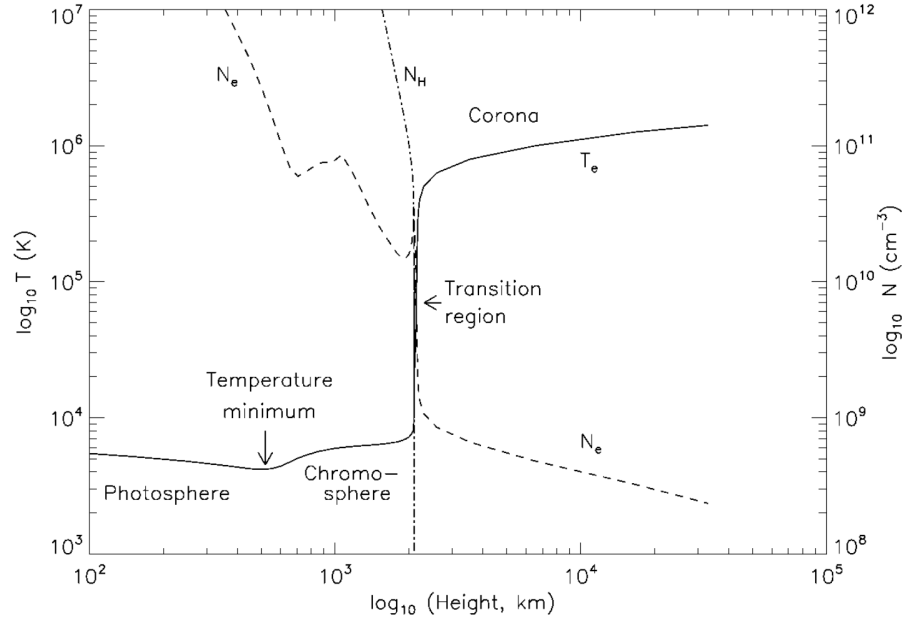


Figure 1.2: The variation of electron temperature (solid line) and electron density (N_e , dashed line) and density of neutral hydrogen atoms (N_H , dot-dashed line) in the solar atmosphere (?).

1.3.1 The Photosphere

The photosphere is defined to be the layer where $\tau_\lambda \sim 5500 = 1$. This is in the green part of the visible spectrum and the Sun is opaque in visible beyond this layer, hence it is called to be the surface of the Sun. This layer is 400–600 km thick and has an effective temperature of ~ 5780 K. The magnetic field lines arising from the tachocline penetrate the photosphere and create a ‘carpet’ over the whole region (?). As mentioned earlier, this is the solar surface known as the ‘quiet Sun’ (QS). This region exhibits an average magnetic flux density of 10–50 G. The QS surface is covered with cells of roughly four sizes, namely, granules, mesogranules, supergranules and giant cells.

Some regions exhibit much stronger magnetic flux density, often associated with highly twisted magnetic field structures. These magnetic features are manifested as Sunspots. The Sunspots harbour some of the strongest concentrated magnetic fields, reaching up to several kilogauss in strength. The other noteworthy solar magnetic structure apart from these are believed to be spatially unresolved flux tubes composing a network with field strengths $\sim O(10^3 G)$ (??).

As the density changes drastically at the photosphere compared to the convective zone,

the thermalized photons from the Sun’s core start free streaming, as the mean free path also increases drastically and, as a result, perturbs the thermal equilibrium (TE). Therefore, the thermodynamic quantities of the photosphere are defined under the assumption of Local Thermal Equilibrium (LTE). As we move higher from the photosphere, the LTE conditions also start deviating because the density keeps on decreasing steadily (?).

1.3.2 The Chromosphere

The chromosphere is a highly non-uniform dynamic layer with a thickness of 1500–3000 km, with increasing temperature (up to 10^4 K) and decreasing number density. As seen in Fig. ??, the temperature of the chromosphere saturates before the dramatic rise in the transition region. This saturation is attributed to a steady deposition of acoustic energy by the creation of shock waves (?). The chromosphere also exhibits a sharp gradient in the plasma β factor, non-LTE conditions, and the dominance of wave motions. The observable features in the chromosphere are active regions, sunspots, plages and also light bridges as labelled in images taken by IRIS SJI (slit-jaw imager) 2796 Å (left panel) and 2832 Å (right panel) displayed in Fig. ??.

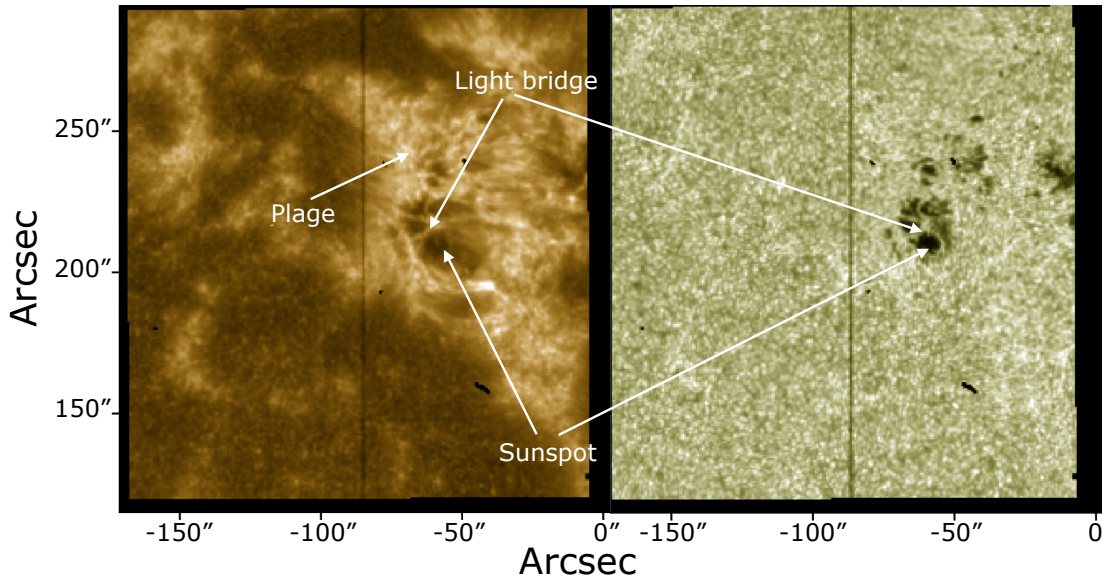


Figure 1.3: IRIS slit-jaw images of NOAA AR 13521 taken in Mg II 2796 Å (left panel) and 2832 Å continuum (right panel) showing the upper chromosphere and upper photosphere, respectively. Different features are labelled.

1.3.3 The Transition Region

The transition region above the chromosphere is a thin, dynamic layer where we witness a dramatic increase in temperature by two orders of magnitude along with a similar decrease in electron density, demonstrated in Fig. ???. In general, this layer is roughly ~ 100 km in thickness, but that can change depending on various dynamic conditions of chromosphere ($\sim 10^4$ K) below, and corona ($\sim 10^6$ K) on top. The transition region is generally characterized by steep changes in temperature, pressure gradients, local optical depth, and competition between gas and magnetic pressure. The transition region also manifests the ARs as various magnetic features such as small-scale brightening, jets, spicules, fibrils etc.

1.3.4 The Corona

The outermost layer of the atmosphere is the corona. The corona maintains a temperature of 1-2 MK during ambient conditions but can rise up to tens of MK during explosive eruptions such as solar flares. Due to such high temperatures, the coronal gas is fully ionized. It is only visible to the naked eye during the total solar eclipse or with coronagraphs due to Thomson scattering of the photospheric visible photons with free electrons in the corona. Corona also emits in various emission lines of e.g. Mg, Fe, Si, S, Ca, O, etc. and their ions, across a wide band of electromagnetic spectrum ranging from X-ray to visible wavelengths. Similar to the other layers, the corona exhibits a variety of structures such as ARs, coronal holes, bright points, filaments, and flares. The flare arcades are most prominently visible in the corona.

1.4 Solar Flares

solar flares are the most powerful energetic explosions in the solar system. They are described as a sudden increase in brightness in localized areas of the Sun. Within tens of minutes, they can release over 10^{32} erg of energy, which is emitted across the entire electromagnetic spectrum, i.e., from radio to gamma rays. They can also launch highly energetic particles into the interplanetary medium. Flares occur in magnetic active regions. It has been estimated that the amount of flare energy released is comparable to the free energy stored in the magnetic system (??). The total energy released varies from event to event. It is also known that larger events occur much less frequently than smaller events.

Fig. ?? displays one of the most well-known and well-studied solar eruptions from Aug 31st, 2012. During this event, an associated giant prominence erupted from the southeast limb, which was visible in all AIA channels as shown in Fig. ???. The sunspots are also clearly visible and labelled in the HMI continuum (see Fig. ??h). In Fig. ??i, we show the co-aligned AIA 304 Å and HMI continuum observation. The prominences are rooted at the sunspot penumbra, accompanied by the hot thermal plasma associated with the accompanying flare

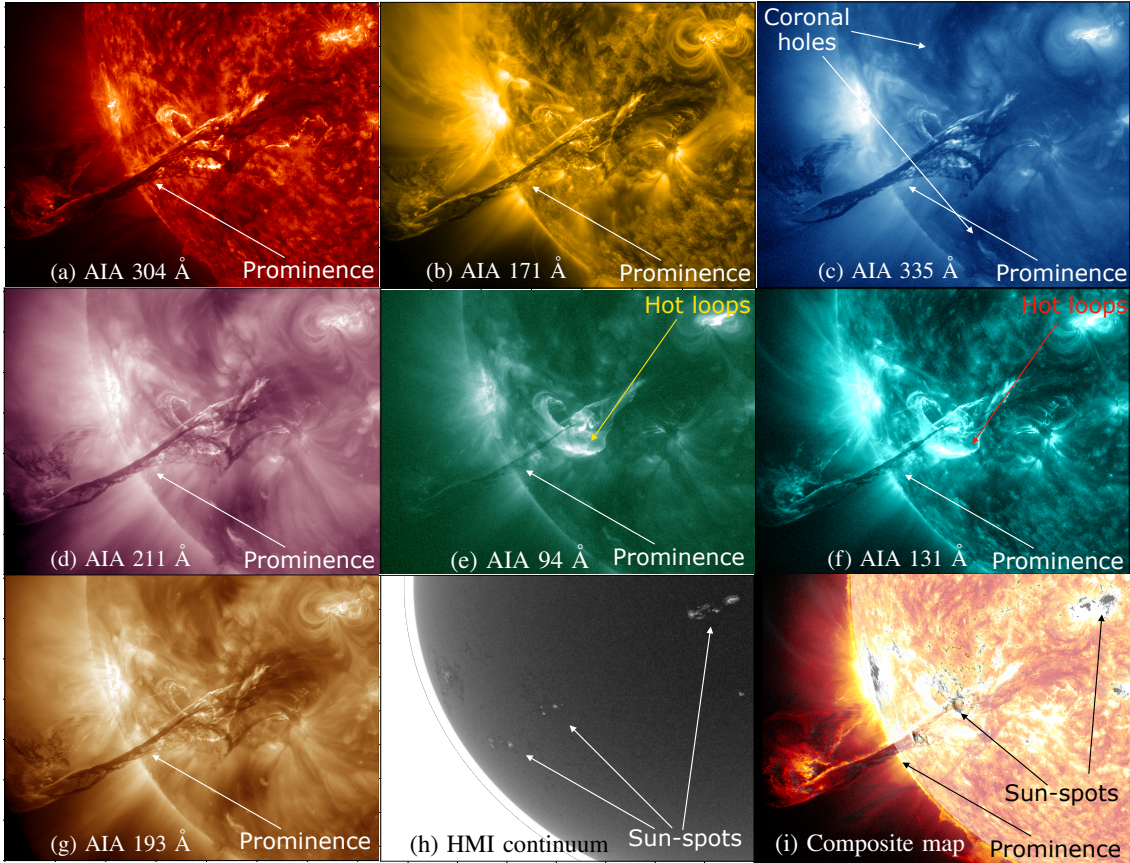


Figure 1.4: AIA observations of prominence eruption and associated flare as observed on Aug 31st, 2012~19:50 UT. Different features across different wavelengths have been labelled.

(visible in Fig. ?? e – f). The novelty of such observation lies in the clear spatial connection across various layers of the Sun, connected via energy and momentum transported from one layer to the other.

1.4.1 Brief history of flare observation

On September 1, 1859, R.C. Carrington and R. Hodgson independently observed the first flare in white-light continuum (??). Such localized brightening on the Sun has remained an enigma ever since. Shortly after the observation by Carrington and Hodgson, the Sun was being studied extensively in the H α wavelength, which essentially images the chromosphere, and the reports of flaring events became increasingly frequent and progressively more complex. No two events were similar, as there were variations observed in the size of the source, ejections of plasma, and shock waves driving into the interplanetary space. Advances in radio technology during the Second World War affirmed the detection of the

CHAPTER 1. INTRODUCTION

presence of non-thermal electrons in the solar corona during military radar operations (?). Around the same time, S.E. Forbrush noticed ground-level cosmic ray enhancement during major solar flares. These discoveries eluded that the flaring events do not only involve the thermal plasma but somehow connect with high energy particles and involve the corona.

In the late 1950s, using rockets and balloons, the Sun was observed in hard X-rays ($\geq 10 \text{ keV}$). ? discovered the first hard X-ray emission during a flare in 1958. Later on, it was deduced from the enhancements observed in radio and hard X-rays that the ejected energetic particles may contain a substantial fraction of the initial energy released (?). Note that while the hard X-ray is created by the bremsstrahlung radiation of the electrons colliding into dense material, resulting in a power-law energy distribution, the broadband radio emission from 1 to 100 GHz is created from gyrosynchrotron emission. Flares are now routinely observed with different space-borne instruments, in particular in the EUV and soft X-ray($\leq 10 \text{ keV}$), which shows that the energy released from the flare heats the local plasma to temperatures beyond 30 MK.

? observed a curious correlation that the soft X-ray flux during the rising phase of the flare is proportional to the time integral of the centimetre radio flux since the start of the flare, suggesting a correlation between thermal plasma and the energetic electrons. Note that the centimetre radio flux is emitted by relativistic electrons. A similar correlation was found between the hard X-ray and soft X-ray flux later on. Such correlation can be expressed as,

$$F_{SXR}(t) \propto \int_{t_0}^t F_{HXR}(t') dt' \quad (1.1)$$

and is known as the “Neupert effect”. This relationship shows that the soft X-ray radiation primarily originates from a thermal plasma which is heated by the energy of the flaring event deposited by the accelerated electrons. We note, however, that Eqn. ?? is only valid if cooling by conduction is negligible and/or the role of ions in the flare energy deposition is minimal (?).

1.4.2 “Standard” model of solar flare

Based on various multi-wavelength studies of solar flares, combined with theoretical modelling a ‘standard’ model of solar flares has been advocated by ?????, and termed as *CSHKP* model. The flares occur due to the abrupt release of magnetic free energy, which was previously stored in the coronal magnetic field via flux emergence and surface motions (?). The majority of the strongest flares are eruptive in nature. The ‘standard’ model attributes the release of flare energy to magnetic reconnection in the corona, which happens due to the eruption and/or coronal mass ejection (????). It is noteworthy that, despite continuous attempts over the decades, this is not at all a quantitative model. Rather, it is an attempt to unify the multi-wavelength observations and modelling attempts in an orderly

CHAPTER 1. INTRODUCTION

manner. Naturally, the model can not explain all the observations from various flares. A schematic picture of the model is shown in Fig. ???. Below we describe the salient points of the ‘standard’ model:

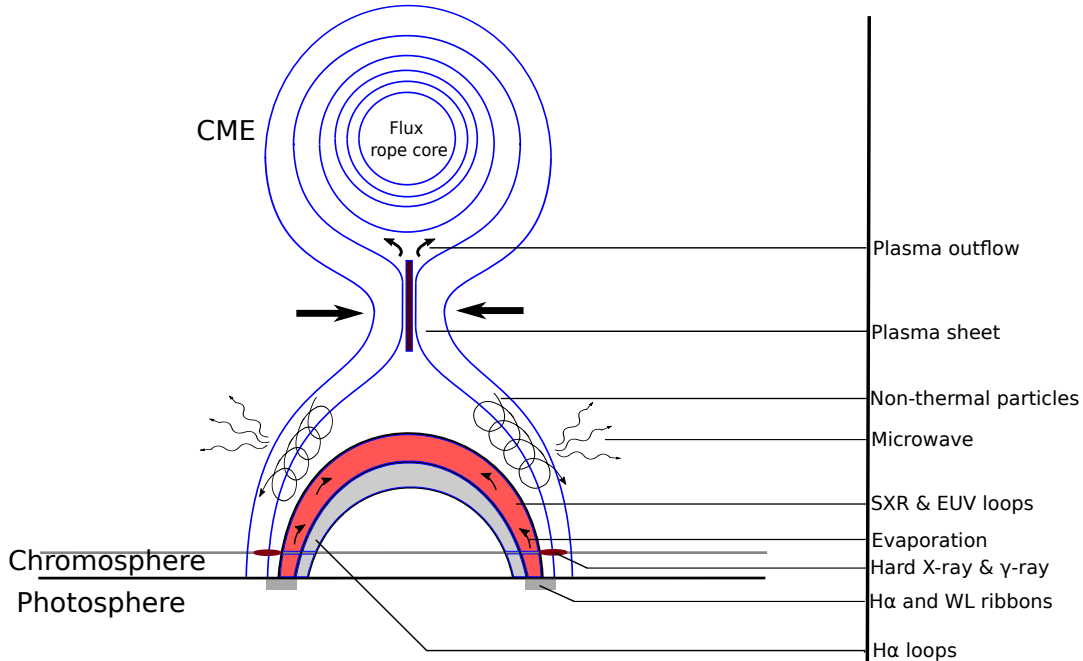


Figure 1.5: A schematic diagram of the standard model of solar flare.

1. In the standard model, following the reconnection event that releases the magnetic free energy, electrons and ions from the reconnection site are accelerated along the realigned magnetic field lines downwards. In the case of an associated CME, parts of the magnetic energy is deposited as kinetic energy. The coronal reconnection source where the energy is released is often observed in HXR. The loop-top HXR sources are often accompanied by the thermal SXR sources. The loop top HXR source is observed above the coronal SXR source (?).
2. The accelerated particles move along the field lines downwards along the magnetic field lines, giving rise to the microwave and radio observations seen from flares via gyro magnetic radiation at various frequencies dictated by the characteristics of local plasma. Finally, the accelerated particles hit the chromosphere, which is considerably denser than the corona, giving rise to Hard X-rays and sometimes also gamma-rays observed from the foot points. This also explains why the coronal hard X-ray source is considerably softer than the foot points. The energetic particles deposit their energy into the local chromosphere as they go through a series of collisions and eventually thermalize (?). Foot point sources are occasionally detected on H-alpha flare ribbons

CHAPTER 1. INTRODUCTION

marking the base of a magnetic arcade (?). The ribbon brightening is usually observed to propagate along the ribbons while they separate further from each other, signifying continued reconnection (?).

3. γ -ray emission from solar flares is visible between 0.8 – 20 MeV generated by the accelerated ions. The neutron capture line at 2.2 MeV forming Deuterium is usually the strongest characteristic line visible from such emissions. Flare-accelerated protons and ions colliding with the dense chromosphere can produce neutrons. It is suggested that these neutrons are captured by ambient protons to form Deuteron, giving rise to the 2.2 MeV characteristic bump (??). Later, RHESSI observations (??) showed that the γ -ray foot-points did not coincide with the HXR foot-points. This demonstrated that the ions and electrons were accelerated differently, as proposed by ?.
4. The thermalized plasma emits in thermal bremsstrahlung, giving rise to soft X-ray and EUV radiation. The heating of the local chromosphere increases the local pressure. When the growing pressure gradient builds up enough, the local plasma expands upwards and fills up the coronal loops with soft X-ray-emitting plasma. This phenomenon is known as "chromospheric evaporation". This was first reported by ???. ? reported velocities of 300 – 400 km/s with temperature \sim 20 MK in Ca XIX, while later on ? reported much gentler up-flow with velocities \sim 200 km/s in Fe XIX line from *SOHO/CDS* observations. Several simulations also reproduced evaporation arising from non-thermal particle precipitation (???).

It is important to emphasise that while the standard model attempts to explain and unify various kinds of differences seen from the numerous flares we observe, there are several cases where the standard model cannot explain the observations. For example, there have been observations of flares where the hard X-ray footpoint does not form (??). It is proposed that in these cases, the plasma in the coronal loops is so dense that the accelerated particles pass through enough collisions to thermalize within the flare loops before reaching the chromosphere. In this process, they may defuse the energy more evenly within the loop rather than impulsively dumping it at the base of the loops. Another flare which previously occurred at the same region might explain the denser coronal loops (??).

1.5 Motivation of the thesis: the energetics of solar flares

Given the rich history of flare observations over more than 150 years, we have learnt a lot about their charactershtics and dyamics. However, there are several complexities involved in the physics of solar flares, which are still fully understood. The reconfiguration of the magnetic structures, which almost always involves complex geometry, makes almost all events unique in some sense. Following the reconfiguration of the magnetic field, the released magnetic free energy is transported across various layers of the Sun and converted

CHAPTER 1. INTRODUCTION

into various other forms of energy. The overarching conversion of magnetic energy into various forms, i.e., reconnection outflow, particle acceleration, thermal and kinetic energy of chromospheric plasma, etc., has proven incredibly complex to model. In cases where flares are associated with eruptions, e.g., CMEs, there is the added complexity of the kinetic and potential energy of the CMEs, the associated shocks and the kinetic energy of the solar energetic particles.

To constrain the models of solar flares and the various associated phenomena, detailed quantitative characterization is absolutely necessary. The questions which are of particular importance are:

- Do active regions have enough free energy to account for the total energy released in the solar flares and their associated phenomena?
- What is the energy partition between flares and CMEs?
- Do the non-thermal component of flares have enough energy to completely power the thermal component or an extra energy source is required to power the thermal component?

While it is now established the active regions have enough magnetic free energy to power the flare and CME and other associated phenomena (??), the energy partition between the flare and associated CME is much more fuzzy. ? found that the flare and CME have energies of the same order of magnitude, while ? concluded the energy in the flare dominates that of the associated CME.

The question about the non-thermal component having sufficient energy to power the thermal component is still unresolved, as even the most recent studies contradict each other in the most puzzling fashion. ? discussed the contradictions arising from some of the studies (??????), the details of which are summarized in Table ??.

Study	No. of flares	GOES class range	Thermal model	Thermal spectrum	Thermal volume	Thermal losses
? (S07 from hereon)	18	A3-B7	Isotherm.	RHESSI	TRACE	X
? (E12 from hereon)	38	C5-X28	Isotherm.	RHESSI	RHESSI	Rad.
? (IC14 from hereon)	10	B3-B9	Multitherm.	RHESSI+AIA	RHESSI	Rad.
?? (WM16 from here on)	24	C3-X17	Isotherm.	RHESSI+GOES	RHESSI	Rad.,Cond.
? (A17 from here on)	188	M1-X7	Multitherm.	AIA	AIA	Rad.

Table 1.1:: Observational summary of the flares as described in ?.

The bolometric energy serves as a representation of the overall energy released during solar flares. Regardless of the mechanism of energy release, e.g., through direct plasma heating, rapid bulk flows, or non-thermal particles, etc., the ultimate outcome is the thermalization of the plasma and the subsequent radiation. Since the bolometric energy encompasses the entire electromagnetic spectrum, it reflects the total energy originally of the flare. Note, however, that this bolometric energy only pertains to the energy liberated within the flare and does not include the energy associated with the concurrent CME.

CHAPTER 1. INTRODUCTION

Fig. ?? displays correlation plots between peak thermal energy and peak GOES flux (left panel) for various flares studied by various authors and corresponding (where available) volume estimates of the thermal plasma (right panel). The plots show that the estimated thermal energy obtained in all studies shows an excellent correlation with peak *GOES* flux. Also plotted are the bolometric energies obtained by ???. Note that the thermal energy obtained by E12 (open red diamonds) and WM16 (filled black circles) are consistently one order of magnitude lower than the bolometric energy (open green diamonds and solid green line) of flares with similar peak GOES flux. Extrapolation of E12 and WM16 is about half an order of magnitude lower compared to IC14 (open blue triangles), while S07 (open pink flipped triangles) is very consistent with the extrapolation. Note that the energies estimated in A17 (orange plus signs) are about an order of magnitude higher than that obtained in other studies and even higher than the extrapolated bolometric energy for flares of the same class from ? and E12.

The above described results present a contradiction in the results obtained in different studies. While there could be several reasons for these differences, they can be attributed to differences in modelling the thermal component of the flares. For example, *RHESSI* usually yields a higher temperature and lower emission measure compared to *GOES* due to the highly multi-thermal nature of the flaring plasma (???). Although the *GOES* temperature is higher by a factor of 1.4, it is not dependent on the flare class. Moreover, ? also investigated whether assuming an isothermal or multi-thermal model introduces any differences in the thermal energy estimates. They reported no significant differences due to differences in models (refer to Fig.2 and the corresponding discussion in ?). Notably, these comparisons of isothermal and models are made by fitting spectra obtained by spatially binning spectra. This does not really incorporate the multithermal nature of the plasma varying spatially.

The thermal energy is estimated using

$$U_{Th} \sim n_e k_B T V f$$

where n_e is the electron density, k_B is Boltzmann's constant, T is the temperature, V is the volume of the flaring plasma, and f is the filling factor.

Fig. ?? right panel shows the volumes used for various studies to estimate the thermal energy as a function of the peak *GOES* flux. Apart from S07 and A17, all other studies used *RHESSI* imaging to estimate the flare volume with a filling factor $f = 1$. S07 determined the volume by employing a semicircular loop model, utilizing the cross-sectional area and loop length derived from the observed areas and separations of foot point brightening of 1600 Å by *TRACE*. In contrast, A17 estimated the volume based on the flare area exceeding a certain threshold in the emission measure obtained from the spatial synthesis DEM method.

It is worth noting that the volume estimates from E12 and WM16 align closely, as do those from A+17, despite employing entirely different methodologies. In contrast, the micro flare volumes reported by IC14 are notably larger, ranging from one to two orders of magnitude beyond what would be anticipated based on the findings of the other four

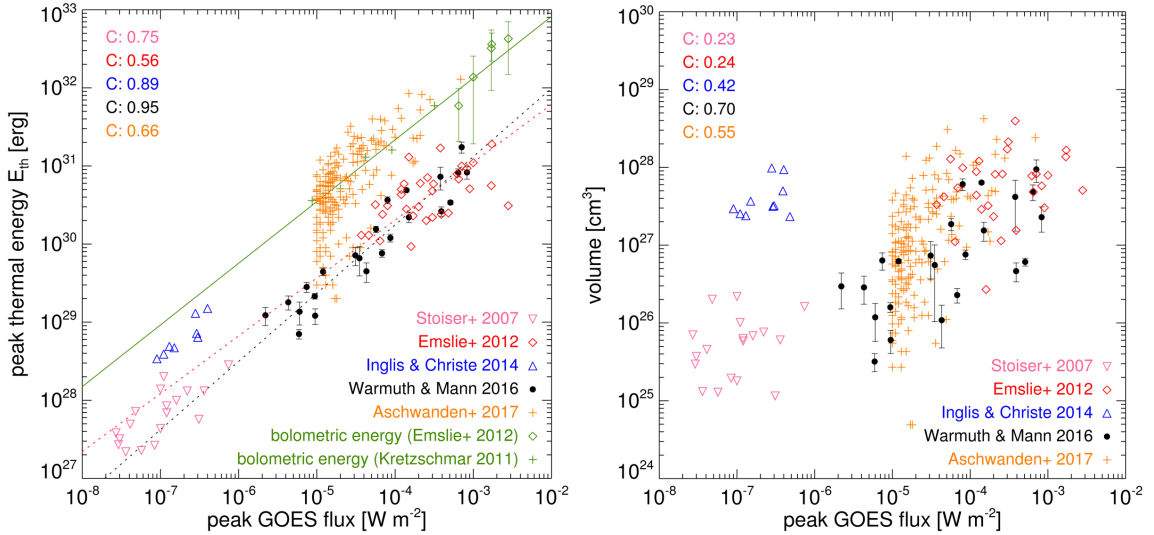


Figure 1.6: *GOES* peak thermal energy (left panel) and volume of the thermal plasma (right panel) as a function of the peak *GOES* flux for all the flares from five studies (figure credit: ?). The C values show the linear correlation coefficient for various studies.

studies. Intriguingly, this discrepancy aligns with the additional volume required to account for the higher thermal energies observed in IC14. The uncertainty in detecting volume can be due to the CLEAN (Component Least Squares Deconvolution) algorithm systematically overestimating the source size (?). There have also been studies demonstrating that *RHESSI* has difficulties in resolving small sources (??), that would be applicable for small thermal sources in the microflares.

From the above-described studies, it is clear that there are number of questions that are crucial to describe the physics of solar flares. We allude to these below.

- The primary challenge in estimating the thermal energy of the hot plasma stems from determining the temperature distribution of the plasma using Differential Emission Measure (DEM), and the radiating plasma volume. How strongly do the uncertainties of determining the thermal energy depend on the uncertainties of the volume estimation and the highly mutithermal nature of the flaring plasma?
- The dissipation of energy from the hot plasma is substantial. Although there is widespread agreement regarding radiative losses across studies, the extent of conductive losses disagree significantly between the studies. Why do various studies vary so significantly on the extent of conductive losses across the literature and what effect does it have on the thermal evolution of the flares?
- How much do the non-thermal energy in injected electrons depend on the poorly constrained low-energy cutoff?

CHAPTER 1. INTRODUCTION

- The thermal and non-thermal energy partition changes with flare class. In smaller flares, there appears to be a deficiency of energetic electrons, whereas in larger flares, the injected non-thermal energy seems to be sufficient in powering the thermal component. Does this signify the existence of an additional third heating source?

In the limited scope of this thesis address the following pressing questions through multiwavelength observations and contribution in the development of new instruments:

- How does the thermal and non-thermal energy partition change over the duration of flares? What effect do the uncertainties of volume estimation have, on the thermal energy estimates and what conclusions can we draw from that regarding the tension in the thermal and non-thermal energy sources?
- Flares connect various layers of the solar atmosphere via different mechanisms during various stages of its evolution. How does the signature of flares look in the NUV regime which mainly originate in the photosphere, chromosphere and transition region. The transition region is one of the least observed part of the solar atmosphere in context of flares. What is the spectral energy distribution of flares across various wavelength regime and layers, specifically in NUV?

1.6 Outline of Thesis

This thesis primarily focuses on studies of solar flares and their signatures in various layers of the solar atmosphere by using multi-wavelength observation and contribution to the development of the solar Ultraviolet Imaging Telescope (*SUIT*) on board the Aditya-L1 mission. The rest of the thesis is structured as follows:

- Chapter ??: To perform various studies in this thesis, we have used observations from several instruments. Moreover, we have used several techniques to analyse the data and derive physical parameters from these observations. Therefore, we dedicate this chapter to providing relevant details of each instrument we have used. Moreover, we discuss the analysis techniques by providing relevant details and salient features. We emphasise the *SUIT* instrument, mention its primary science goals, and briefly discuss the specific questions that *SUIT* can address regarding solar flares.
- Chapter ??: This chapter addresses the partition between solar flares' thermal and non-thermal energy and their time evolution in two flares. For this purpose, we use multi-wavelength observations from two vantage points recorded by *SDO/AIA*, *STEREO-A/EUVI*, *SO/STIX*, *GOES/SUVI*. Using existing tools and the observations from two vantage points, we propose a new method to accurately calculate the volume of the flaring plasma, which is a crucial parameter in the derivation of

CHAPTER 1. INTRODUCTION

thermal energy. We demonstrate that an accurate estimate of the volume of flaring plasma as a function of time can affect the accurate estimation of thermal energy and, therefore, will have significant implications on the partition between the thermal and non-thermal energy components.

- Chapter ???: Here we discuss some of the initial preparatory analysis we performed for *SUIT* instrument, including the throughput model, selection of science filters, modelling of the spacecraft jitter and its effects on the imaging performance of the instrument. We also describe a scheme for absolute calibration using standard stars like Vega and Sirius. For this purpose, we have used Sun-as-a-star spectra combined with the instrument’s throughput model to evaluate the calibration scheme.
- Chapter ???: Having derived the instrument model for *SUIT*, we now forward the model to the expected observations the instrument will record. For this purpose, we use MPS-Atlas simulation and *IRIS* observations, with measured transmission profiles of various optical components and the PSF.
- Chapter ???: The two filters, among 11, that *SUIT* has are tuned to observe the Mg II h & k lines. Therefore, in preparation for *SUIT*, we study three flares belonging to three different classes, namely X, M and C, observed by *IRIS* in spectroscopy mode. We study the ratio of the two spectral lines *viz.*, Mg II h & k for the three flares. The ratio of the Mg II k& h lines is a proxy for the optical depth of the surrounding plasma. We found that the line intensity ratio shows a correlated increase and decrease with the flare light curve. We argue this to be the signature of plasma flow associated with flare and a change in the density of the local environment.
- Chapter ???: The *SUIT* instrument was switched on Nov 20th, 2023, while still in the cruise phase, with a first light on December 6th. The spacecraft was inserted into the halo orbit around L1 point on Jan 06, 2024. Since the first light, it has detected several flares, both with and without getting into flare mode. In this Chapter, we discuss the first flare observed on Feb 22, 2024, after enabling the flare detection algorithm. We discuss the first results and show the capabilities of the *SUIT* instrument for flare physics.
- Chapter ???: Finally, we summarize the results obtained in the various projects in the context of the overarching perspective of flare energetics and its signature in the chromosphere and photosphere in NUV. We also discuss the caveats and the eventual progression of these projects, as well as the future prospects.

Chapter 2

Existing Solar Observations and Techniques: A bridge towards Solar Ultraviolet Imaging Telescope

The remarkable technological progress attained in the last decades has yielded significant benefits in the form of highly advanced imaging, spectroscopic, and polarimetric instruments designed for astronomical observations. These instruments have empowered us with the ability to scrutinise the Sun with exceptional detail. Specifically, space-based observatories have added new avenues for observing the Sun. The studies within this thesis are performed using multi-wavelength imaging and spectroscopic observations of solar flares recorded from space. This chapter briefly describes and provides relevant details of instruments whose observations are used in this thesis. Moreover, we also discuss the data analysis techniques used for our analysis.

2.1 Solar Dynamics Observatory

The solar Dynamics Observatory (SDO; ?) is a NASA mission designed to understand the causes of solar variability at various spatio-temporal and wavelength scales, as well as its impacts on Earth and the near-Earth environment. It is part of NASAs Living With a Star program and houses multiple instruments onboard to address its numerous scientific goals. Among the three instruments onboard *SDO*, we have extensively used data from two instruments the Atmospheric Imaging Assembly (AIA) and the Helioseismic and Magnetic Imager (HMI).

2.1.0.1 Atmospheric Imaging Assembly (AIA)

AIA (?) obtains full-disk images of the solar transition region and corona with $0.6''$ pixel size and 12s cadence in EUV channels and 24s cadence in UV channel. The field of view (FOV) covers up to $0.5 R_\odot$ above the limb. It incorporates several filters at 94 Å, 131 Å, 171 Å, 193 Å, 211 Å and 335 Å, mainly probing the corona, along with filters at 304 Å, 1600 Å, 1700 Å, and 4500 Å, mainly observing the chromosphere and photosphere, providing a temperature coverage range of 0.06 MK to 20 MK and across various heights. Under different conditions, these AIA filters observe different plasma phenomena (?). Typical exposure times range between 0.5 and 3 seconds. Each AIA telescope is accompanied by its own guide telescope to ensure highly accurate image stabilization. For our analysis, we have extensively used the coronal EUV channel observations from AIA, e.g. 94 Å, 131 Å, 171 Å, 193 Å, 211 Å and 335 Å. These coronal channels observations are usually available with a 12 s cadence.

2.1.0.2 Helioseismic and Magnetic Imager (HMI)

HMI (?) obtains images of the Sun across the Fe I 6173 Å line at six wavelength locations and infers all four components of the Stokes' parameter. Using these observations, various parameters are inferred e.g., Line of Sight (LOS) magnetic field, Doppler velocities, vector magnetic fields etc. We have mainly used the LOS magnetogram for our analysis. These magnetograms have a $0.5''$ pixel size and 45 s cadence.

2.2 Interface Region Imaging Spectrograph (IRIS)

The Interface Region Imaging Spectrograph (IRIS; ?) is a NASA small satellite explorer mission designed to observe the dynamics of the lower solar atmosphere. IRIS contains a spectrograph and a slit-jaw imager (SJI), observing the chromosphere, the transition region, and the lower corona. It primarily observes the Sun in two pass bands around 1400 Å and 2800 Å. IRIS provides data at high spatial resolution ($0.33''$ in FUV and $0.4''$ in NUV), high time cadence (up to 1 second), and high spectral resolution (12 or 25 mÅ).

IRIS observes three wavelength bands: two in the Far Ultraviolet (FUV) range, spanning 1331.7–1358.4 Å and 1389–1407 Å, and one in the Near Ultraviolet (NUV) range, covering 2782.7–2851.1 Å. IRIS measures spectra through two primary modes: raster and sit-and-stare. In raster mode, the slit traverses a field of view, capturing spectra from each pixel along its path. When the displacement between consecutive slit positions is comparable to the slit width, it is called dense raster mode; otherwise, it is called sparse raster mode. Alternatively, the instrument may position the slit on a specific region for observation of the Sun. This mode can allow the Sun to naturally rotate across the region or adjust for solar rotation while maintaining continuous observation. This mode is referred

to as sit-and-stare. In our analysis, we have used both spectra and SJI imaging from the Mg II h & k window and SJI imaging from the Si IV 1402 Å window.

2.3 Spectrometer/Telescope for Imaging X-rays (STIX)

Solar Orbiter (SO; ?) is a joint mission between the European Space Agency (ESA) and NASA, launched in February 2020. The Spectrometer/Telescope for Imaging X-rays (STIX, ??) is designed to study the Sun’s X-ray emissions, providing crucial insights into solar flares and other high-energy phenomena. STIX incorporates a set of collimators and detectors to capture high-resolution images of the Sun in X-rays. These images allow us to pinpoint the locations and intensities of X-ray emissions associated with solar flares. The instrument covers a broad range of X-ray energies, from approximately 4 to 150 keV, probing both thermal and non-thermal X-rays. STIX provides X-ray imaging with a spatial resolution $\sim 7''$ at the shortest wavelengths using Fourier imaging techniques. Notably, the spatial resolution depends on the visibilities at various energies. STIX can operate at a temporal cadence as high as 0.1 s. The cadence of observation is adjustable depending on the flaring activity. The instrument operates in two data modes: the low-resolution background monitoring mode in quiet conditions and the high-resolution mode activated during solar flares. STIX works together with other instruments onboard the solar Orbiter, providing complementary measurements to enhance our understanding of the Sun’s dynamic behaviour across different wavelengths and energy ranges.

2.4 Extreme Ultraviolet Imager (EUVI)

Solar Terrestrial Relations Observatory-Ahead (*STEREO-A*; ?), is one of two spacecraft in NASA’s STEREO mission, which was launched in October 2006 with the goal of studying the Sun and its dynamic behaviour. *STEREO-A* and its twin spacecraft *STEREO-B* (Behind) were designed to provide stereoscopic views of the Sun, enabling three-dimensional observations of solar phenomena such as coronal mass ejections (CMEs) and solar flares. Extreme Ultraviolet Imager (EUVI; ?) is one of the key instruments onboard the *STEREO-A* spacecraft. EUVI is designed to capture images of the Sun in the extreme ultraviolet (EUV) wavelength range. This range of wavelengths is particularly useful for studying the Sun’s outer atmosphere, known as the corona, and observing features such as solar flares, coronal loops, and coronal holes.

EUVI can capture high-resolution images of the Sun’s corona, with spatial resolutions in order of a few arcseconds when the respective spacecraft is at the perihelion. It observes the Sun in 171 Å, 195 Å, 284 Å and 304 Å, simultaneously. EUVI provides continuous observations of the Sun from the *STEREO-A* spacecraft’s vantage point, located slightly ahead of Earth in its orbit around the Sun. This allows EUVI to monitor solar activity

over extended periods and to track the evolution of solar features such as AR, flares, and CMEs. We have used 171 Å and 195 Å observations from EUVI for our analysis.

2.5 X-Ray Telescope (XRT)

Hinode (?), meaning "Sunrise" in Japanese, is a space mission launched by the Japan Aerospace Exploration Agency (JAXA) in collaboration with NASA and the UK Space Agency in September 2006. Also known as solar-B before its launch, *Hinode* is dedicated to studying the Sun's magnetic field and its dynamic behaviour, focusing on understanding the mechanisms driving solar activity and space weather phenomena. The X-Ray Telescope (XRT; ?) is one of the key instruments aboard the *Hinode* spacecraft.

XRT captures solar corona images in X-ray wavelengths, allowing us to study phenomena such as solar flares, coronal loops, etc. Its imaging capabilities enable us to investigate the solar corona's structure, dynamics, and heating mechanisms with a pixel size $1.028''/\text{pix}$ and a Field of View (FoV) size ($34' \times 34'$). XRT utilizes narrow-band filters to isolate specific X-ray emission lines emitted by highly ionized elements in the solar corona sensitive to temperatures from 1 – 30 MK. XRT provides continuous observations of the solar corona from the vantage point of the *Hinode* spacecraft, which orbits the Earth in a Sun-synchronous polar orbit. The cadence of XRT observations can range from 30 – 60 s in the regular synoptic mode and upto 2 s in flare mode. In our analysis, we used XRT imaging observation from various filters.

2.6 Geostationary Operational Environmental Satellites (GOES)

Geostationary Operational Environmental Satellites (GOES) are a series of weather satellites operated by the National Oceanic and Atmospheric Administration (NOAA) in the United States. These satellites continuously monitor weather conditions across the Americas, including the United States, Canada, Mexico, and parts of South America. GOES data are used by meteorologists and weather forecasters to monitor and predict weather conditions, track severe weather events, and issue warnings and advisories to the public. The continuous monitoring provided by GOES satellites helps improve the accuracy and timeliness of weather forecasts. In addition to monitoring terrestrial weather, GOES satellites also monitor space weather conditions, including solar flares, coronal mass ejections (CMEs), and geomagnetic storms. This information is crucial for forecasting space weather events and assessing their potential impact on satellite communications, navigation systems, and power grids. Among the numerous instruments on-board *GOES*, we have used data from two instruments extensively – X-Ray Sensor (XRS) and solar Ultra Violet Imager (SUVI).

2.6.0.1 X-Ray Sensor (XRS)

The X-Ray Sensor (XRS; ?) is an instrument onboard *GOES*. The primary function of the XRS is to continuously monitor and measure full disk integrated solar soft X-ray emissions, particularly those associated with solar flares. XRS is designed to detect and measure solar X-ray emissions in two energy bands: short wavelength (0.5 to 4 Å) and long wavelength (1 to 8 Å) with a 2 s cadence during nominal operations.

2.6.0.2 Solar Ultraviolet Imager (SUVI)

Solar Ultraviolet Imager (SUVI; ?) is an instrument aboard *GOES*, designed to observe the Sun in the EUV spectrum, providing crucial data for monitoring solar activity and space weather. SUVI captures images of the Sun in 94 Å, 131 Å, 171 Å, 195 Å, 284 Å and 304 Å with a 2.5" pixel size. These wavelengths are very similar to AIA and provide complementary observations and very similar temperature coverage as AIA. The FoV of SUVI is rotated by $\sim 45^\circ$, and provides a larger radial distance coverage along the diagonals. In our analysis, we have used SUVI observations from 94 Å, 131 Å, 171 Å, and 195 Å.

2.7 Techniques for Astrophysical Plasma Diagnostic

We employ various techniques throughout this thesis to infer electron density, ion and electron temperature, velocity, and thermal structure of the plasma observed in both Chromosphere and Corona. It is standard practice to use atomic databases like CHIANTI (??) to derive the plasma properties. Below we describe the working principle of the methods used within the scope of this thesis.

2.7.1 Differential Emission Measure and Thermal Properties of the Plasma

Differential emission measure analysis is a commonly employed method with instruments that observe multiple spectral bands to determine the temperature and emission measure of optically thin coronal plasma exhibiting multiple thermal components along a line of sight. However, the inversion process is often challenging due to its ill-posed nature and the frequent lack of sufficient constraints, making it an under-determined problem. One of the very first DEM calculation algorithm was *xrt_dem_iterative*, which was designed and validated for use with XRT data (??).

The intensity observed by any optically thin imager can be related to the temperature distribution in solar Corona with

$$g_i = \int_T R_i(T) \zeta(T) dT + \delta g_i \quad (2.1)$$

In Eqn. ??, g_i is the counts observed in some specific filter (usually in units of $\text{DN} \cdot \text{s}^{-1} \cdot \text{pix}^{-1}$), δg_i is the observed error, R_i is the temperature response function of the specific filter and $\zeta(T)$ describes the thermal distribution of the local plasma (usually in units of $\text{cm}^{-5} \cdot \text{K}^{-1}$). For multiple filter observations, this problem can be posed as a matrix equation in the form of $\vec{g} = \mathbb{R} \vec{\zeta} \Rightarrow \vec{\zeta} = \mathbb{R}^{-1} \vec{g}$. However, because of the ill-posed and under-determined nature of the inverse problem, any attempt to invert this set of equations and recovering the DEM results in a significant increase in the noise.

There are several well-characterised methods for inverting the DEM. In this thesis, we have used the method based on regularized inversion developed by ?, to infer the thermal distribution of the coronal plasma. Given the under-defined nature of the inverse problem, the problem reduces to a least-square minimizing problem

$$\|\tilde{\mathbb{R}}\zeta(T) - \tilde{g}\|^2 + \lambda \|\mathbf{L}(\zeta(T) - \zeta_0(T))\|^2 = \min \quad (2.2)$$

where $\tilde{\mathbb{R}} = (\delta g)^{-1} \mathbb{R}$ and $\tilde{g} = (\delta g)^{-1} g$. The minimization is performed using the Lagrange multiplier method. \mathbf{L} is the constrain matrix, λ is the regularization parameter and $\zeta_0(T)$ is the initial guess solution for the DEM. For further details please refer to ?.

With the inverted DEM we get information regarding the distribution of the plasma at a range of temperatures. We can calculate the Emission Measure (EM) given by, $EM = \int_T DEM(T) dT$ (in units of cm^{-5}). The EM is connected to the local plasma density by $EM = \int n_e^2 dl$. We can also infer the average temperature of the local plasma with the DEM by, $\bar{T} = \frac{1}{EM} \int_T DEM(T) T dT$.

2.7.2 Doppler and Non-thermal Velocity from Spectra

The bulk motion of the plasma along our line of sight can be easily inferred by measuring the red/blue shift of various lines compared to their rest wavelengths. This shift in wavelength is related to the LOS velocity by, $\frac{V_{LOS}}{c} = \frac{\Delta\lambda}{\lambda}$.

In addition to the plasma's bulk velocity, several parameters can be inferred from the spectra. The spectral lines are formed due to the transition of electrons between two atomic/ionic energy levels. Instead of a sharp Dirac-delta function, we get the spectra broadened over a wavelength range due to several factors, e.g., thermal broadening, Doppler broadening, pressure, optical depth, etc. The FWHM of the spectral line is given by, $\text{FWHM} \sim \frac{\lambda_0}{c} \sqrt{\frac{2k_B T}{m} + v_{nth}^2 + r^2}$. Here, λ_0 is the central wavelength, T is the temperature of the plasma, m is the mass of the ion, v_{nth} is the non-thermal velocity and r is the given instrumental width.

The non-thermal broadening of spectral lines is caused by various factors e.g., turbulence, wave motion, nano flares, small-scale local flows, magnetic reconnection, etc. All of these broadening appear on top of the Doppler broadening. Accurate estimation of the

non-thermal broadening depends significantly on the accurate estimation of the instrumental broadening.

2.8 The solar Ultraviolet Imaging Telescope (SUIT)

The solar Ultraviolet Imaging Telescope (SUIT; ??), is one of the seven payloads aboard the Aditya-L1 mission (??) led by the Indian Space Research Organization (ISRO). Launched on September 2, 2023, the satellite orbits around the Sun-Earth L1 point in a halo orbit. Equipped with eleven science filters, comprising eight narrow-band and three broad-band filters, SUIT possesses a distinctive capability to explore various heights within the solar photosphere and chromosphere. This capability aids in understanding the diverse physical processes involved in the transport of mass and energy across different layers of the Sun. Additionally, SUIT offers a unique opportunity to spatially measure the solar spectral irradiance in the Near Ultraviolet (NUV) range, a critical aspect in advancing our comprehension of Sun-climate relationships.

SUIT is designed to deliver continuous full-disk and Region of Interest (RoI) solar images, boasting a plate scale of $0.7''$. It possesses the ability to track RoIs while compensating for the effects of differential rotation, as outlined by ?. Additionally, SUIT is equipped with onboard intelligence to detect and localize flares, and it can autonomously adjust exposure times to prevent saturation. The primary scientific inquiries targeted by SUIT include (?):

- Dynamic coupling between the lower and the middle solar atmosphere
- Measurement of solar spectral radiance in the NUV.
- Spectral energy distribution of solar flares in NUV
- Dynamics of chromospheric eruptive phenomena at various spatiotemporal scales
- Initiation of Coronal Mass Ejections(CMEs) and space weather: the kinematics of erupting prominence during the early phase.

2.8.1 SUIT & solar Flares

Solar flares are the most powerful magnetic events in the solar system. They are described as a sudden increase in brightness in localized areas on Sun. Within tens of minutes, they can release over 10^{32} erg of energy, which is emitted across the entire electromagnetic spectrum from radio to gamma rays. They can also launch high energetic particles into the interplanetary medium. Most of the flares occur in magnetic active regions, and the amount of flare energy released is comparable to the free energy stored in the magnetic system. The term "flare" is generally used explicitly for the entire magnetically-driven

CHAPTER 2. SOLAR OBSERVATORIES AND ANALYSIS TECHNIQUES

event's electromagnetic radiation, as it is the most significant fraction of the total energy liberated. The total energy released varies from event to event. It is also known that larger events occur much less frequently than smaller events.

The solar Ultraviolet Imaging Telescope (SUIT; ??) is one of the seven payloads onboard the Aditya-L1 mission (?) of the Indian Space Research Organization (ISRO). With its eleven science filters (three broadband and eight narrow band), SUIT will have the capability to probe different heights of solar atmosphere in photosphere and chromosphere to help us understand the various processes that transport mass and energy from one layer to another. Through SUIT imaging, we would be able to resolve solar flares spatially on the surface of the Sun, for the first time in near ultra-violet (NUV) **200 – 400 nm regime**, which will help us to address the questions regarding their build-up and triggering mechanism. In addition, to measure the spatially resolved solar spectral irradiance within the wavelength range that is central for studying the Chemistry of oxygen and ozone in the Stratosphere of Earth's atmosphere.

It has been shown that the majority of flare energy emerges at the visible and UV wavelength range (?). ? showed that about 77% of the energy is released in the wavelength range > 200 nm, and only 23% is seen in extreme ultraviolet (EUV) and soft X-ray (SXR), i.e., below 200 nm (???). Although the energy content in hard X-ray (HXR) is a tiny fraction of the total energy budget, they are still crucial in understanding the energization process (?). However, to develop a comprehensive understanding of solar flares, it is mandatory to perform multi-wavelength studies of all kinds of flares. This may have implications on the physics of the origin of solar flares and different physics processes and contribute to the solar spectral irradiance as a function of the solar activity cycle. Although we have been observing Sun and solar flares in various wavelengths, the spectral energy distribution of the radiated energy from the flares is still very poorly understood. The first solar flares were observed from the ground in the visible domain (??). It is also well known that the flare emission in the visible domain occurs mainly in $H\alpha$ and Ca II lines (???). However, the lesser understood component of the visible and Near Ultra Violet (NUV) emission is the enhancement of the continuum. The study of the white-light (WL) flares has proven to be very difficult because they have a very short duration and low contrast against the background, making their observation from Earth rare and of poor quality. Also, the flares in NUV are not observable from any ground-based instrumentation as most of the NUV gets absorbed in the upper atmosphere, thus requires space-based observations. **The attenuation is usually given by**

$$I = I_0 e^{-\alpha d} \quad (2.3)$$

where the I and I_0 are the initial and transmitted intensity respectively, ' d ' is the distance traveled by the incident flux. The attenuation coefficient (α) is defined in units of length^{-1} and given by the Linke-Borne formula (??), $\alpha = A\lambda^{-B}$, which depends on various physical parameters of the atmosphere,

e.g., density, temperature, pressure, composition of the air column etc. Under average atmospheric conditions, the attenuation coefficient varies significantly in the wavelength range 200 – 400 nm, varying from $> 4 \text{ km}^{-1}$ around $\sim 200 \text{ nm}$, to $< 0.4 \text{ km}^{-1}$ around $\sim 400 \text{ nm}$ (see Fig.7, Fig.83 and the accompanying discussions in ?).

The origin of the WLFs, i.e., the physical process responsible for generating the continuum and its contribution to the overall energy distribution, is still highly uncertain. The question remains whether WLFs are photospheric phenomena due to H^- free-free emission or chromospheric phenomena due to H free-bound emission. The more recent studies further constrain the origin of the WLFs to be Chromospheric phenomena, as it has been shown that the WL and HXR foot point centroids are cospacial. Similarly, ? constrained the cospacial WL and HXR foot points within the chromosphere for three flares. With the help of SUIT, we would be able to localize the WL flares and resolve them on various parts of the solar disk, which along with observations from Interface Region Imaging Telescope (IRIS), Helioseismic and Magnetic Imager (HMI), would help us localize the source of the WL foot points and also comment on the formation mechanism of the WL itself.

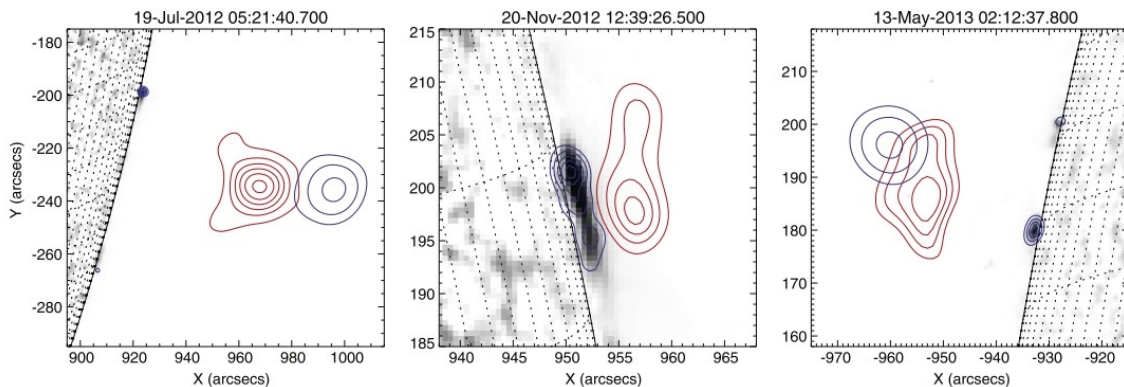


Figure 2.1: X-ray and optical imaging of the three flares at the peak time of the impulsive phase: the images are from HMI with the pre-flare image subtracted. The contours represent RHESSI Clean maps in the thermal (red, 1215 keV) and non-thermal (blue, 3080 keV) HXR range (?).

The spectral energy distribution of flares is one of the critical areas of interest in the physics of flares. A complete understanding of this will help us decode the physical processes involved in solar flares and help quantify their effects on solar spectral irradiance. Ideally, it would be essential to observe flares at all wavelengths simultaneously with sufficient spatio temporal resolution to figure out the spectral energy distribution of flares. Unfortunately, this is generally not the case, and we have to rely on the sporadic observations made using ground-based instruments in the visible domain. As mentioned earlier, the majority of the flare energy is emitted in the NUV and visible domain. ??, performed statistical studies using a large number of flare observations across a wide energy range. They demonstrated,

CHAPTER 2. SOLAR OBSERVATORIES AND ANALYSIS TECHNIQUES

at the peak of the flare, about 70% of the total energy was radiated in the continuum visible and NUV channel as illustrated in ???. SUIT would observe and resolve the solar flares within 200-400 nm using 8 NBs and 3 BBs. This, along with IRIS data, would help us comment on the energy distribution of flares of various classes.

Mean X-ray class	TSI(ergs)	Ratio $\frac{26-34nm}{TSI}$	Ratio $\frac{0-50nm}{TSI}$	Ratio $\frac{0.1-0.8nm}{TSI}$	Ratio $\frac{\text{continuum}}{TSI}$
X3.2	5.9×10^{31}	0.9-0.8%	12-9%	1.2-1%	67%
M9.1	1.6×10^{31}	1.7-0.4%	23-5%	1-0.4%	85%
M4.2	1.3×10^{31}	2.2-0.5%	18-6%	0.6-0.3%	74%
M2.0	5.1×10^{30}	1.7-0.6%	18-6%	0.7-0.4%	69%
C8.7	3.6×10^{30}	1.5-0.5%	16-5%	0.4-0.2%	72%

Table 2.1:: Spectral Energy Distribution from a sample of 2100 flares across various wavelengths(?).

Finally, one of the major question of interest is how the solar flares affect the Spectral solar Irradiance (SSI) and Total solar Irradiance (TSI) variability from a short to much longer, solar Cycle timescale. ?? performed statistical studies using a large number of flare observations across a wide energy range. For this purpose, they used the full Sun observations of solar flux from solar and Heliospheric Observatory (SoHO), three visible solar irradiances from VIRGO/Solar Photometer (SPM) pass bands centred on 402 nm, 500 nm, and 862 nm, respectively, from 1996 to 2008. Additionally, they also use the EUV irradiance in the ranges 0.1-50 nm and 26-34 nm measured by SOHO/Solar EUV Monitor (?) and SXR measurements from GOES satellites. They showed that stacked TSI variation profiles during solar flares show variation at more than 2 sigma level during the peak flare time, indicating the presence of flare signals in the TSI measurements.

This allows us to quantify the solar variability induced be solar flares of various timescales. With the help of SUIT, we would be able to localize the flare locations and study the change in SSI from the local environment in the 11 science filters. This information combined with TSI measurements can allow us to quantify the effect of flares of various energy scales on the TSI variability of the Sun. As, both the TSI and SSI variability directly or indirectly couples with various atmospheric parameters, we can also study the effect the flares have on them. For example, the Earth's atmospheric chemistry and composition respond to any changes in solar UV output in a very nonlinear fashion (?). Since the number of flares also shows a change with solar activity, it is prudent to ask how much do flares contribute to the solar spectral irradiance in NUV **over solar cycle timescales**. This is particularly important because the irradiance in NUV plays a key role in heating the upper and middle layers of the Earth's atmosphere directly and their coupling with the Stratosphere. It also directly influences the middle and lower atmosphere chemistry and composition via the Ozone-Oxygen cycle. **In certain extreme cases, a single flare can drive noticeable changes in the upper atmospheric conditions, e.g., the X-class flare on 7th September, 2011 induced a large variation in the E-layer conductiv-**

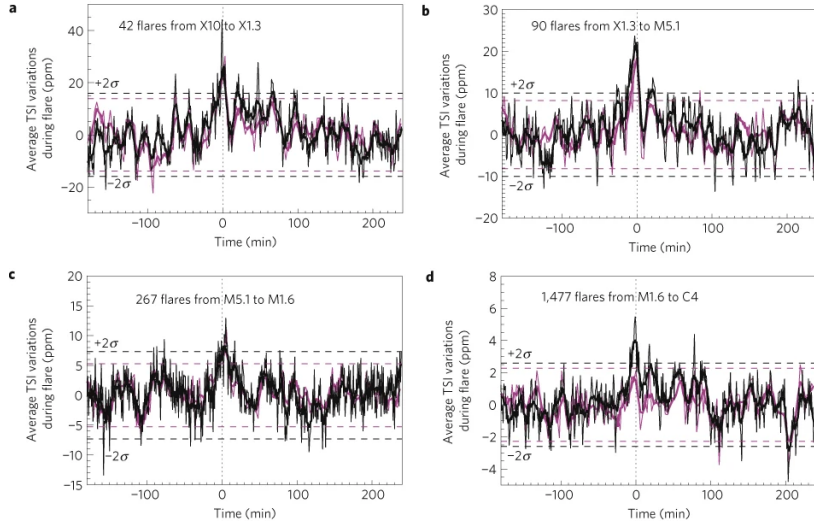


Figure 2.2: Averaged TSI variations during flares. The TSI time-series averages over four exclusive sets of solar flares of decreasing amplitude. The black and pink curves correspond respectively to the TSI measured by the PMOV6 and the DIARAD radiometers. The dashed lines correspond to the 95% confidence levels, while the vertical line denotes the peak time of the flare (?).

ity driven by the Ly – α radiation (see Fig.10 and the accompanying discussion in ?).

CHAPTER 2. SOLAR OBSERVATORIES AND ANALYSIS TECHNIQUES

Chapter 3

Estimating thermal energy of two Solar Flares

3.1 Introduction

Solar flares are the largest magnetic events in our solar system. They are characterized by the eruptive release of magnetic energy, and manifest as localized transient heating of coronal plasma to temperatures over ~ 10 MK. Flares are characterized by the full-disk integrated peak soft X-ray flux observed by the X-Ray Sensor onboard the *Geostationary Operational Environmental Satellites (GOES/XRS, ?)* (“*GOES class*”). The various components of the flare manifest in different wavelengths of the electromagnetic spectrum. The flare arcade and the fan exhibit the thermal plasma, while the majority of the non-thermal energy is from the foot points (?). The hot coronal plasma exhibited by flares is generally attributed to chromospheric evaporation, heated by the collisions of the flare-accelerated electrons in the impulsive phase (?). There is also strong evidence that the plasma might be directly heated in the corona in some cases (e.g. ??).

There have been several works (???????) that study the partition between the thermal and non-thermal energies in flares, which holds key insight into the relevant underlying physical processes in the flares. The results have been contradictory, and there is no consensus on whether non-thermal energetic electrons have enough energy to power the observed thermal energy component of smaller flares. These studies usually use peak thermal energy as a representative of the bulk thermal output of the flares. While these quantities are fair representation of the bulk thermal output of the flare, identifying subtle differences in the heating mechanisms at play at different stages of the flares requires a quantification of the thermal energy as a function of time.

There are several studies (??) that estimate thermal energy as a function of time. The

thermal energy of the flares is defined as

$$U_{Th} \simeq 3n_e k_B T V f, \quad (3.1)$$

where ‘ n_e ’ is the electron number density of the flaring plasma, ‘ V ’ is the volume of the flaring plasma, ‘ f ’ is the volume filling factor, and ‘ T ’ is the instantaneous temperature. One of the key challenges in characterizing the flares’ thermal energy is determining the volume.

? used $\frac{1}{e^2}$ contour of soft X-ray emitting region to identify the flare area ‘ A ’, which was subsequently used to estimate the volume, $V \sim A^{\frac{3}{2}}$. ? used a similar method, using intensity threshold on AIA 131 Å observation, to estimate the flare area (A). ? used a similar method with *Reuven Ramaty High Energy Solar Spectroscopic Imager (RHESSI, ?)* soft X-ray images to estimate the lower limit of the volume. They used *RHESSI* hard X-ray imaging to estimate the distance between two footpoints. Assuming a perfect “arc-shaped” loop they calculated the upper estimate of the volume and concluded that the largest source of uncertainty in determining the thermal energy arises from the uncertainty in the filling factors.

? also estimated the evolution of cumulative non-thermal energy injected by the electrons by assuming a thick-target model (?) and fitting the *RHESSI* spectrum of the events. They fitted the *RHESSI* spectra in 25–35 keV bands to determine the non-thermal energies in time bins with significant emission above 25 keV. This process ensures a better accuracy for determining non-thermal energy by dividing the flare into short time intervals with large energy inputs, resulting in small thermal energy losses. They found that the non-thermal cumulative energy was larger than the thermal component of the flare for most of the duration of the flare. This is expected as radiative cooling significantly lowers the temperature of the flare arcade as the flare evolves. They also deduced that during the early impulsive phase, the cumulative non-thermal energy could be lower than the thermal energy, depending on the estimates used for the flaring plasma volume.

The filling factor ‘ f ’ quantifies the fraction of the apparent volume that is filled with the plasma of a specific temperature. It might also hold information about the geometric projection effects of the real volume into the apparent projected volume that is observed. Due to the highly multi-thermal nature of the flaring plasma and rapidly changing volume during the rise phase of the flare, it is challenging to define a filling factor that describes the plasma volume across the evolution of the flare.

? studied super hot flares from *RHESSI* observations, and used a 50% intensity contour of cleaned *RHESSI* images to estimate the flare area, A . The volume $V = \frac{4}{3}\pi(A/\pi)^{3/2}$ was inferred from the area assuming spherical symmetry. The two temperature components from the *RHESSI* spectral fit were assigned a volume $V/2$ each to estimate the total thermal energy. In all of these cases, the assumption of symmetrical expansion is useful because the thermal energy was estimated from a spectra obtained by integrating multiple pixels. There is no reliable way to address the spatially varying multi-thermal nature of the flaring plasma

in these cases.

In addition to the bulk thermal plasma in the flare loop, there are studies that suggested completely different heating mechanisms at play in specific flares. For example, ? suggested a super hot plasma component in flares is directly heated in the corona in some large solar flares. Sustained temperatures in supra-arcade fans in flares have been hypothesized to be caused by supra-arcade down flows (e.g. ?), suppression of conduction by turbulence (e.g. ?) or global compression from reconnection inflows (e.g. ?). These processes are distinctly different from chromospheric evaporation, which is characterized by the development of the hard X-ray foot-points and increasing intensity of soft X-ray and EUV-emitting plasma as the loops fill up.

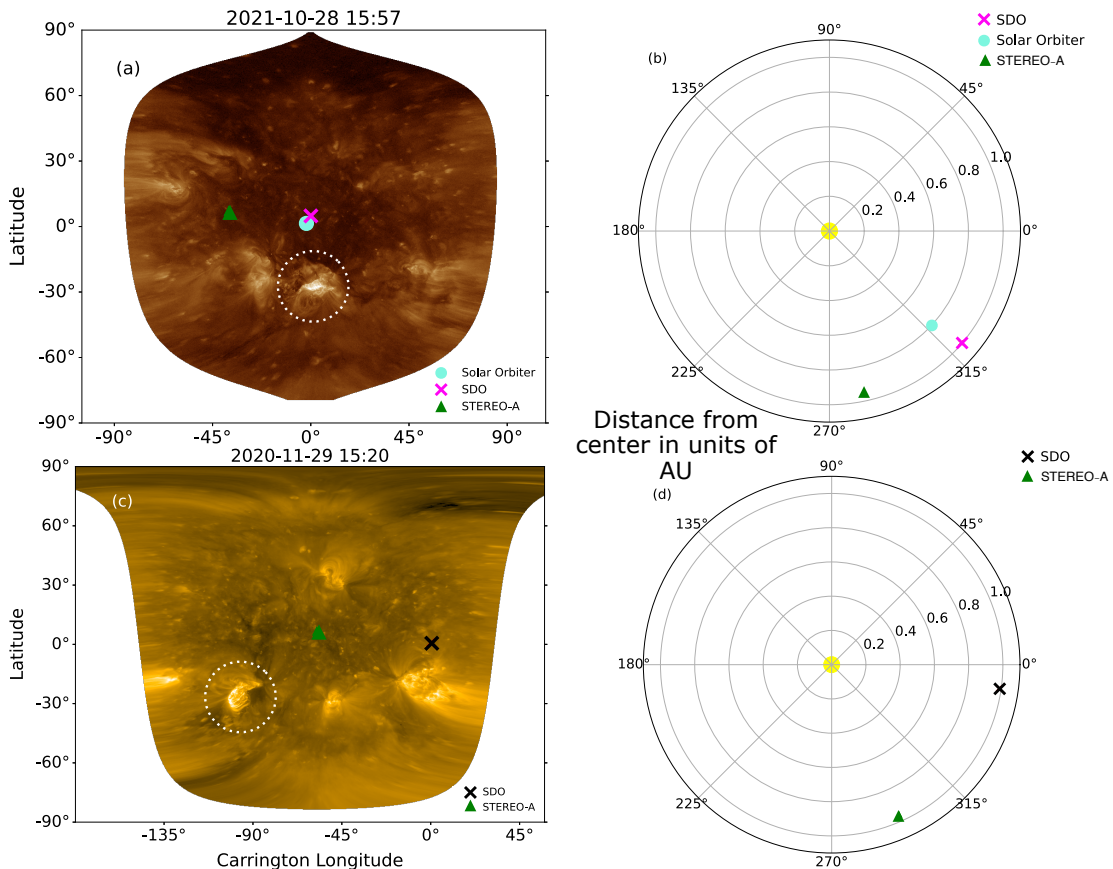


Figure 3.1: Position of various instruments during the flares. AIA 193 Å observations during 2021 Oct 28 (panel a) and EUVI 171 Å observation during 2020 Nov 29 (panel c) in Heliographic Stonyhurst (HGS) coordinates. The two flares studied here are enclosed by white dotted circle. The projected positions of *Solar Orbiter*, *SDO* and *STEREO-A* are marked as labelled. Positions of various spacecrafts projected onto the Heliocentric Inertial (HCI) frame for the for 2021 Oct 28 (panel b) and 2020 Nov 29 (panel d), as labelled.

Here we study the evolution of the thermal energy of two flares, *viz.* M-class and X-

class. We use existing tools and observations of the same region on the Sun from different vantages to estimate the volume of the flaring plasma more accurately. We show that a better estimate of the plasma volume affects the estimate of the thermal energy and has implications towards the energy budget of the flare. We also estimate the cumulative non-thermal energy deposited by the non-thermal electrons and compare it with our thermal energy estimates for the flare observed on 28 October, 2021. In §?? we discuss the observations used in this **chapter** and details of our analysis. We discuss our method for estimating the thermal energy in §??. In §?? and §??, we describe our method of volume estimation and cumulative non-thermal energy estimation, respectively. We discuss the results in §??.

3.2 Observations and Data Analysis

We study the two flares observed on 28 October, 2021 (X-class) and 29 November, 2020 (M-class) observed on the disk center and limb of the Sun, respectively, from the perspective of Atmospheric Imaging Assembly onboard the *Solar Dynamic Observatory* (*SDO*/AIA, ??) vantage point. For this study, we primarily use the observations from AIA, the Extreme Ultraviolet Imager onboard *Solar Terrestrial Relations Observatory-A* (*STEREO-A/EUVI*, ??) and the Solar Ultraviolet Imager onboard *GOES* (*GOES/SUVI*, ?), along with imaging from the Spectrometer/Telescope for Imaging X-rays onboard *Solar Orbiter* (*SO/STIX*, ???), the X-Ray Telescope onboard *Hinode* (*Hinode/XRT*, ?) and the X-Ray Sensor onboard *GOES* (*GOES/XRS*, ?). For the relevant specification of the instruments used, refer to Table ??.

The positions of various spacecraft with respect to the flares' location on the solar disk is illustrated in Fig. ???. The AIA 193 Å observation of the 2021 Oct 28 flare is projected to Heliographic Stonyhurst (HGS) coordinates in panel a, with *SDO* (magenta cross), *SO* (cyan circle) and *STEREO-A* (green triangle) positions marked with respect to the flare location in Fig. ???.a. The flare is marked with white dotted circle. The relative separation between the spacecrafsts show the difference in the polar angle (vertical axis in Fig. ???.a) and azimuthal angle (horizontal axis in Fig. ???.a) introduced due to difference in vantages. The positions of the spacecrafsts projected onto the Heliocentric Intertial (HCI) frame for the 2021 Oct 28 event is plotted in Fig. ???.b. The relative separation between the spacecrafsts show the difference in azimuthal angle and the distance from the sun (distance from the center radially outwards in Fig. ???.b). We show the same for the 2021 Nov 29 flare in Fig. ???.c and d, with *STEREO-A/EUVI* 171 Å emission projected to HGS and HCI coordinates.

3.2.1 X flare on 28th October, 2021

The X1 flare occurred on Oct 28, 2021 (SOL2021-10-28T15:35) near $\sim [0'', -500'']$ solar coordinates as seen from AIA. The flare was observed by *SDO/AIA*, *STEREO-A/EUVI*,

Instruments	Details	Flares
<i>SDO/AIA</i>	0.6 "/pix. Used for estimating the thermal properties. Temperature coverage $5 < \log (T) < 7.5$	28 October, 2021 & 29 November, 2020
<i>GOES/SUVI</i>	2.5 "/pix. Has similar temp. response as AIA. Used for replacing saturated AIA frames in DEM estimation	28 October 2021 & 29 November, 2020
<i>Hinode/XRT</i>	1 "/pix. Used simultaneously with AIA data in estimation of the thermal properties. Temperature coverage $6.1 < \log (T) < 7.5$, provides better constraints on the higher temp. end.	29 November, 2020
<i>STEREO-A/EUVI</i>	1.6 "/pix. Used for estimating the geometry of the arcade. 171 and 195 Å Observations are used with AIA 171 and 193 Å.	28 October 2021 & 29 November, 2020
<i>SO/STIX</i>	X-ray imaging and spectroscopy in the 4-150 keV range. Soft X-ray imaging used for calculating the area of the flare. Spectra used for constraining the thermal and non-thermal properties	28 October 2021
<i>GOES/XRS</i>	Continuous full disk integrated soft X-ray light curve. Used for estimating the bulk thermal properties of the flare.	28 October, 2021 & 29 November, 2020

Table 3.1:: List of the various instruments with their relevant specifications that were used for the analysis of the specific flares.

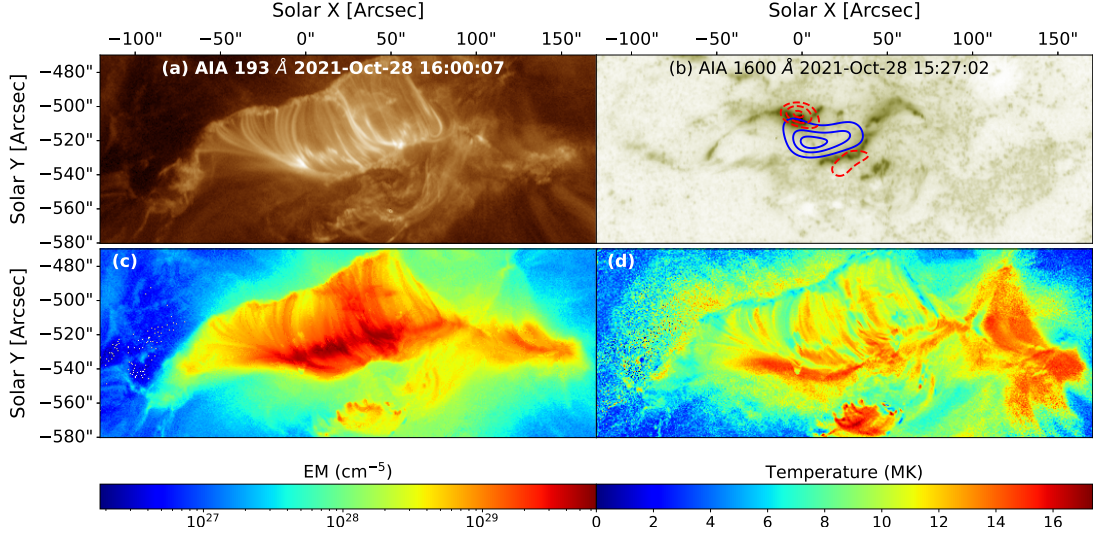


Figure 3.2: X-class flare observed on October 28, 2021. Panel (a): the post eruption arcade as observed in AIA 193 Å. Panel (b): Two ribbon of the flare observed in AIA 1600 Å, overplotted with STIX soft X-ray contours of 4–15 keV (solid blue lines) and hard X-ray contours of 15–25 keV (dashed red lines). Panel (c): the emission measure map of the region integrated over the temperature range of $5 < \log T < 7.4$. Panel (d): the obtained DEM weighted temperature.

GOES/SUVI, and XRT, along with *GOES/XRS* and STIX observations. AIA observations provide imaging with 94, 131, 193, 171, 211 and 335 Å passbands. SUVI provides imaging with similar wavelengths as AIA: 94, 131, 195, 171, 195 and 284 Å, while *STEREO-A/EUVI* provides imaging in 171, 195, 284 Å coronal passbands. The flare exhibits a standard two-ribbon structure, along with a ridge at the top of the rising flare arcade (?). The ridge most prominently shows up in the AIA 193 Å channel with contributions from Fe XII and Fe XXIV.

SO/STIX provides X-ray imaging and spectroscopy in the 4–150 keV range. Spectroscopic observations are provided with 32 pre-defined energy channels distributed in this energy range. STIX is an indirect imager measuring visibilities in the Fourier space, and images can be reconstructed from these visibilities with different algorithms. We use the MEM-GE algorithm (?) to construct the STIX intensity maps.

In Figure. ?? (top row) we display the flare as observed with AIA 193 Å (panel a) and 1600 Å (panel b, inverted colors). These images reveal the two ribbon nature of the flare with post eruption arcades (see e.g. ?). We also overplot the STIX intensity contours (15:27:40 – 15:28:00 UT) in 4–15 keV (blue solid lines) and 15–25 keV (red dashed lines), on an AIA 1600 Å image during the rise phase of the flare (see Fig. ??b). The STIX hard X-ray contour aligns with AIA 1600 Å ribbons.

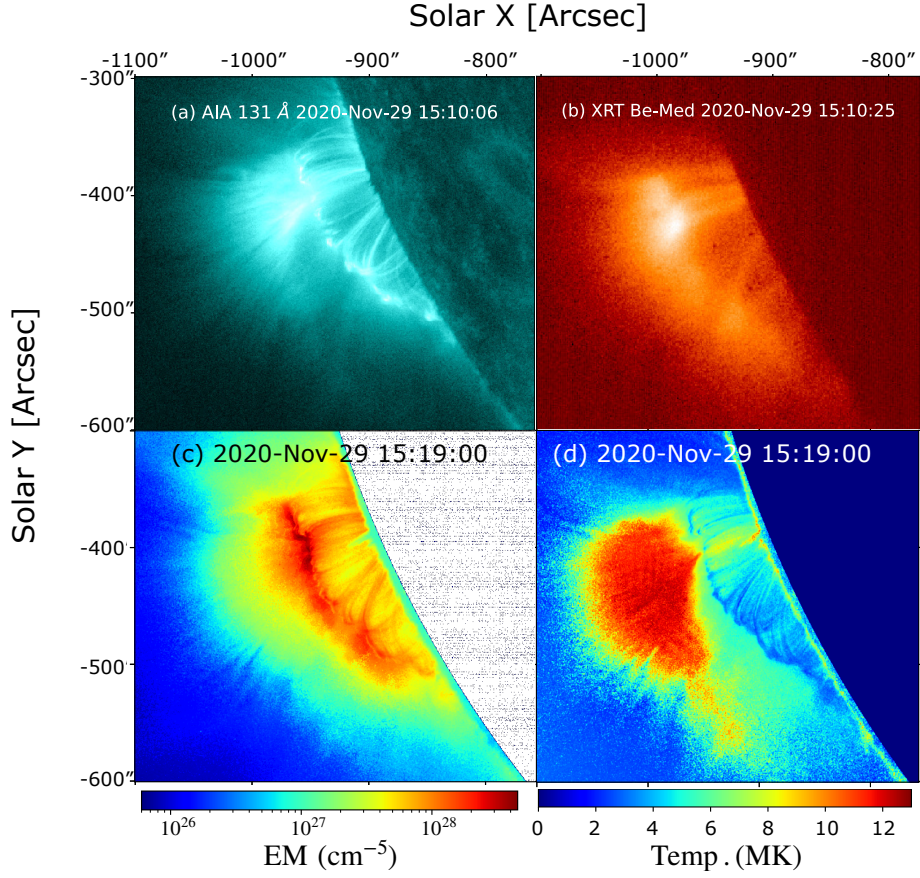


Figure 3.3: M-class flare on Nov 29, 2020 as observed nearly simultaneously by AIA 131 Å (panel a) and XRT Be-med filer (panel b) and the derived EM map (panel c) and DEM weighted temperature (panel d). The EM map is obtained by integrating over the temperature range of $5 < \log T < 7.4$.

3.2.2 M flare on 29th November, 2020

The M flare occurred on November 29, 2020, near $\sim [-950'', -430'']$ solar coordinates from the AIA perspective. In the AIA images, the footpoints were occulted behind the limb. The flare was also recorded by *STEREO-A/EUVI*, *GOES/SUVI* and *Hinode/XRT*. Along with these instruments, there were observations from *GOES/XRS* and *Fermi/GBM*. There were no observations from STIX for this event.

The flare exhibits a fan which is visible in the hot channels of AIA (131 and 193 Å) and the XRT channels. Fig. ??a shows an AIA 131 Å image of the flare recorded during the decay phase. In Fig. ??b, we plot an XRT Be-med filter observation taken near simultaneous with the AIA image. For the M-class event, the *Fermi* observations were periodically eclipsed during the duration of the flare. We do not calculate the cumulative non-thermal energy for this event, as during the eclipses there is no reliable way to estimate

the instantaneous non-thermal energy deposited. Hence, the estimation of cumulative non-thermal energy would not be a fair representation of the total non-thermal energy available.

3.2.3 Thermal Energy

We estimate the thermal energy of the X-class event by calculating the differential emission measure (DEM) of the flaring region from the six AIA passbands including 94 Å (Fe X \sim 1.1 MK, Fe XVIII \sim 7.1 MK), 131 Å (Fe VIII \sim 0.4 MK, Fe XXI \sim 11 MK), 171 Å (Fe IX \sim 0.6 MK), 193 Å (Fe XII \sim 1.6 MK, Fe XXIV \sim 17 MK), 211 Å (Fe XIV \sim 2 MK), 335 Å (Fe XVI \sim 2.5 MK) (??). Near the peak of the flare, several AIA frames are saturated in several instances and as such they cannot be used for the analysis. The SUIVI temperature response is very similar to AIA (?). Therefore, whenever necessary, the specific AIA frames can be replaced by those taken by SUIVI for thermal energy estimates after co-aligning and co-registering the two observations. Moreover, we also need to rescale the AIA temperature response functions to account for the binning of the AIA data to match the SUIVI resolution. Note that since most of the XRT observations during the flare are saturated, we do not include them in our analysis of this flare.

For the M-class event, we estimate the thermal energy using AIA and XRT observations. Here, we bin the AIA observations to XRT pixel size, co-align, and calculate the DEMs. As described earlier, we rescale the AIA temperature response functions to account for the binning of the AIA data.

We use the regularized inversion method (?) to calculate the DEMs. The observed flux from the individual passbands can be written as,

$$F_i = \int DEM_c(T) R_i(T) dT + \delta F_i \quad (3.2)$$

where R_i is the temperature response of the passband ‘i’, δF_i is the error on the observed intensity for the passband ‘i’ and $DEM_c(T)$ is the column differential emission measure (in units of $cm^{-5}K^{-1}$). The DEM inversion was performed for a temperature range $4.5 \leq \log(T) \leq 8$.

With the inverted DEM, we calculate the column emission measure (EM^c in units of cm^{-5}) and DEM-weighted temperature as:

$$EM^c = \int_T DEM_c(T) dT \quad (3.3)$$

$$\bar{T} = \frac{1}{EM^c} \int_T DEM_c(T) T dT \quad (3.4)$$

The temperature range of the integration is set to $5 < \log T < 7.4$. We calculate and plot the emission measure (panel c in Figs. ?? & ??) and the DEM weighted temperature (panel d in Figs. ?? & ??) for all the pixels in the field of view (FOV) for both the flares.

The main goal of calculating the DEM maps is to estimate the thermal energy (using Eqn. ??) arising from various parts of the flare arcade. As alluded to earlier, one of the most crucial quantity is to obtain the volume of the flaring plasma. For our analysis, the volume of the plasma along an individual pixel is given by $V_j = A \times LOS_j$, where LOS_j is the line of sight (LOS) for the j-th pixel in the FOV and A is the physical area of a pixel.

We use the above expression for volume along with the emission measure and DEM weighted temperature estimated from the inverted DEM in Eqn. ?? and sum over the pixels in the FOV to estimate the thermal energy arising from the FOV. This procedure gives us,

$$U_{Th} = \sum_j \frac{3k_B A \sqrt{LOS_j}}{\sqrt{EM_j^c}} \int_T DEM_c(T)_j T \, dT \quad (3.5)$$

where EM_j^c and $DEM_c(T)_j$ are the column emission measure and the column DEM in $5.0 < \log T < 7.4$ for the j-th pixel in the FOV. We have used $n_e^2 \times LOS = EM^c$ and a filling factor $f = 1$. For the 2020 Nov 29 flare we mask the solar disk while calculating the DEMs and thermal energy. As evident from Eqn. ??, one of the major uncertainties in determining the emitting volume depends on determining the LOS for individual pixels in the FOV.

3.2.3.1 Determining the LOS

We use co-temporal *STEREO-A* 171 Å, 195 Å, and AIA 171 Å, 193 Å images with *scc_measure.pro*, available in the *sswidl*, to calculate the height of the loop. This routine allows us to select a point on the observation from one of the two vantages. The line of sight (LOS) through the same point is shown on the observation from the different vantage. The same point can be identified on the projected LOS by the user by identifying similar emission characteristics. The program determines the 3D coordinates of the point (heliographic latitude, longitude and radial distance). We carry out the same measurement at various positions along the loop top, to calculate the change in loop height across the arcade. With the different height measurements at various locations, we can calculate the volume of the flaring plasma under a semicircular assumption. We note that the height estimation using *scc_measure.pro* is limited by our identification of "similar emission characteristics" between the two observations from AIA and *STEREO-A*. We choose multiple points on the top of the arcade, and calculate the height of the arcade at various locations tracing the looptop. The number of points we consider is not fixed and varies from frame to frame. After this, using the chosen points we interpolate to get the loop top from the AIA perspective, and the calculated height at these points gives us how the height of the loop top changes across the arcade. We assume a semi-circular loop geometry with the height of the loop top to calculate the LOS along every pixel within the flare arcade. It is worth reiterating that a majority of the uncertainty in determining the LoS would be arising from the identification of the loop top in two different vantages.

To infer the LoS along individual pixels in the FOV for both the flares, we use AIA and STEREO-A/EUI observations, recorded from two different vantage points, to calculate

the height of **both flare loops**. We show the STEREO-A/EUI 195 Å and AIA 193 Å observation for the Nov 29, 2020 flare in Fig. ?? panel b and a respectively. The blue cross marked in Fig. ??a is the LOS going into the page from AIA perspective. The blue line marked in Fig. ??b is the same LOS projected onto the STEREO-A perspective. The red crosses marked on the AIA 193 Å loops mark the LoS going into the page, to infer the looptop from the AIA perspective. The red crosses marked on Fig. ??b EUVI 195 Å observations marks the position of the looptop along the LoS from AIA perspective considered to find the looptop from EUVI perspective. In Fig. ??c we show the inferred LoS map for these two frames. The fan is assumed to have a constant LoS depth as mentioned earlier. For the loops we calculate the LoS assuming a semi-circular loop geometry with the height inferred from `scc_measure.pro`. The inferred LoS is lower near the loop top, and increases as we move closer to the foot points, exhibiting the variable LoS across the observation frame.

We display STEREO-A/EUVI and AIA-171 images taken **nearly simultaneously** in Fig. ?? a & b, respectively for the 28 Oct, 2021 event. The red and black cross on Fig. ??a shows a point at the top of the flare arcade. The LOS goes into the page through that point from the *STEREO-A* vantage. The blue line in Fig. ??b shows the LOS through the point in Fig. ??a projected to *SDO/AIA* point of view. This demonstrates the geometric effect of observing from different vantage points. In Fig. ??c we show the inferred LoS map from the AIA perspective.

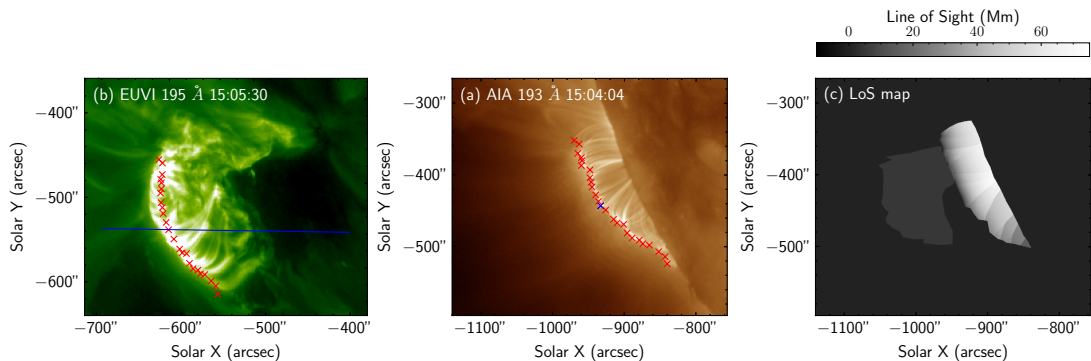


Figure 3.4: (a) SDO/AIA 193 Å observation of the Nov 29 flare in the decay phase. The red and blue crosses marks various points on the top of the arcade used to trace the looptop. The LOS goes into the page from AIA perspective. (b) *STEREO-A*/EUVI 195 Å observation around same time. The blue solid line is the LOS from AIA perspective in panel (a) projected onto *STEREO-A* perspective. The red crosses mark the other red crosses from AIA perspective marked on the looptop visible from Stereo-A perspective. The line of sight of the region is shown in panel (c). The LoS is higher near the base of the loops and lower near the looptop. The fan is assumed to be constant LoS.

The extent of the flare arcade is calculated by selecting pixels from the FOV which are located within an emission measure contour of 5% of the peak emission measure value. It is possible to calculate the extent of the flare arcade from the intensity observed from any

of the *SDO/AIA* or STIX imaging (for further details about the STIX imaging procedure, please refer to ?). However, due to the highly multi-thermal nature of the plasma, this procedure might be prone to missing significant portions of the flare arcade. The emission measure inferred from the DEM, on the other hand, reflects the density of the plasma in the entirety of the concerned temperature range of $5 < \log(T) < 7.4$. Therefore we find that, a 5% contour of peak emission measure gives a better estimate of the extent of flare arcade. Outside of the flare arcade, we assume a LOS ~ 2 Mm (the average thickness of chromosphere).

3.2.4 Energy in the non-thermal electrons

We estimate the energy in the non-thermal electrons for the 2021 Oct 28 X-class event by fitting the STIX spectra. In Fig. ?? .a, we plot the STIX light curve of the event in 4 to 10 keV (solid blue line), 10 to 15 keV (solid orange line), 15 to 25 keV (solid green line) and 25 to 50 keV (solid red line). The attenuator kicked in around $\sim 15:28$ UT, which drastically cuts down the intensity to avoid saturation. The hard X-ray peak is visible in the 25 to 50 keV (solid blue line) at $\sim 15:28$ UT. The soft X-ray peak is visible within the attenuated flux in 6 to 12 keV (solid magenta line) at $\sim 15:30$ UT.

We closely follow the method described in ? to estimate the energy deposited by the non-thermal electrons. We fit the STIX spectra of the event averaged over several time bins during the evolution of the flare with ‘*vth*’ and ‘*thick2*’ functions available in the ‘*OSPEX*’ X-ray spectra fitting package in *sswidl*. We show a reference fit to the spectra obtained over a time bin $\sim 15:27:00$ - $15:27:10$ UT in Fig. ?? panel (b) with ‘*vth*’ (solid green) and ‘*thick2*’ (solid yellow). The function ‘*vth*’ is a two-component thermal function. The parameters are the emission measure and temperature of the two thermal components and the relative abundances of Iron/Nickel, Calcium, Sulfur and Silicon with respect to the coronal abundances of CHIANTI (??). The ‘*thick2*’ assumes the non-thermal component to be bremsstrahlung from energetic electrons with an injected spectrum $F_0(E_0)$ ($e^{-} s^{-1} cm^{-2} keV^{-1}$) in the form of a broken power law:

$$F_0(E_0) = A \begin{cases} 0, & E_0 < E_{min} \\ E_0^{-\delta_1}, & E_{min} \leq E_0 < E_b \\ E_0^{-\delta_2} E_b^{\delta_2 - \delta_1}, & E_b \leq E_0 < E_{max} \\ 0, & E_{max} \leq E_0 \end{cases} \quad (3.6)$$

The parameters of this model spectrum, e.g., the normalization parameter A, the low- and high-energy cutoffs E_{min} and E_{max} , break energy E_b , the power law indices δ_1 and δ_2 below and above the break are constrained by the fitting. We only fix the high energy cutoff at 3.2×10^4 keV for every fit. The high energy cutoff is fixed much higher than our concerned energy range ($\sim O(10^1$ keV)), and we can safely assume that it has a negligible

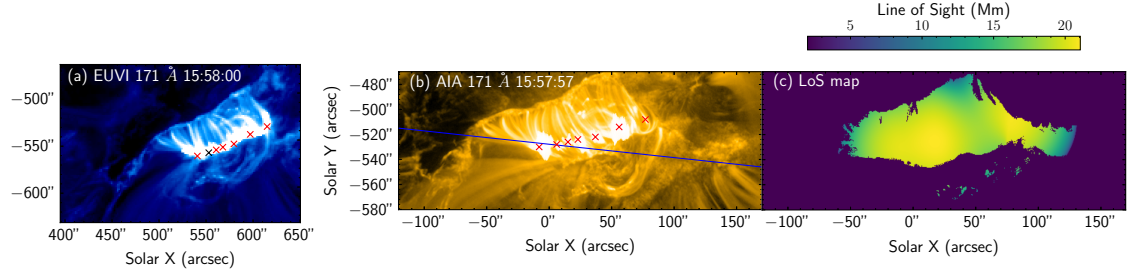


Figure 3.5: (a) *STEREO-A/EUVI* 171 Å observation of the **Oct 28** flare arcade in the decay phase. The red and black cross marks a point on the top of the arcade. The line of sight (LOS) goes into the page through that point. (b) *SDO/AIA* 171 Å observation of the flare arcade. The blue line marks the LOS through the arcade from the *STEREO-A* perspective projected to the AIA perspective. The red crosses mark the other red crosses from *Stereo-A* perspective marked on the loop top visible from AIA perspective. The line of sight of the region is shown in panel (c).

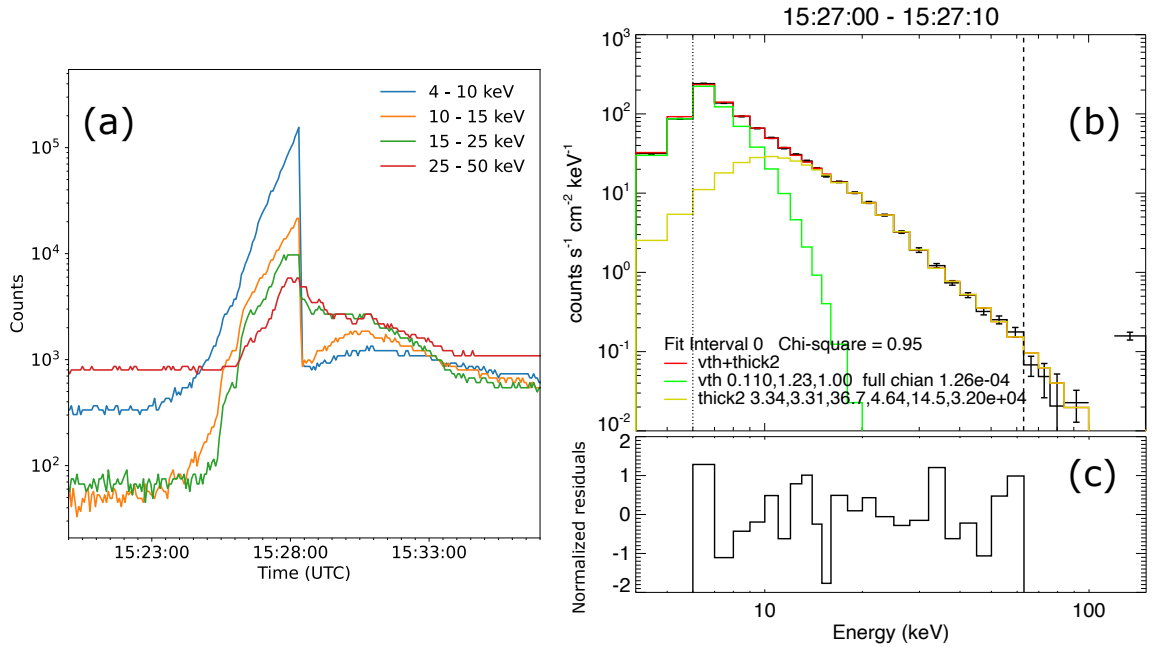


Figure 3.6: Panel a: STIX light curve of the 2021 Oct 28 X-class event in different energy bands as labeled. Panel b: STIX spectra integrated between 15:27:00–15:27:10 UT during impulsive phase, fitted with ‘*thick2*’ (solid yellow), ‘*vth*’ (solid green) and the complete fit function ‘*vth+thick2*’ (solid red line). The panel (c) shows the normalized residuals of the fit.

effect on fitting the X-ray spectra (?). While this serves our purpose of quantifying the bulk non-thermal energy as a function of time, there can be finer details of the physical parameters from the "cold thick target" model that can pose non-physical conditions during the early rise phase of the flares. This can also have noticeable effect on the total thermal energy budget of the flare. To mitigate this several modifications of the cold thick target model have been proposed, e.g., local re-acceleration of electrons and ions (?), warm thick target model (??) and injection of kappa distributed electrons instead of power law (???). We describe the physical origin of some of these models and their effects on the inferred injected electron spectra in Appendix ???. We also fit two of the modified models to the same spectra and compare the differences that arise due to that.

The ‘OSPEX’ fitting is done by a forward fitting procedure. The parameters of the functions ‘*vth*’ and ‘*thick2*’ are varied to generate a photon spectrum, which is folded through the detector response matrix to produce a count rate spectrum. This count rate spectrum is used to constrain the parameters of the functions through an iterative procedure by minimizing the χ^2 between the calculated and measured count rate spectrum. We provide the fitted temperature and the EM of the hotter thermal component in Tab. ?? during various phases of the flare. The temperatures listed in Tab. ?? is lower than the upper limit of the temperature range used ($5.0 \geq \log T \leq 7.4$) to calculate the EM and DEM weighted temperature in §??.

The non-thermal energy in the electrons (U_e) at any instant $t = t'$ can be estimated by integrating the best-fit electron energy spectrum via:

$$U_e(t = t') = \Delta t \int_{E_{min}}^{E_{max}} F_0(E_0)(t = t') dE_0$$

where the electron energy distribution is constrained by fitting the count spectra for the time interval $t' - \Delta t/2 \leq t \leq t' + \Delta t/2$. The cumulative energy deposited into the foot point over time by the non-thermal electrons is a good indicator for the source of the thermal energy of the plasma. We add the energy deposited at the foot points by the non-thermal electrons from every time bin, to estimate the cumulative energy deposited by the non-

Time (UT)		log(T) of thermal component	EM (cm^{-3})
Impulsive phase	15:26	7.098	10^{48}
HXR peak	$\sim 15:27:20 - 15:28:20$	7.19	3×10^{48}
Right after SXR peak	$\sim 15:35:39 - 15:36:34$	6.88	4.1×10^{49}
Into the decay phase	14:48:20	6.5	2×10^{49}

Table 3.2:: Fitted temperature of the hotter component of the thermal plasma during various stages of the flare.

thermal electrons up until that instant:

$$U_e^{cumulative}(t) = \sum_{t'=t_0}^t U_e(t')$$

3.3 Results

We plot the estimated thermal and non-thermal energy as a function of time in Fig. ??a. The black solid curve with crosses and red solid curve shows the evolution of thermal energy estimated using DEM and temperature from AIA and GOES light curves, respectively. Note that, since GOES does not provide any spatial information, in order to obtain the effective volume we first estimate the loop length using RTV scaling (??). For this purpose we use the EM obtained from GOES and assume a volume filling factor of 1. Note that since the RTV scaling implicitly assumes that the flare arcade is in mechanical equilibrium, the effective volume estimated using this method will only be applicable during the decay phase of the flare. Since, the assumption of filling factor to be 1 may also be susceptible to uncertainties, we also compute and plot the thermal energy evolution curve using $f = 0.4$ (green solid line with triangles) and $f = 0.2$ (blue solid line with squares). We also over plot, the thermal energy that is computed using the EM and temperature obtained from GOES but the volume inferred from STIX soft X-ray contours, under the assumption that $V \sim A^{\frac{3}{2}}$ (purple dotted line).

The interesting trend in Fig. ??a is that the thermal energy calculated from the constrained DEMs (solid black curve with crosses) is closer to a volume filling factor $f = 0.2$ (solid blue curve with squares) in the impulsive phase, but is asymptotic with a filling factor $f = 1$ (solid red curve) during the decay phase. This result indicates that the flare loops during the impulsive phase do not fill up apparent volumes similar to those in the decay phase. The change in the effective filling factor is indicative of the sharp change in the volume during the impulsive phase.

The lime green solid line with circles in Fig. ??a, shows the cumulative energy in the non-thermal electrons. This quantity is the amount of energy deposited at the flare foot points, and one of the sources of the thermal energy of the flare. The cumulative non-thermal energy of electrons $\simeq 1.2 \times 10^{31}$ erg > peak thermal energy calculated from the DEM estimates $\simeq 5 \times 10^{30}$ erg.

For the 2020 November 29 event, the *STEREO-A* perspective looks down into the supra-arcade plasma sheet. Thus the LOS of this feature can not be calculated as demonstrated in Section ?? for the supra-arcade pixels. For the supra-arcade fan pixels in the FOV, we assume a LOS $\simeq 8$ Mm, as suggested in several other studies (see e.g., ???). We use these calculated LOS maps, along with Eqn. ?? to estimate the thermal energy as a

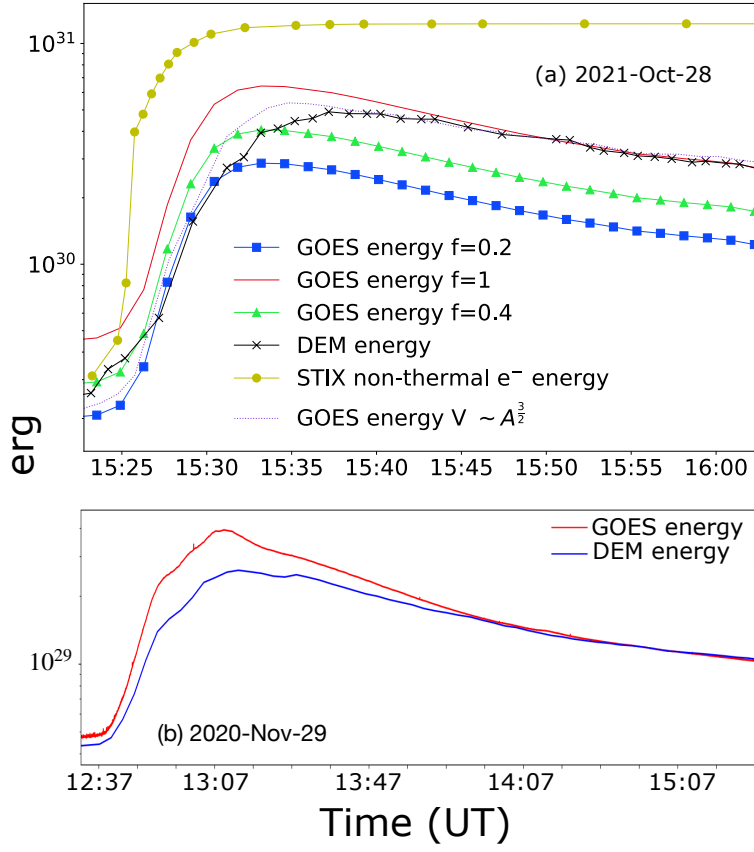


Figure 3.7: Panel (a): Temporal evolution of thermal energy for the 2021 Oct 28 flare as measured using GOES light-curve using the effective volume and a filling factor $f = 1$ (solid red), $f = 0.4$ (green triangles), $f = 0.2$ (blue squares), thermal energy calculated from GOES light curve, but the volume inferred from the area of the of the flaring arcade with STIX SXR images, under the assumption that $V \sim A^{\frac{3}{2}}$ (purple dotted), and DEM obtained from AIA observations (black crosses). We also plot the evolution of non-thermal energy as estimated from STIX (lime green circles). Panel (b): Temporal evolution of thermal for the 2020 Nov 29 flare as measured from GOES light curves with a constant effective volume (solid red) and that calculated from the DEMs inferred from the imaging and a varying volume from the imaging (solid blue).

function of time and plot it in Fig. ???.b. The blue solid curve shows the thermal energy calculated from the DEMs. The red solid curve shows the thermal energy calculated from the GOES light curves and the constant effective volume calculated assuming an RTV loop with a volume filling factor $f = 1$. The thermal energy estimated from the GOES observation, using the effective volume obtained from the RTV approximation is clearly an overestimate in the impulsive phase. But similar to the previous scenario, it is a good estimator of the thermal energy in the decay phase.

There have been several studies that suggest that the plasma in the fan is directly heated (??????). Unlike the flare arcade, the thermal output of the fan is not directly related to the energy deposited by the non-thermal electrons and ions at the foot point. Hence, this different mechanism should also be reflected in the time evolution of the thermal output of the fan, compared to the thermal output of the loops. Under the assumption of the LOS ~ 8 Mm in the fan region, we separately calculate the contribution from the fan to the total thermal energy for the 2020 Nov 29 event.

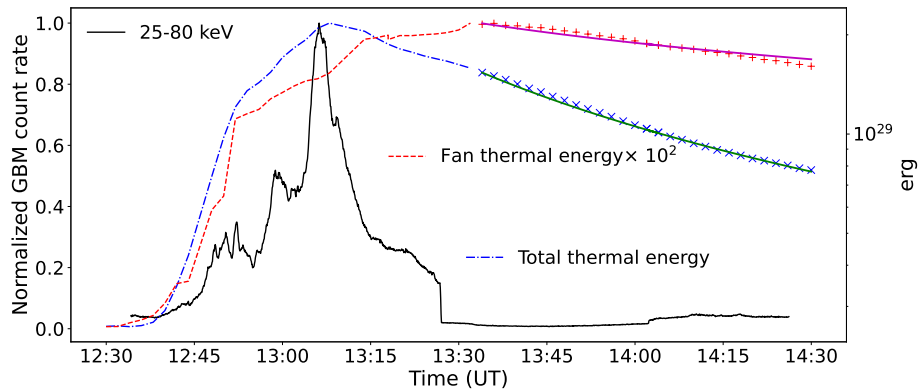


Figure 3.8: Calculated thermal energy for the 2020 Nov 29 flare. The total thermal energy (blue dot-dashed) in comparison to the thermal energy from the fan (red dashed) and the Fermi hard X-ray count (black solid). The magenta and the green solid line show the fit to the thermal energy output to the fan and the loop's thermal output.

Fig. ?? shows the thermal energy of the fan as a function of time (red dashed line) in comparison to the total thermal energy of the 2020 Nov 29 event (blue dot-dashed line). The thermal energy form the fan is \sim two orders of magnitude lower than the total thermal energy of the event. The thermal energy of the fan also peaks much later (~ 20 minutes) compared to the total thermal energy. After the thermal energy of the fan peaks, the thermal energy of the fan (red + sign) and the total thermal energy of the event (blue crosses) are fitted with a power law of the form $at^{-\delta}$ as a function of time. The fits are shown with magenta and green solid line for the fan and the total thermal energy, respectively. The value of the power law index are -0.95 and -1.1, respectively, for the fan and the total thermal output. The plots shows that the thermal energy of the fan decay slower compared to the total thermal output. The normalized *Fermi* GBM 25 – 80 keV count rate (black solid line) peaks at a similar time as the total thermal energy of the event.

3.4 Summary and Discussion

We have used AIA, SUII, and XRT observations to calculate DEM maps and estimate the thermal energy for two solar flares as a function of time. In addition, we have also used

CHAPTER 3. SOLAR FLARE ENERGY

observations from AIA and *STEREO-A* to calculate the geometry of the flare loops and estimate the LOS for the AIA observations. To constrain the non-thermal energy in the 28 October, 2021 event, we have used STIX observations.

Our findings suggest that a single value of volume filling factor is inadequate to describe the evolution of thermal energy throughout the duration of the flare. As such we need to estimate the volume of the flaring plasma as a function of time. In Fig. ??, the thermal energy calculated from *GOES* with various filling factors demonstrates this concept perfectly. During the impulsive phase, the thermal energy calculated from the DEMs is consistent with $f=0.2$, and later in the decay phase, it is consistent with $f=1$. This result demonstrates how the volume of the flare arcade is changing over time with respect to the volume in the decay phase. The thermal energy calculated from $V \sim A^{\frac{3}{2}}$ assumption agrees well with the thermal energy calculated from constrained DEMs in the decay phase. But it still predicts higher energy in the impulsive phase. This discrepancy signifies that the assumption of self-similar expansion may not be valid at the initial sharp rise in the impulsive phase for some flares. Our results are in line with the findings of ? (For details, please refer to Tab.5 therein and the corresponding discussion).

Our results also demonstrate the utility of estimating the volume from different vantages as a function of time. For events like the X-class event on 2021 October 28, the on-disk imaging allows the estimation of the volume from the flare ribbon area under the assumption of self-similar expansion. But for scenarios like the limb event 2020 November 29, where the flare ribbons are not visible from any imaging observation, or the visible foot point and/or visible portions of the loop are projected at a very high angle, estimating the volume of the loop by calculating the height of the loop at various points serves as an important tool in estimating the thermal energy at various phases of the flare.

These results demonstrate that the accurate determination of volume can have significant implications for thermal energy estimates as well as partition between thermal and non-thermal energies. While the former related to the total energetics of the flares, the latter relates to the efficiency of converting the energy deposited by non-thermal electrons into the thermal energy of the ambient plasma.

For the 2020 November 20 flare, we have also estimated the thermal energy for the fan and compared the evolution of the thermal energy of the fan with respect to the total thermal energy of the event. In Fig. ??, the thermal energy from the fan (red dashed line) is \sim two orders of magnitude lower than the total thermal energy of the event (blue dot-dashed line). The thermal energy also peaks much later (\sim 20 minutes) compared to the total thermal energy. This result shows that the fan plasma is being heated directly by a process different from the flare arcade (e.g. SADs (?), plasma flow turbulence (?)). The fan also cools slower than the arcade, which indicates that either continuous heating is present in the fan during the decay phase of the flare or there is suppression of cooling (e.g. ?). The event had both foot points occulted from the Earth's perspective, so it is a fair assumption that most of the hard X-ray is from the loop top coronal source. This circumstance explains

CHAPTER 3. SOLAR FLARE ENERGY

the near-simultaneous peak in *Fermi* hard X-ray (black solid line) and the thermal energy peak from the flare.

Our results exhibit the importance of different solar missions that can observe the Sun with higher spatial resolution (to resolve the finer structures better) and from various vantages (to triangulate the geometry). The ability to spatially resolve the temperature structure of the flaring plasma not only gives us a better estimation of the thermal energy, but it also allows us to spatially separate various portions of the flaring plasma (e.g. for the 2020 November 29 event, we could separate the contribution of the fan from the total thermal energy). This separation enables us to demonstrate that a different heating mechanism was at play in the fan. However, we do note that the reliability of any such estimations needs to be rigorously tested with observations of various flares from various geometric projections.

Chapter 4

Forward modelling SUIT observations

4.1 Introduction

The remarkable technological progress attained in the last few decades has yielded significant benefits in the form of highly advanced imaging, spectroscopic, and polarimetric instruments designed for astronomical observations. These instruments have empowered us with the ability to scrutinize the Sun with exceptional detail. While some of these are ground-based telescopes, the others operate from space. Primarily, space-based instruments observe the Sun in Ultraviolet (UV), extreme ultraviolet (EUV), and X-ray bands, capturing radiation from upper atmospheric layers such as the transition region and corona, which emit due to their elevated temperatures. Various studies of the Sun over the last few decades have successfully uncovered the physical properties of the gas in the upper layers of the solar atmosphere using the observations recorded by X-ray imaging (*Hinode* X-ray Telescope (*Hinode*/XRT, ?)) and spectroscopy (the Spectrometer/Telescope for Imaging X-rays on *Solar Orbiter* (*SO*/STIX, ?)) and Extreme Ultraviolet (EUV) imaging (Atmospheric Imaging Assembly on the *Solar Dynamic Observatory* (*SDO*/AIA, ?), Extreme ultraviolet Imaging Telescope on *Solar and Heliospheric Observatory* (*SoHO*/EIT, ?), Solar Ultraviolet Imager on the *Geostationary Operational Environmental Satellites* (*GOES*/SUVI, ?), the Extreme Ultraviolet Imager on *Solar Terrestrial Relations Observatory-A* (*STEREO-A*/EUVI, ??), the Extreme-Ultraviolet Imager on *SO* (*SO*/EUI ?)) and spectroscopy (*Hinode*/EIS, ?), among many others. The *Transition Region and Coronal Explorer* (*TRACE*, ?), the Solar Ultraviolet Measurements of Emitted Radiation on *SoHO* (*SoHO*/SUMER, ?) and the *Interface Region Imaging Spectrograph* (*IRIS*, ?) allowed us to probe the chromosphere and the transition region in detail. These missions provide us with continuous full disk and Region of Interest (RoI) coverage of the Sun over the X-ray and EUV wavelengths. The situation is rather different in the Near-Ultraviolet (NUV) regime. There is clearly a lack

CHAPTER 4. SUIT FORWARD MODEL

of continuous coverage of the full solar disk in this wavelength range.

One of the key challenges of carrying out solar observations in the UV regime from the ground is the strong attenuation by the Earth's atmosphere. One of the first stratospheric balloon-borne instruments was flown in 1970 and 1971 by ? to circumnavigate this. The instrument carried a 20 cm telescope that imaged the sun in 200–460 nm. The Rasolba balloon experiment was composed of a 30 cm telescope with an ultraviolet spectrograph. They obtained high-resolution spectra of the Sun in the spectral range 190 – 295 nm (??). Sunrise (??) is a balloon-borne observatory that followed up these instruments to observe the Sun in the Near UltraViolet (NUV) regime with a telescope of 1 m diameter. It has flown twice, in June 2009 and June 2013, respectively and provided us with high-resolution imaging in 214, 300, 312, 388 and 397 nm with the Sunrise Filter Imager (SuFI, ?) in 2009 and at 214, 279 and 397 nm in 2017 (?), Dopplergrams and vector magnetograms in Fe I 525.02 nm with the Imaging Magnetograph eXperiment (IMaX, ?) at various locations on the solar disk. During these two flights, along with quiet sun and active regions, Sunrise observed various solar phenomena, e.g. emerging flux events (?), properties and dynamics of moving magnetic features around pores (?), proper motion of bright points in quiet sun and active regions (?), properties of fibrils (?) etc. These observations demonstrated the wealth of information this wavelength range carries and opened the path for full disk coverage of the Sun in the NUV.

The Solar Ultraviolet Imaging Telescope (SUIT; ??) is one of the seven payloads onboard the Aditya-L1 mission (??) of the Indian Space Research Organization (ISRO), launched on September 2, 2023. The satellite is placed in a halo orbit around the Sun-Earth L1 point. With its eleven science bandpasses (eight narrow bands and three broad bands), *SUIT* has the unique capability to probe different heights in the solar photosphere and chromosphere, helping us to understand various physical processes responsible for the transport of mass and energy from one layer to another. Moreover, *SUIT* provides the unique opportunity to measure the spatially resolved solar spectral irradiance in the NUV, which is central to our understanding of Sun climate relations.

SUIT is designed to continuously provide full-disk and RoI images of the Sun, with a 0.7" pixel size. It can track the RoIs while compensating for the differential rotation (?). Moreover, it can detect and localise flares with onboard intelligence and can automatically control the exposure time to avoid saturation. The main science questions that *SUIT* aims to address are (??):

- Coupling and dynamics of the solar atmosphere: *How is energy channelled and transferred from the photosphere to the chromosphere in the solar atmosphere?*
- Sun-Climate Relationship: *Understanding the Variability of Solar Spectral Irradiance (SSI) and NUV radiance of various features on the Sun.*
- Solar Flare Dynamics and Energy Distribution: *At Which wavelength Do flares emit*

CHAPTER 4. SUIT FORWARD MODEL

the majority of their energy, and what proportion of this energy is from the NUV Range? What is the spectral energy distribution of flares?

- Physics of eruptions at various spatiotemporal scales: *what physical processes drive eruptive phenomena observed at various spatiotemporal scales in the Photosphere and Chromosphere?*

In this work, we aim to forward model the observations recorded by *SUIT* using the Max Planck Institute/University of Chicago Radiative Magneto Hydrodynamics (MURaM, ?) and MPS-ATLAS codes as well as observations recorded by the Interface Region Imaging Spectrograph (*IRIS*). MURaM is a three-dimensional (3D) MHD code designed to facilitate realistic simulations of magneto-convection and other related magnetic features (such as pores, sunspots and emerging flux) in the upper convection zone and photosphere. The simulation includes the effects of non-gray radiative transfer, partial ionization, full compressibility and open boundary conditions. The simulation gives us various physical quantities such as density, temperature, magnetic flux density etc. The MPS-ATLAS (?) code, which solves the radiative transfer equation varies rapidly with the help of opacity distribution functions, can be applied to the model atmosphere obtained from MURaM to synthesize the spectrum. Since the MURaM simulation cubes used here do not include the non-local thermodynamic equilibrium, these cannot be used to forward model the observations for chromospheric filter. Therefore, for this purpose, we utilize the observations recorded by *IRIS* in Mg II lines. **The Mg II h & k lines, located at approximately 2803.5 and 2796.3 Å, respectively, are among the most prominent spectral features in the near-ultraviolet (NUV) range.** These lines are primarily formed in the upper chromosphere and the lower transition region (?), making them valuable diagnostics for studying chromospheric dynamics and heating. The Mg II lines exhibit core reversals due to non-LTE (local thermodynamic equilibrium) effects, providing insights into velocity flows, turbulence, and heating mechanisms in the solar atmosphere. Their strong sensitivity to temperature and density variations makes them particularly useful for investigating solar flares, where enhanced emission in these lines indicates energy deposition in the chromosphere.

The rest of the **chapter** is structured as follows. In §?? we briefly describe details of the payload and present the effective area of various filter combinations. We present our method for calculating intensity maps from model atmospheres computed from MURaM, using MPS-ATLAS in §??. We present the measured point spread function (PSF) for the eleven science filters of *SUIT* and the effects of the instrument PSF on the imaging in §?? with the calculated intensity maps presented in §?? and *IRIS* observations. Finally, we summarize and conclude in §??.

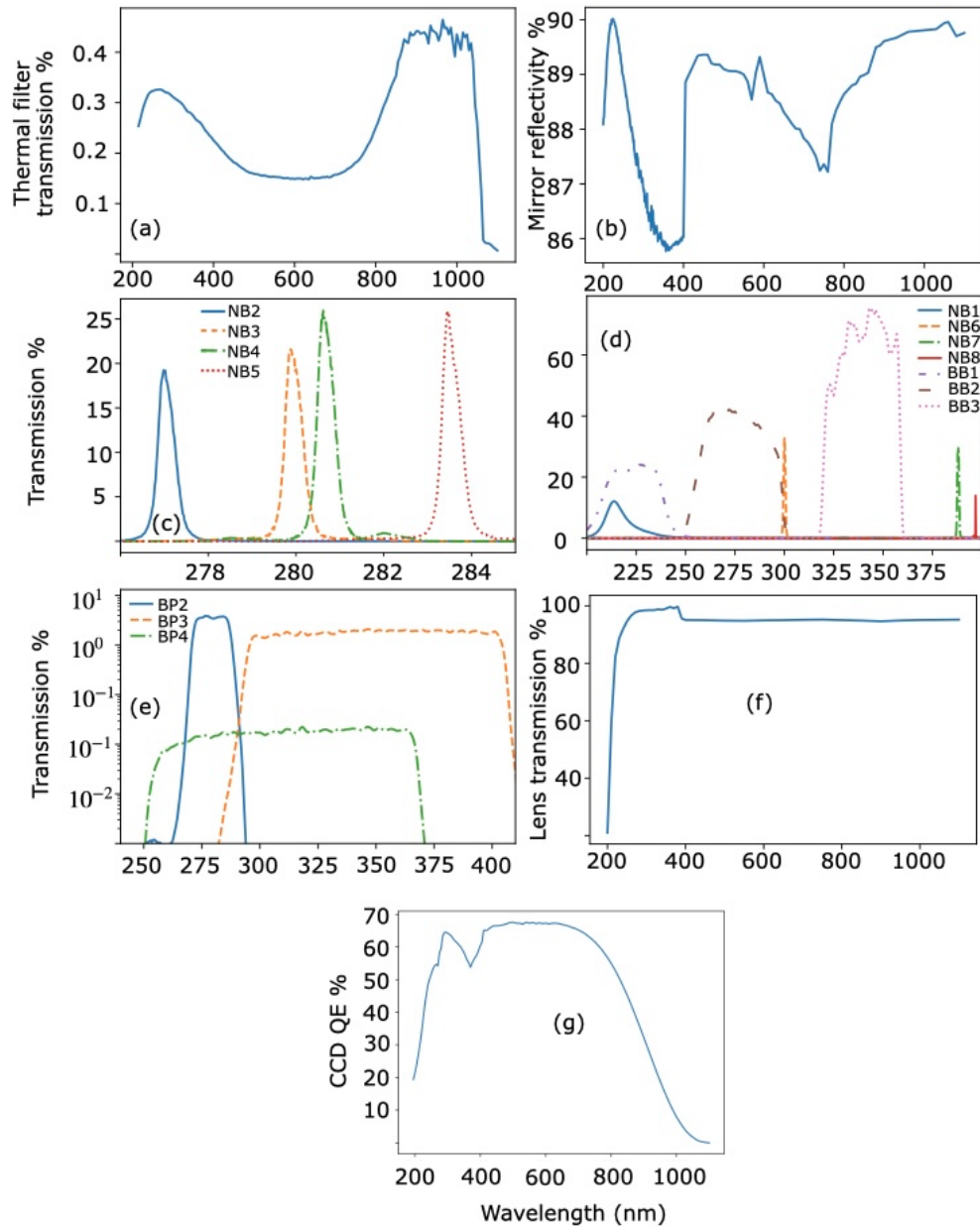


Figure 4.1: Transmission as a function of wavelength of thermal filter (panel a), science filters (panels c and d), band pass filters (panel e) and the field corrector lens (panel f). We also plot the reflectivity of the mirrors in panel b and the quantum efficiency curve of the detector (panel g). Labels on x-axes are wavelength in nanometers.

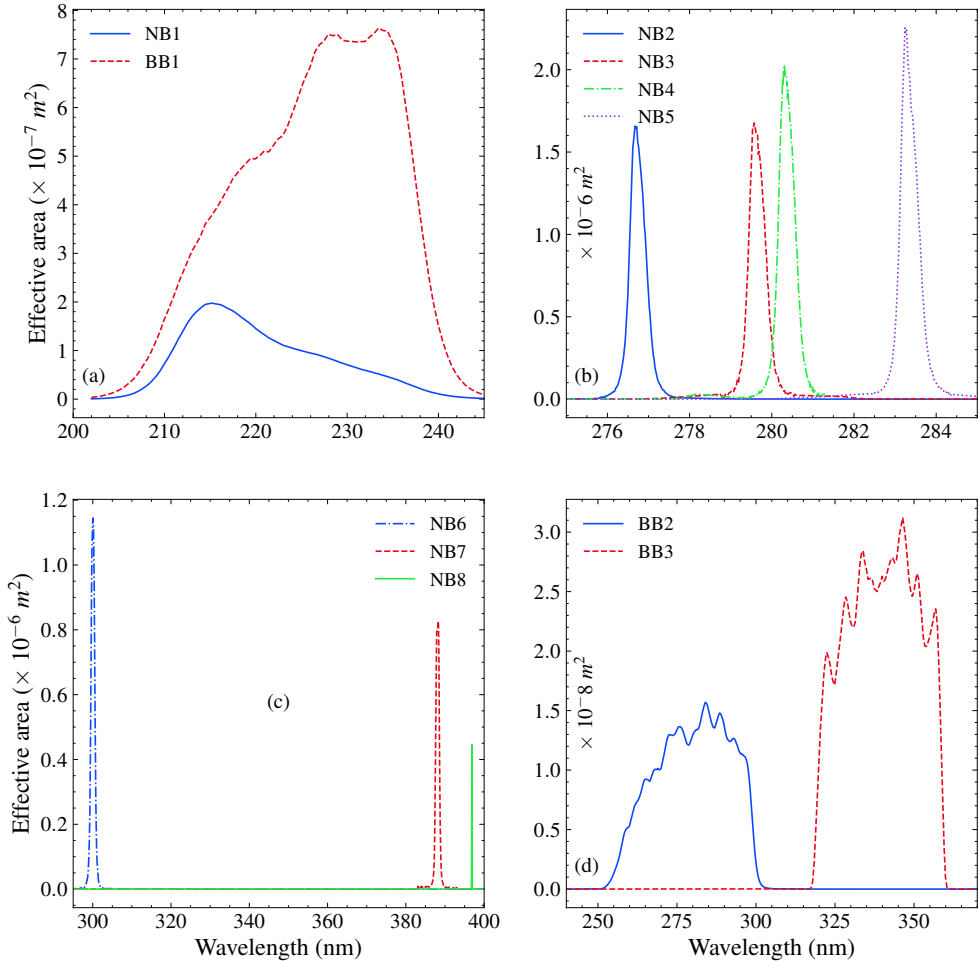


Figure 4.2: The effective area curves for all science filters as labelled.

4.2 The Instrument

The *SUIT* is a two mirror off-axis telescope, which is designed to image the Sun with a plate scale of $0.7''$, and a field of view (FOV) of 0.75° on a 4096×4096 charged coupled device (CCD), which has $12\ \mu\text{m}$ pixel size. The entrance of the payload consists of an entrance door mechanism and a thermal filter(TF). The TF (??) is designed to cut down most of the incoming visible ($\approx 99.75\%$) and infrared($\approx 99.5\%$) radiation and transmits a very small fraction ($\approx 0.3\%$) of the radiation within 200–400 nm. The transmitted light passes through the telescope and gets reflected from the primary and secondary mirrors, respectively, to arrive at the shutter mechanism, which is located between the secondary mirror and the filter wheels. For more details on the instrument, see ??.

SUIT has 11 science filters (first column Table ??) and five bandpass filters (BPFs), which are used to keep the photon flux within the dynamic range of the CCD. Out of these five bandpass filters, while two are the spare copies NB08 and BB01, we designed three additional bandpass filters, namely, BP02, BP03 and BP04. These 16 filters are mounted on two filter wheels (FWs), each holding eight filters. The combination of the appropriate science filter and band pass filter is achieved by rotating the two filter wheels independently. Note that the secondary piece of BB01 is used as a combination of filter NB01 and BB01. Similarly, NB08 is combined with an identical NB08. Between the FWs and the detectors, a focusing lens is mounted on a piezo motor, which can be used as a focusing mechanism. Fig. ?? displays the transmission profile of the individual components in the optical path.

4.2.1 Effective Area of SUIT

Let $p(\lambda)$ be the incident photon flux on the entrance aperture. The photo-electron count at the detector, also known as Data Number (DN) is given by,

$$DN = \int p(\lambda) R(\lambda) t d\lambda$$

where $R(\lambda)$ is the instrument effective area for the specific filter combination and t is the exposure time. The instrumental response, $R(\lambda)$, is computed by multiplying the measured response of all the optical components along the ray path.

Hence,

$$\begin{aligned} R(\lambda) &= TF(\lambda) \times PM(\lambda) \times SM(\lambda) \times SF_i(\lambda) \times \\ &\quad CF(\lambda) \times L(\lambda) \times QE(\lambda) \times A \end{aligned}$$

where A is the entrance aperture area and $TF(\lambda)$, $PM(\lambda)$, $SM(\lambda)$, $SF_i(\lambda)$, $CF(\lambda)$, $L(\lambda)$ and $QE(\lambda)$ are the measured responses as a function of wavelength of thermal filter, primary

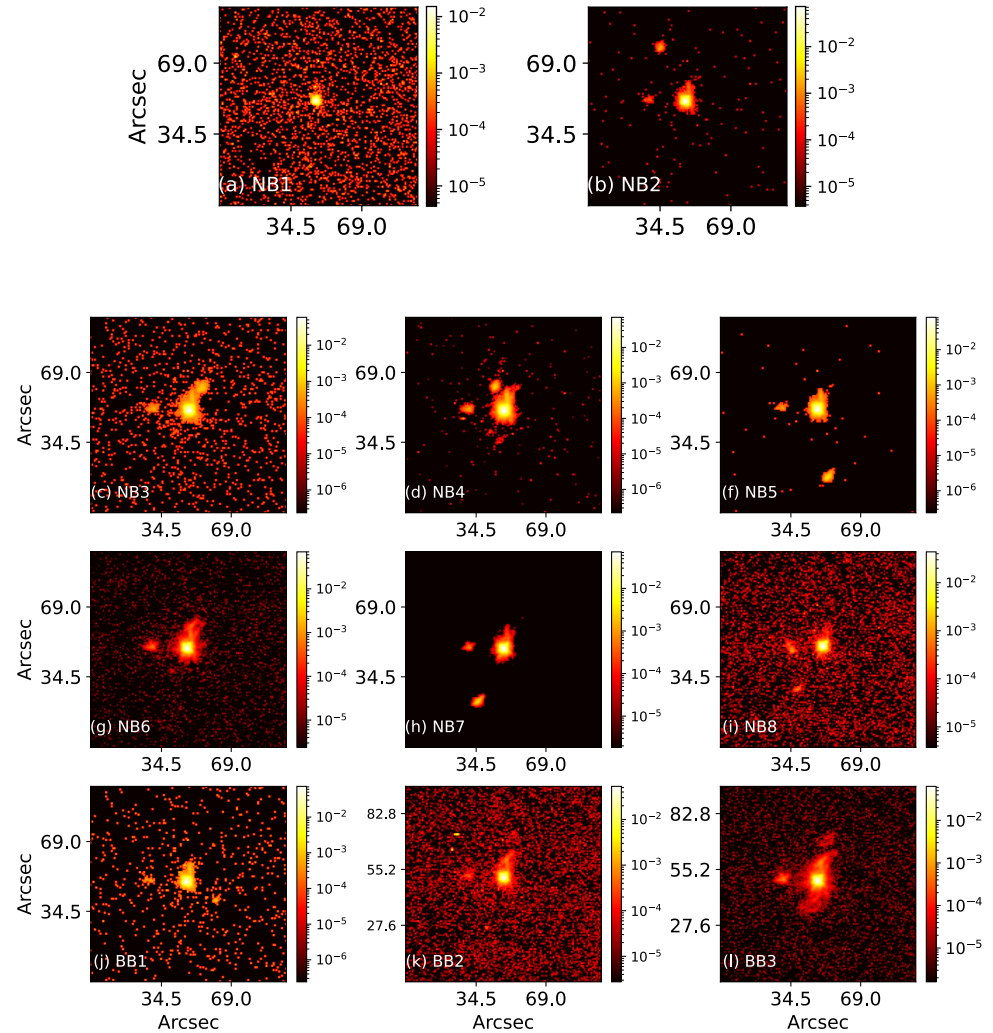


Figure 4.3: The measured PSF for the various filter combinations. The colourmap is area normalized, i.e. the sum of the PSF over the total area is unity.

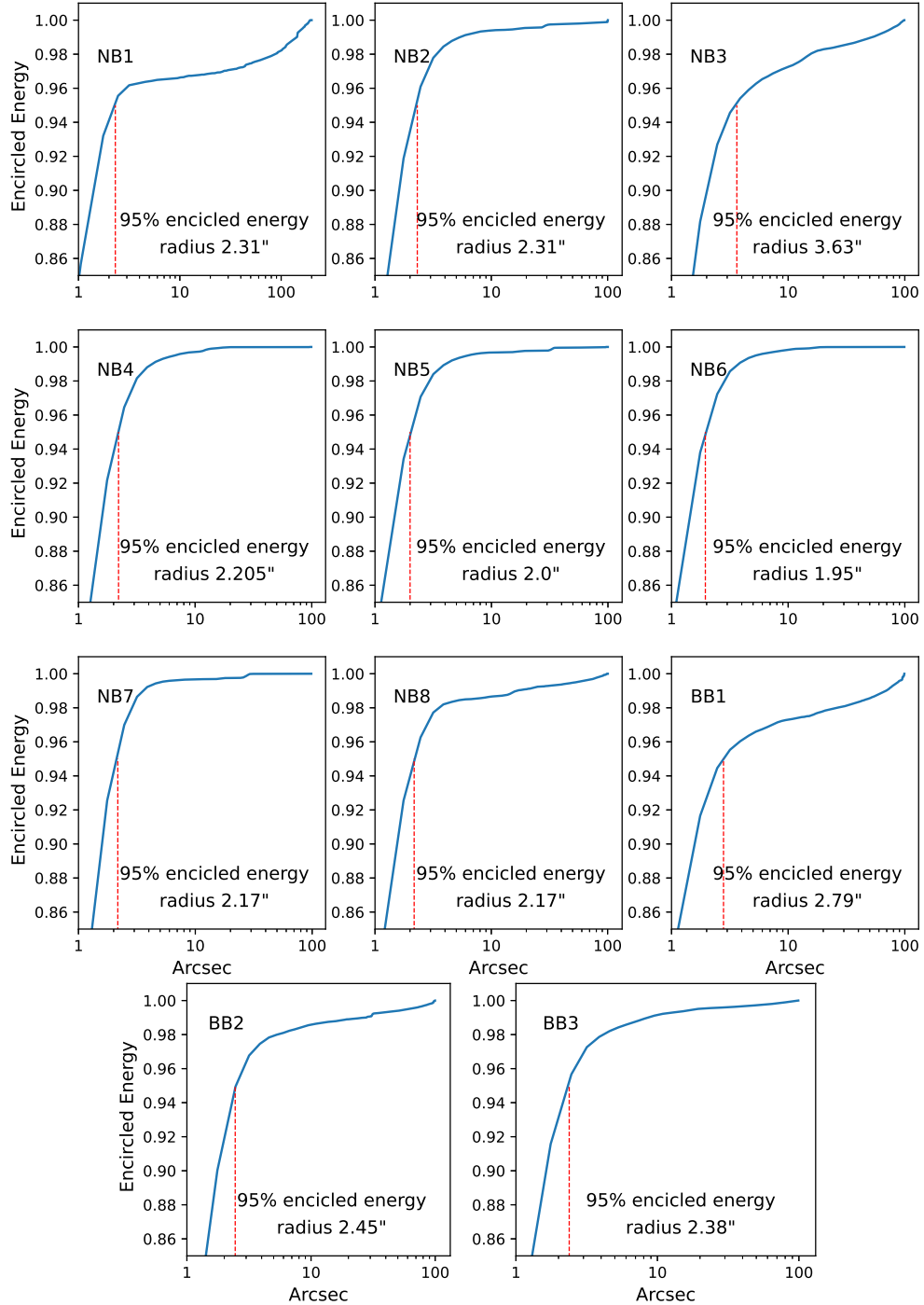


Figure 4.4: The encircled energy curve for the measured PSF. The 95% encircled energy radius are marked with the vertical dashed red line. The angular scale of the 95% encircled energy radius is also quoted in each panel for the specific filter combination.

mirror, secondary mirror, science filters, band pass filters, field corrector lens and the quantum efficiency of the CCD, respectively. The obtained effective area curves for each filter are shown in Fig. ??.

4.2.2 The Point Spread Function (PSF) of *SUIT*

In Fig. ??, we plot the measured Point Spread Function (PSF) at the centre of the CCD for the different science filter combinations for *SUIT*. The PSFs are highly peaked at the centre. The scattered light background becomes clearly visible due to the log scaling of the color bar and is more than two orders of magnitude lower than the peak.

Fig. ?? shows the encircled energy curve for the measured PSFs for various filter combinations normalized to the total integral of unity. The vertical dashed lines in each plot show the radius within which 95% of the incident light falls. For example, for the NB02 filter, 95% of the incident light from a point source arrives within a $2.31''$ radius ($\sim 4.6''$ diameter) and 5% of the light falls outside that region. Note that while the 95% diameter is $4.6''$, the PSF is strongly peaked. The overall diameter is considerably larger than the highly peaked part of the PSF because of the presence of a pedestal in the PSF. The pedestal is visible in all of the cases at the base of the central peak, although it is about 2 order of magnitude lower in all the cases (see Fig. ??). In some cases (e.g. NB01, BB02 etc.) a few or multiple smaller peaks apart from the pedestal are also visible. Similar radii for other filters are quoted in the corresponding panels of Fig. ???. The encircled count curves help us characterize the stray light for various filter combinations.

4.3 Forward Modeling *SUIT* intensity maps using MPS-ATLAS and MURAM

One of the essential steps of characterizing the science filters was to conduct a thorough throughput modeling for the concerned filter combinations. However, quantifying the effects of the wavelength response of the optical components and the PSF on the spatially resolved observations, as well as the contrast variation, requires detailed modeling with resolved simulations of the Sun’s surface. For this purpose, we use the MPS-ATLAS code. It is an updated version of the well established ATLAS9 (?) code that can efficiently generate Opacity Distribution Functions (ODFs), model atmospheres, and calculate emergent spectra in local thermodynamic equilibrium (LTE) for a given wavelength range by solving radiative transfer (RT) equation in plane parallel geometry using the assumptions of local-thermodynamic-equilibrium (LTE).

We use 3D MHD model atmospheres simulated by ? and 1.5D RT with MPS-ATLAS (see e.g., ?, for details) with measured filter profiles of *SUIT*, to calculate the emergent intensity. The 3D MHD simulation employs a symmetric lower boundary condition for the

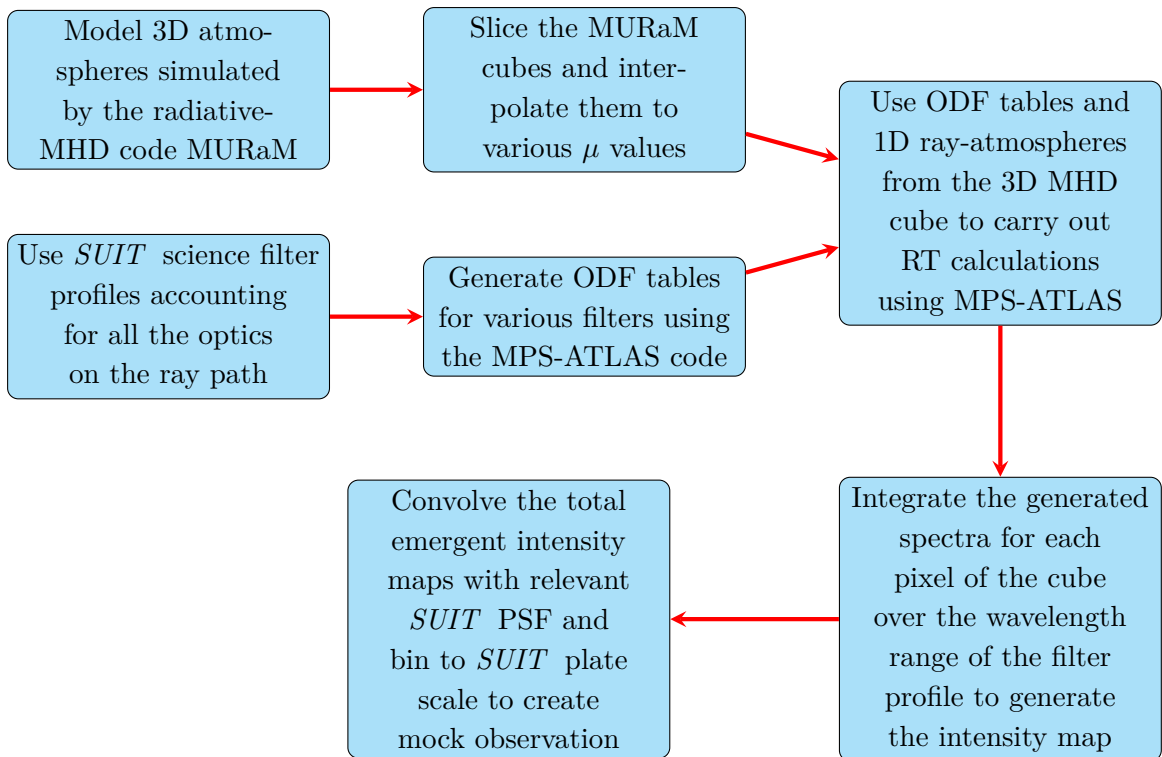


Figure 4.5: The flow chart shows the entire process of generating the simulated intensity maps, from the data cubes and characterizing the filters.

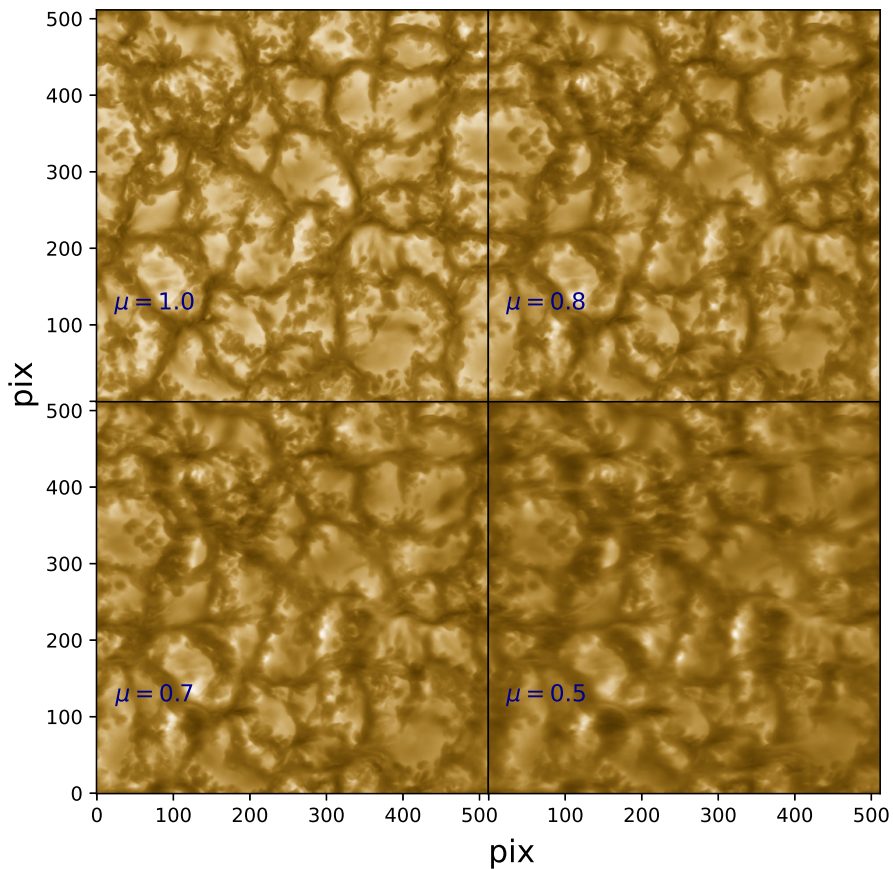


Figure 4.6: Forward modelled intensity maps at various μ values for BB02 filter of SUIT.

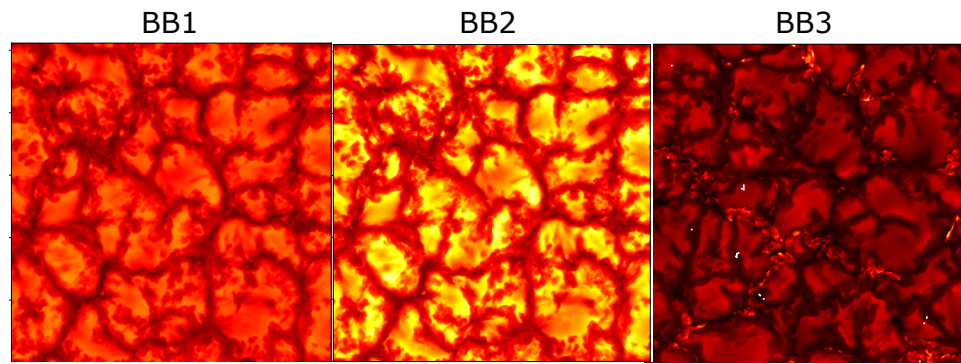


Figure 4.7: Forward modelled intensity maps for various science filters of SUIT.

CHAPTER 4. SUIT FORWARD MODEL

magnetic field and a variety of initial magnetic field configurations to create small-scale variations and various levels of magnetization. The RT equation is solved using the method of ODFs, accounting for both continuum and line opacities within the concerned wavelength range. This takes into account both continuum and line opacity within the concerned wavelength range. Accurately accounting for the line opacity is one of the major challenges in synthesizing spectra over a broad wavelength range. In the ODFs method, the opacity is sorted without the information of the corresponding wavelength within small intervals of wavelengths known as bins. The geometric mean of the sorted opacity values for multiple sub intervals within a given wavelength bin is pre-tabulated over atmospheric parameters such as temperature, pressure and micro-turbulent velocities. During RT calculations, opacity is then interpolated for the required grid parameters of the atmospheric model. The primary goal of the ODF method is to significantly minimize the computational time required for RT calculations. This becomes particularly crucial when computing emergent spectra across numerous atmospheres, such as those arising from 3D MHD simulations.

? developed an optimized method using the MPS-ATLAS code that allows us to use an arbitrary filter profile instead of a rectangular filter profile. We use this method, with our measured effective area, to forward model intensity maps for NB01, NB02, NB05, NB06, NB07, BB01, BB02 and BB03 filter combinations that *SUIT* is using.

We describe the end-to-end procedure in Figure ???. The 3D MHD model atmospheres are sliced at various angles and interpolated to various Line of sight (LOS) angles. As described earlier, the ODF tables are generated for various atmospheric parameters, such as temperature, pressure and micro-turbulent velocities, for the measured science filter profiles. The generated ODF tables are used to solve the RT through the model atmosphere using the MPS-ATLAS code. This provides us the emergent intensity as a function of wavelength for all the rays of the model atmosphere. Integrating this intensity across the wavelength range, we determine the total emergent intensity for each filter.

Figure ?? displays the *SUIT*'s BB02 intensity maps obtained at various μ values, namely $\mu = 1.0, 0.8, 0.7$ and 0.6 , respectively. The spatial scale of the region is $(9 \text{ Mm} \times 9 \text{ Mm})$ with (512×512) pixels, with a pixel size of $\simeq 0.025''/\text{pixel}$. This is at a much higher resolution than that of *SUIT*, which is $\sim 0.7''/\text{pixel}$. Moreover, these intensity maps do not include the effects of the instrument point spread function (PSF). Therefore, we first need to convolve the computed intensity maps with the measured PSF of *SUIT*, and then bin it to *SUIT* plate scale to obtain synthetic observables that are comparable to *SUIT* observations. Fig. ?? displays the simulated intensity maps for the *SUIT* BB filters across the same MURaM cube.

We use the MURaM and MPS-ATLAS codes to forward model the observations for NB01, NB02, NB06, NB07, BB01, BB02 and BB03. We note that since the MURaM simulations studied here cannot be used for the chromospheric filters, namely NB03 (Mg II k), NB04 (Mg II h) and NB08 (Ca II k), we have used observations recorded by *IRIS* to forward model the NB03 and NB04 filter observations. *IRIS* also provides spectra corresponding to

the continuum filter NB05. Hence, we forward model NB05, also using *IRIS* observations. Forward modelling of SUIT observations using *IRIS* data is straightforward as we do not need to use any MHD simulation cube and RT code. However, the convolution with the spatial PSF and the application of the spectral filter profile, etc. still must be carried out. For our analysis, we use dense raster scans from *IRIS*. The dense rasters usually have $\sim 0.33\text{--}0.4''$ per pixel spatial resolution. This spatial resolution is half of the pixel size of *SUIT*. In addition to that, the 95% encircled energy radius for most of the *SUIT* filter combinations is $\sim 2''$. Hence, we can safely ignore the instrument characteristics of *IRIS*. For the two filters where we are using *IRIS* data, the bottom right box in Fig. ?? is replaced by *IRIS* observations.

4.3.1 SUIT filters forward modeled with MPS-ATLAS

Following the procedure described above, we forward model the intensity maps in NB01, NB02, NB06, NB07, BB01, BB02 and BB03. Since the spatial extent of the simulation box is much smaller compared to the size required to reliably convolve with the *SUIT* PSF, we stitched the same simulated box multiple times to be able to convolve with the measured PSFs of *SUIT*. This could be done without problems due to the use of periodic boundary conditions in the MURaM simulation setup. Fig. ??a displays the stitched images obtained for BB03. In Fig. ??b, we display the corresponding image that is convolved with the PSF of the respective filter of *SUIT* and binned to its plate scale.

To compare the intensity contrast before and after the convolution, we plot intensity across a small part of the vertical (panel c) and a horizontal cut (panel d). The blue curves represent the intensity cut through the MPS-ATLAS simulated intensity maps, while the orange dashed curves are for convolved-binned intensity maps. The contrast variation across the cuts reproduces the intensity peaks and troughs in similar regions. These intensity cuts demonstrate that we can reproduce the intensity contrasts in the forward-modelled data with reasonably similar spatial positions. The forward-modelled observational features appear broader, with reduced contrast. This reduction in contrast, is anticipated given the difference in the plate scale of simulation and that of forward-modelled observations. The 95% encircled energy is largely $2''$ for most filter combinations (see Fig. ??). This would imply that the intensity from a point source would be redistributed to a circle of $2''$ radius. So, if we have two equally bright/dark point sources, they would be merged if the distance between them is $2''$ or less. Hence, we should be able to study contrast variation at the spatial scale of $\sim 2''$ using *SUIT* observations. We have performed this exercise on all the filters corresponding to the photosphere and continuum and have obtained similar results.

4.3.2 NB03 & NB04

As alluded earlier, to forward model NB03 and NB04 observations, we have used *IRIS* archival data. The *IRIS* obtains UV spectra with high spatial ($0.33\text{--}0.4''$ per pixel), temporal

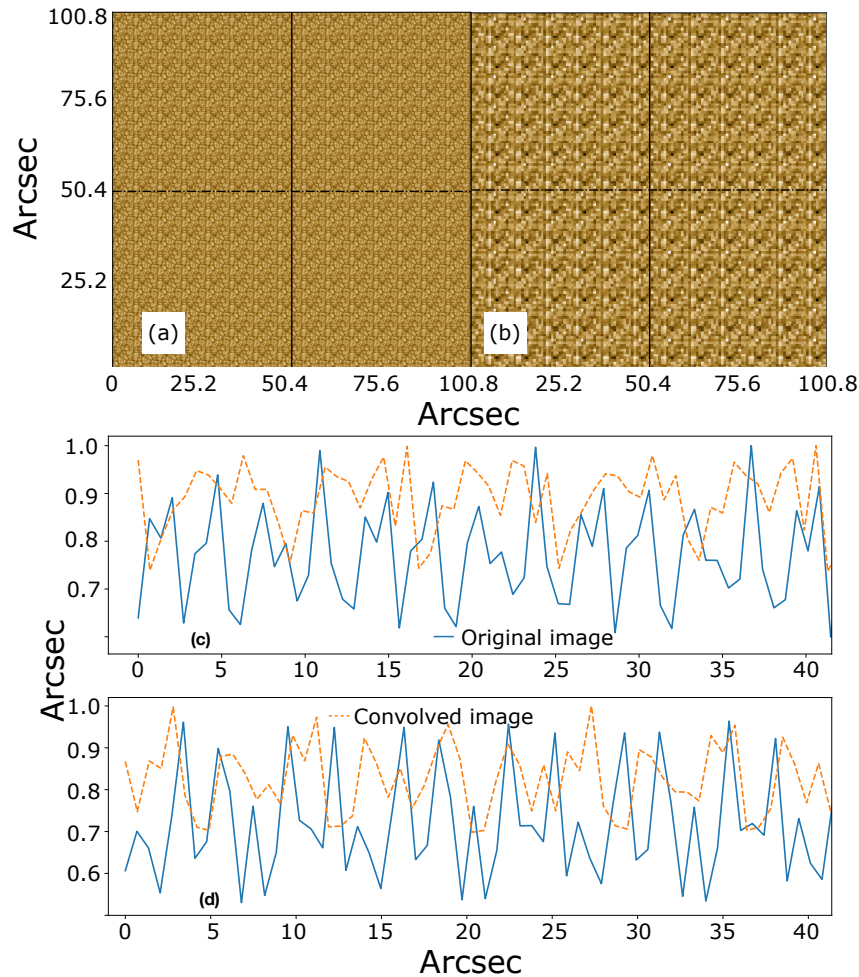


Figure 4.8: The effects of convolution on the simulated BB03 intensity map. Panel a) MPS-ATLAS simulated BB03 intensity map. Panel b) convolved and binned BB03 intensity map. The normalized intensity variation along the horizontal and vertical black lines are plotted in panel c and d, respectively. The blue curves correspond to the simulated BB03 filter, whereas the orange curves correspond to convolved binned data.

(1s), and spectral resolution (~ 26 and ~ 53 mÅ) and images of the scanned regions using the slit-jaw imager. In the spectral channels, the strongest lines that *IRIS* regularly observes are C II, Mg II and Si IV. Here we use the very large and dense 320 step raster observation from 11th July, 2023 of a sunspot in AR 13363. The sunspot was located at the heliographic position of $\sim [-180'', -397'']$. The *IRIS* raster had a FoV of $\sim [112'', 175'']$. We use *iris_getwindata.pro* available in the *sswidl* distribution to get the calibrated spectra over the raster FoV. This gives us the calibrated spectra for all the pixels in the raster FoV in units of $erg.cm^{-2}.s^{-1}.sr^{-1}.pix^{-1}$. We multiply the entire spectra of each pixel through the NB03 and NB04 effective area (see Fig. ?? panel b) and convolve with the measured PSF (see Fig. ??) to forward model NB03, NB04 observations. Consequently, the observed intensity is,

$$DN_{NB03} = \int IRIS_spec(\lambda) R_{NB03}(\lambda) t d\lambda$$

and

$$DN_{NB04} = \int IRIS_spec(\lambda) R_{NB04}(\lambda) t d\lambda$$

where R_{NB03} and R_{NB04} are the measured effective area for the respective filter combinations. Fig. ??a shows the *IRIS* raster FoV intensity map in the Mg II k line. The *IRIS* image convolved with NB03 (NB04) PSF and binned to the *SUIT* plate scale is shown in Figs. ??b(c).

To compare the intensity contrast obtained from *SUIT* images with those from *IRIS* observations, in Figs. ??e & f, we plot the normalized intensity profiles along the vertical (panel d) and horizontal (panel e) lines shown in panels a, b and c for NB03 and NB04 as labelled. The horizontal white dotted line encounters a light bridge on the western end of the sunspot (marked with a white arrow in Fig. ?? panels a, b & c). We see three dips in the intensity profile in Fig. ?? panel e, as the horizontal white dotted line encounters the sunspot thrice. In both panels d & e, NB03 (orange dashed line) and NB04 (black dot dashed line) has a lower contrast (peak to trough variation) compared to *IRIS* (red solid line) and NB04 (black dot-dashed line) contrast. This is in line with our measurements of the PSF for NB03 & NB04, as the measured PSF for NB03 has a higher scatter component in the background compared to NB04 (see panel c & d in Fig. ??, Fig. ??). Therefore, NB03 has a higher radius for 95% encircled count (see NB03 and NB04 in Fig. ??). A higher radius for 95% encircled count results in lower contrast in the convolved mock NB03 map.

4.3.3 NB05

The NB05 channel (with the central wavelength at 283.2 nm) is also observed by *IRIS*. Therefore, we use the *IRIS* 2832 Å window observation of the same AR 13363 mentioned in §???. In Fig. ??a, we plot the integrated intensity of the *IRIS* 2832 Å window. In panel b we

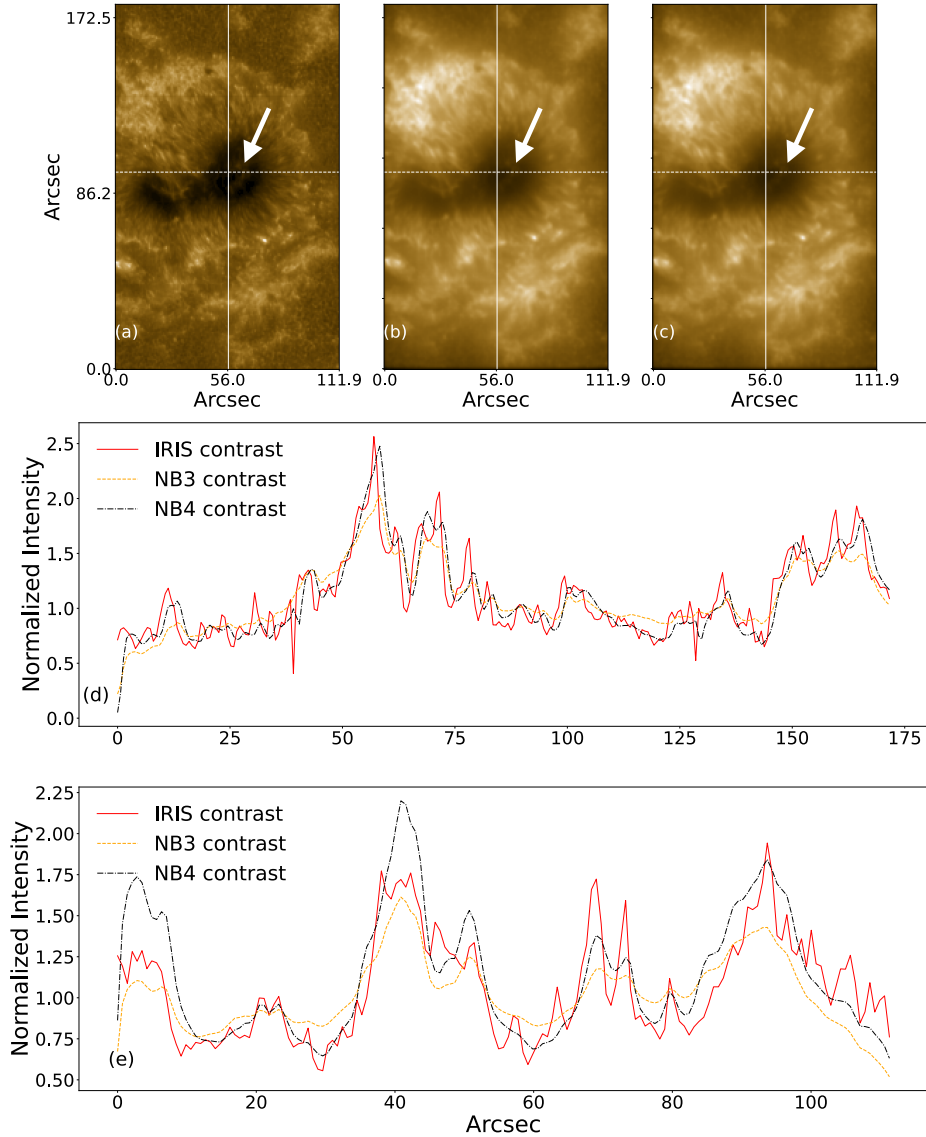


Figure 4.9: Effects of convolution on the *IRIS* raster observation with the NB03 & NB04 PSF. Original (panel a), convolved with NB03 PSF and binned to *SUIT* plate scale (panel b), convolved with NB04 and binned (panel c) *IRIS* intensity maps obtained in Mg II k. Normalized intensity variation along the vertical-solid (horizontal-dashed) white line marked in panel a, b & c are shown in panel d (panel e). Red-solid curves correspond to original *IRIS* image, orange-dashed curves correspond to mock NB03 and black dot-dashed curves correspond to NB04.

CHAPTER 4. SUIT FORWARD MODEL

plot the same region passed through the NB05 effective area and convolved and binned to *SUIT* plate scale. In panels c and d we plot the normalized *IRIS* intensity (red solid line) and normalized *SUIT* NB05 intensity (orange dashed line) along the white dashed line and blue solid line marked in panels a and b, respectively. The features marked ('1' & '2') in panels a and b are also marked in the normalized intensity variation panel e. Although there is a significant loss in contrast, the features are still identifiable. As demonstrated previously, various features are reproduced in the same spatial location with reduced contrast.

We have also used a very large, dense 320-step raster observation from 20th July 2023 of a sunspot in AR 13376 to create the mock observation. The sunspot was located at the heliographic position of $\sim [-147'', 325'']$. The *IRIS* raster had a field of view (FoV) $\sim [112'', 119'']$. As described earlier, we forward modeled *SUIT* observations in the NB05 passband for this region. In Fig. ?? panel a we plot the integrated map obtained in *IRIS* 2832 Å window. In panel b we plot the same region passed through the NB05 effective area and convolved-binned to the *SUIT* plate scale. In panel c(d) we plot a cropped view of the sunspot in the southern part of the region in *IRIS* 2832 Å (*SUIT* NB05 convolved). The light bridge within this sunspot narrows in thickness as we move from the upper-left to the lower-right. We take multiple measurements close to one another and average them to calculate the thickness of the light bridge at some specific location. In the northern part, the lightbridge is $\sim 2''$ thick in the *IRIS* observation and $4''$ in the mock NB05 observation (see upper set of white arrows in panels c and d). It narrows down to $1''$ in the southern part in the *IRIS* observation, and $1.8''$ in the mock NB05 observation (lower set of white arrows).

We take a slice through the sunspot and the light bridge, marked with a vertical white line in Fig. ?? panel c. The intensity along this line for normalized *IRIS* contrast (solid red line) and convolved NB05 contrast (dot-dashed blue line), is plotted in Fig. ?? panel e. The light bridge is marked with a black arrow in the intensity profile.

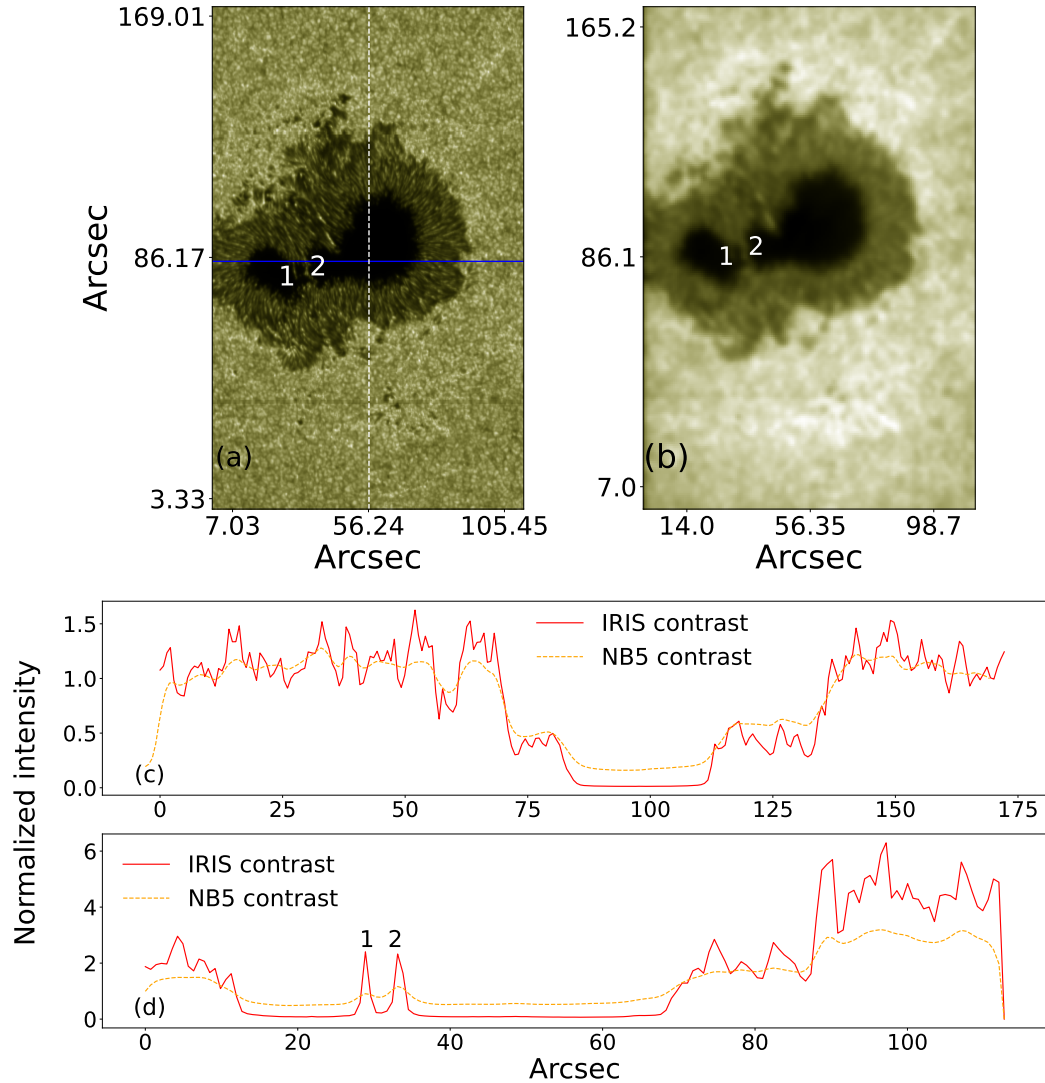


Figure 4.10: Effects of convolution on the *IRIS* raster observation with the NB05 PSF. We plot the *IRIS* raster intensity map obtained in 2832 Å continuum in panel a and the convolved-binned intensity image in panel b. The normalized intensity variation obtained from both images along the white-dashed and blue-solid lines are shown in panels c and d, where red solid lines correspond to the original *IRIS* image and orange dashed lines correspond to the convolved-binned intensity map. The two thin features marked by ‘1’ and ‘2’ within the sunspot in panels a and b are also marked in the intensity variation plot.

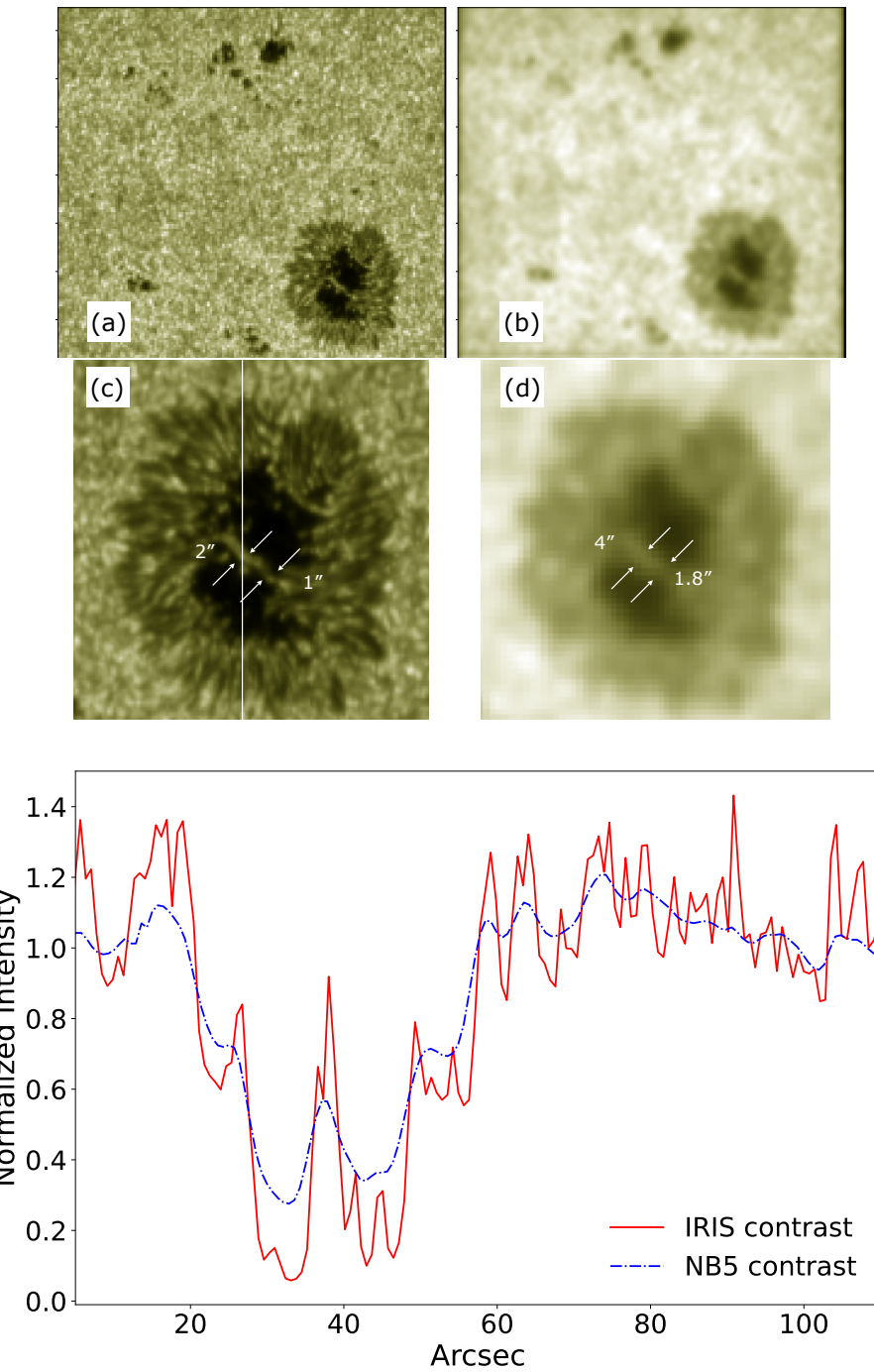


Figure 4.11: Effects of convolution on the *IRIS* raster observation with the NB05 PSF. Panel (a): *IRIS* raster intensity in 2832 Å continuum. A large sunspot with a thin, light bridge in the middle is present in the southern part of the region. Panel (b): The *IRIS* raster observation in panel a convolved with the NB05 PSF (see fig. ?? panel e). Panel (c) & (d): Zoomed view of the larger sunspot in the South in *IRIS* and the simulated *SUIT* NB05 map, respectively. The light bridge in the middle of the sunspot is marked by a set of four white arrows. The thickness of the light bridge at two locations is marked in both the panels. The normalized intensity along the vertical white line drawn in panel (c) is plotted in panel (e). The normalized intensity of the original *IRIS* (mock NB05) observation is plotted in solid red (dot-dashed blue) line. The light bridge is marked in the intensity profile with a black arrow.

4.4 Summary and Conclusions

The observation of any optical telescope is convolved by the PSF of the telescope. The PSF represents the response of the optical system to a point source. It quantifies the extent of blurring of a point source when imaged through the optical system, as well as the effects of various components like scattering, diffraction, etc. We have applied the measured PSF at the *SUIT* detector plane for various filter combinations to the emergent radiation from MURaM simulation cubes (computed by MPS-ATLAS) and to pre-existing *IRIS* observations to create mock *SUIT* observations. The *SUIT* PSF in all of the filter combinations is highly peaked with a pedestal \sim two orders of magnitude lower (see Fig. ??). In most of the filter combinations the 95% encircled count radius is $\sim 1.4 - 2.5''$. This would imply that two equally bright or dark features on the Sun $\sim 2''$ apart would be merged in the corresponding *SUIT* observation. Hence, we could resolve features on a spatial scale of $> 2.5''$ for the corresponding filters in *SUIT* observations. These projections are more relevant for line filters in *SUIT* (e.g. NB03(Mg II k), NB04(Mg II h), NB08 (Ca II h)), as it would exhibit more features in close proximity (bright points in ARs and QS, the plage regions around sunspots, small eruptions in ARs). These projections are made with the measured PSF at the center of the CCD. The PSF distortions increase gradually as we move away from the centre of the CCD, with more angular elongation.

We believe the forward modeling pipeline will help us simulate *SUIT* observations from existing MHD simulations and compare them to real *SUIT* observations to constrain current model parameters. The comparisons with forward-modelled mock *SUIT* observation with real *SUIT* observations over time would also provide useful insights into the degradation of the instrument with respect to the on-ground projections. The deconvolution algorithm would be useful to improve the contrast across *SUIT* observations and spatially localize features more reliably on the solar surface.

Chapter 5

Intital preparatory analysis for SUIT

This thesis chapter originally appeared in the literature as

Photometric calibration and spectral validation of the Solar Ultraviolet Imaging Telescope onboard Aditya-L1, Sarkar, J., Roy, S., Ramaprakash, A.N., et. al., 2025, *J. Astron. Telesc. Instrum. Syst.* 11(1), 014005 (2025), doi:[10.11117/1.JATIS.11.1.014005](https://doi.org/10.11117/1.JATIS.11.1.014005).

5.1 Introduction

SUIT consists of two main sub-units: The *SUIT* optics package - comprising an off-axis Ritchey-Chrétien telescope, and *SUIT* Electronics package - responsible for imaging with the telescope and communicating with the satellite. The main components of the *SUIT* optics package include a multi-operation entrance door, a thermal filter to limit the amount of incoming sunlight, primary and secondary mirrors, a shutter mechanism to control exposure times, baffles to reduce stray and scattered light, a motorized filter wheel assembly, a piezoelectric focusing mechanism, and a CCD detector. Figure ?? shows a schematic diagram of the telescope (For further details, please refer to ?).

SUIT observes the Sun in eleven spectral bands, of which three are broadband (referred to as BB) and eight are narrow bands (referred to as NB), as listed in Table ???. These are used to image different heights of the solar atmosphere, from the photosphere to the chromosphere. In the wavelength range of interest, i.e., 200–400 nm, the solar flux increases by two orders of magnitude, as can be seen in the combined spectrum obtained from solar flux measured by SOLSPEC (see Fig. ??). Therefore, we must employ certain combination filters to control solar flux levels and achieve the best signal-to-noise ratio (SNR) at each bandpass within the nominal exposure time while

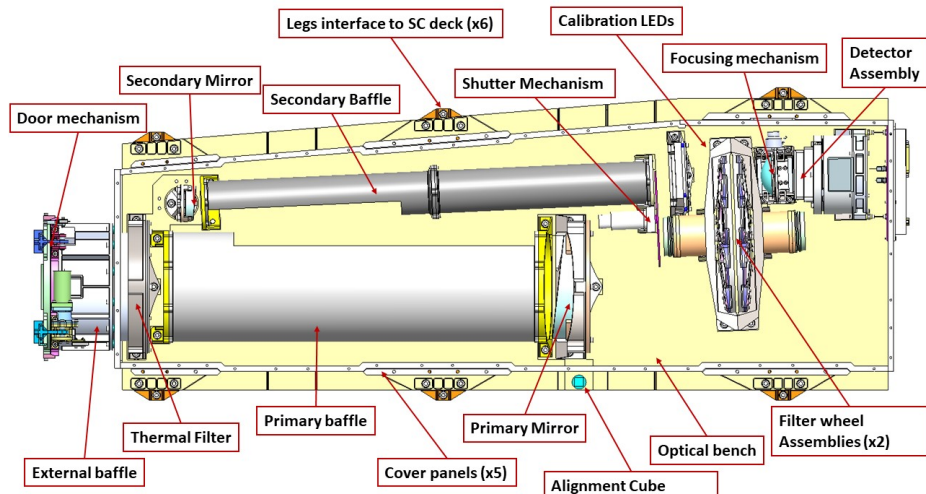


Figure 5.1: Schematic diagram of the *SUIT* telescope.

maintaining the spectral purity of the passband by suppressing leakage of light from wavelength bands outside of the science interest. These combination filters are listed in the second column of Table ???. In total, *SUIT* has 16 filters mounted on two filter wheels, each having eight slots. A given filter combination is achieved by rotating the two filter wheels independently and placing the desired filter combination in the beam path. For example, *SUIT* uses BB1 as a combination filter for BB1, as this particular filter aims to measure the irradiance of the entire Herzberg Continuum. On the other hand, the NB8 filter aims to accurately observe the line core of the Ca II h line (~ 396.85 nm). Several strong flare lines close to the line core go into emission during a flare (e.g. He at ~ 397 nm). Combining NB08 with another NB8 results in lower SNR for a given exposure time, as opposed to combining it with a bandpass filter. But we decided to chose this combination for maintaining the spectral purity at the expense of cadence or SNR. Similar choices regarding spectral purity were made for the band NB7 (CN Band), where we specifically wanted to probe the CN band in the continuum. The position of the various filters on the filter wheel also plays an important role in dictating the cadence of the observations, e.g. the BB filters are usually not planned to be used in normal flare observations. So, the NB filters and their corresponding combination filters have to be arranged in such a way as to minimize the time taken to rotate the filter wheel, achieve the planned filter combination, and maintain an acceptable cadence. The choice of filter combination is a delicate optimization between suppressing the out-of-band leakage and achieving a reasonable SNR within an acceptable exposure time. Additionally, the positions of combination filters on the filter wheel must be chosen to minimize the time spent in rotating the filter wheels from one combination to other dictating the cadence of observation.

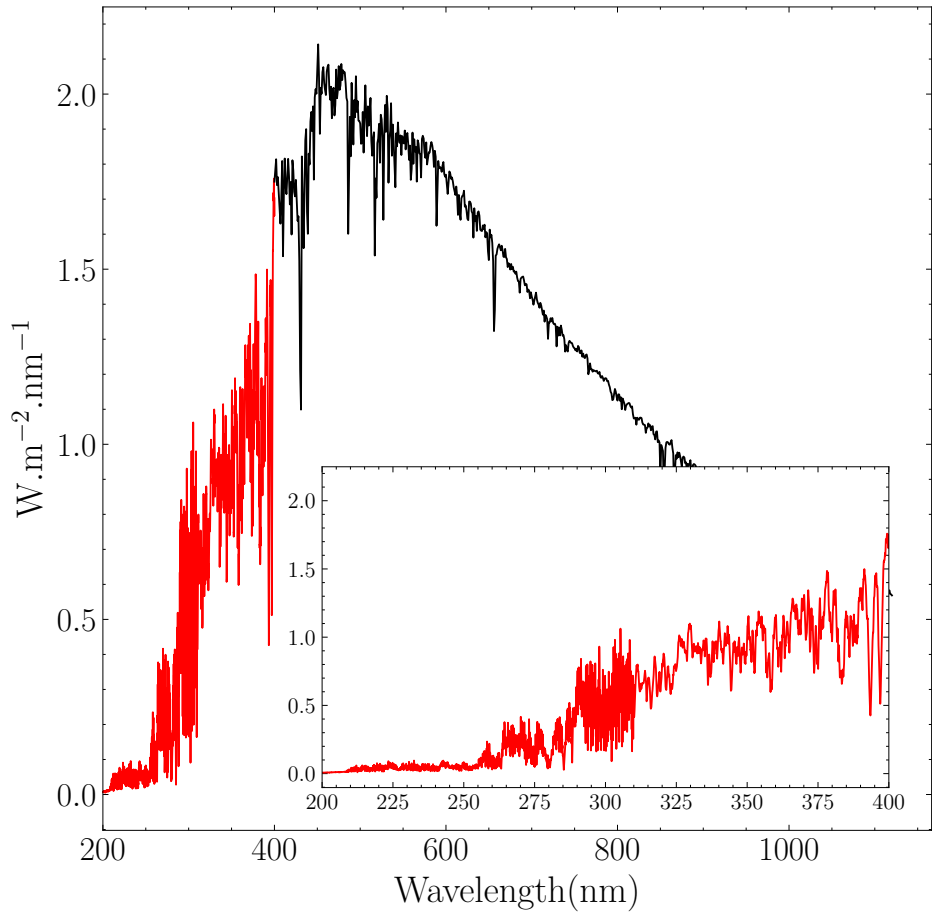


Figure 5.2: The solar spectrum from SOLSPEC. Parts of the solar spectra marked in red show the wavelength range covered by *SUIT*'s observation passbands. The inset plot shows a dramatic rise in solar irradiance within *SUIT*'s observation band.

5.2 Analysis of Spacecraft jitter simulation for *SUIT*

One of the key steps in estimating the imaging performance was to quantify if the RMS level of spacecraft jitter would affect the imaging across various exposure times. For this purpose, we analyzed the simulated spacecraft drift data provided by the ISRO URSC team to quantify the RMS jitter as a function of exposure time. Two main moving components within the payload can generate significant jitter on the payload, namely the shutter vane and the filter wheel (FW) movement. The spacecraft has a filter wheel movement torque compensator in place to minimize the jitter generated by the FW movement. So, four main scenarios were simulated to be analyzed, arranged from least to most amount of jitter:

1. No shutter torque + no filter movement

CHAPTER 5. SUIT PREPARATORY ANALYSIS

Science Filter	Combination Filter	Central Wavelength (nm)	Bandpass (nm)	Science target
NB1	BB1	214.0	11.0	Continuum
NB2	BP2	276.7	0.4	Mg II k blue wing
NB3	BP2	279.6	0.4	Mg II k
NB4	BP2	280.3	0.4	Mg II h
NB5	BP2	283.2	0.4	Mg II h red wing
NB6	BP3	300.0	1.0	Continuum
NB7	BP3	388.0	1.0	CN Band
NB8	NB8	396.85	0.1	Ca II h
BB1	BB1	220.0	40.0	Herzberg Continuum
BB2	BP4	277.0	58.0	Hartley Band
BB3	BP4	340.0	40.0	Huggins Band

Table 5.1:: List of science filters on board *SUIT*. Columns from left to right denote filter mnemonics (including science and combination filters; NB: Narrowband, BB: Broadband, BP: Bandpass), central wavelengths for science filters and corresponding bandpasses, and the observation interest for the filter.

2. Only shutter torque
3. Shutter torque + FW movement + FW compensation torque
4. Shutter torque + FW movement + no FW compensation torque

The Fig. ?? shows the simulated drift for the aforementioned four cases. We did a Fourier analysis of the simulated drift data to characterize the spacecraft jitter from the spacecraft drift. The Fig. ?? shows the power spectrum for the simulated drift shown in Fig. ???. The SUIT imaging channels have a maximum possible exposure ~ 1.4 s, which corresponds to a frequency of ~ 0.7 Hz and lower exposures would correspond to a higher frequency. So, signals in the Fourier transform corresponding to 0.7 Hz or higher are capable of affecting the imaging within the exposure window. We assumed any signal with a frequency 0.5 Hz or greater from the Fourier transform to be Jitter signal. We then took a frequency cut at 0.5 Hz, of the power spectrum to filter the drift from the jitter and then took an inverse FT to reconstruct the jitter signal for the three axis. To calculate the amount of RMS jitter on various time scales relevant in the context of SUIT exposure times, we took the extracted jitter signal and picked out bins of multiple time scales and calculated the RMS jitter for them. We had several bins for each time scale, each of which gave us RMS jitter and maximum jitter within that bin. We averaged all the bins to estimate the RMS jitter and maximum Jitter for that specific timescale. Figures ?? ad ?? shows the RMS and maximum jitter as a function of timescale. SUIT has a $0.7''/\text{pix}$ resolution. Both the average and the maximum jitter even in the worst case scenario, i.e when shutter torque and FW movement is present but the FW movement compensation is not employed, is much lower than the pixel size of SUIT within timescales relevant to exposure times for SUIT. We did not need to account for the jitter while characterizing the imaging performance.

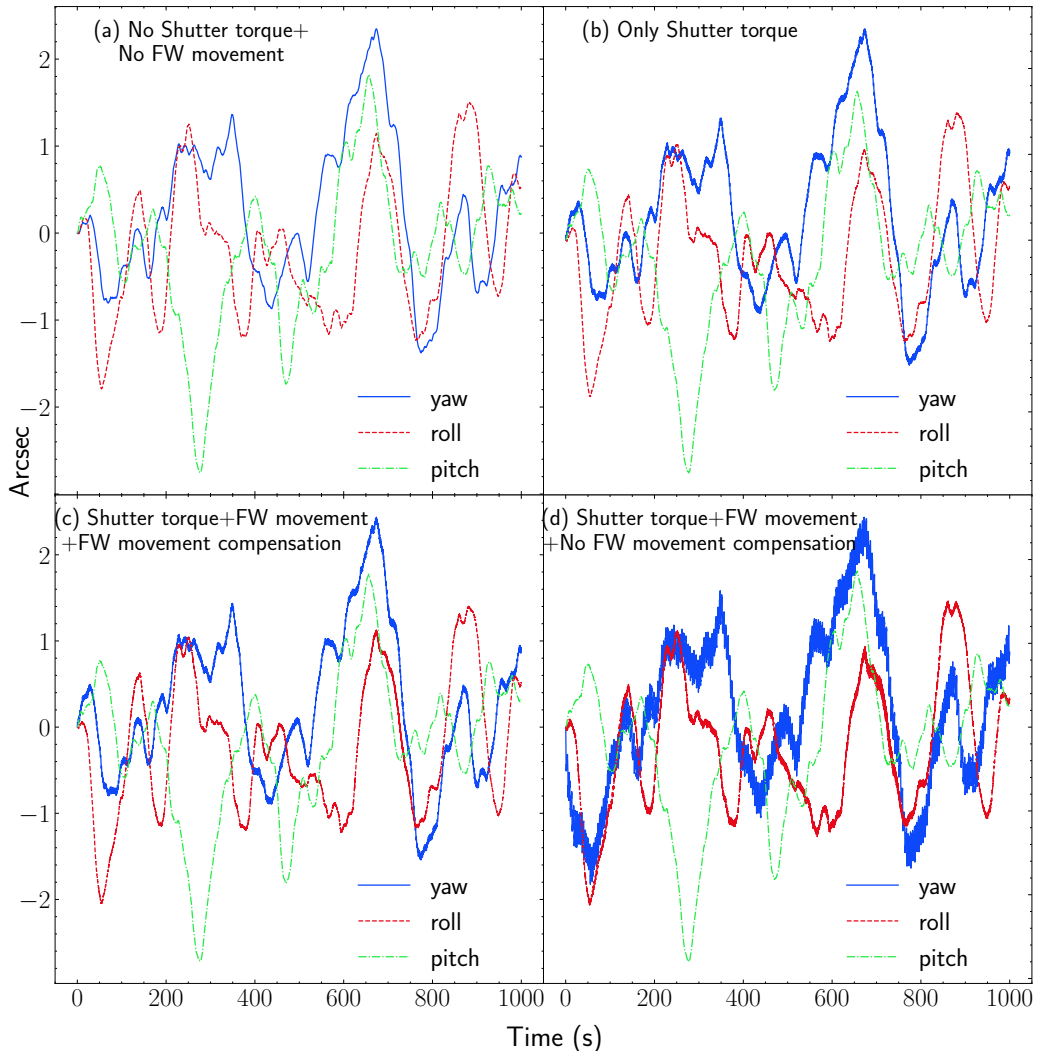


Figure 5.3: The simulated drift for the yaw (blue solid), roll (red dashed) and pitch (green dot-dashed) axis of the payload as a function of time for the aforementioned four cases in §?? in the four panels respectively as marked.

5.3 Throughput model of *SUIT*

The design of the *SUIT* telescope prioritizes throughput and photometric accuracy requirements. Optical parameters of various optical elements, such as the reflectivity of primary and secondary mirrors, transmission of the thermal filter, field corrector lens, spectral transmission of the science filter, and combination filter, are optimized to maximize throughput within their corresponding wavelength ranges.

The optical response of *SUIT* is evaluated based on the solar spectral irradiance and the throughput characteristics of each sub-assembly. Experimental throughput data is com-

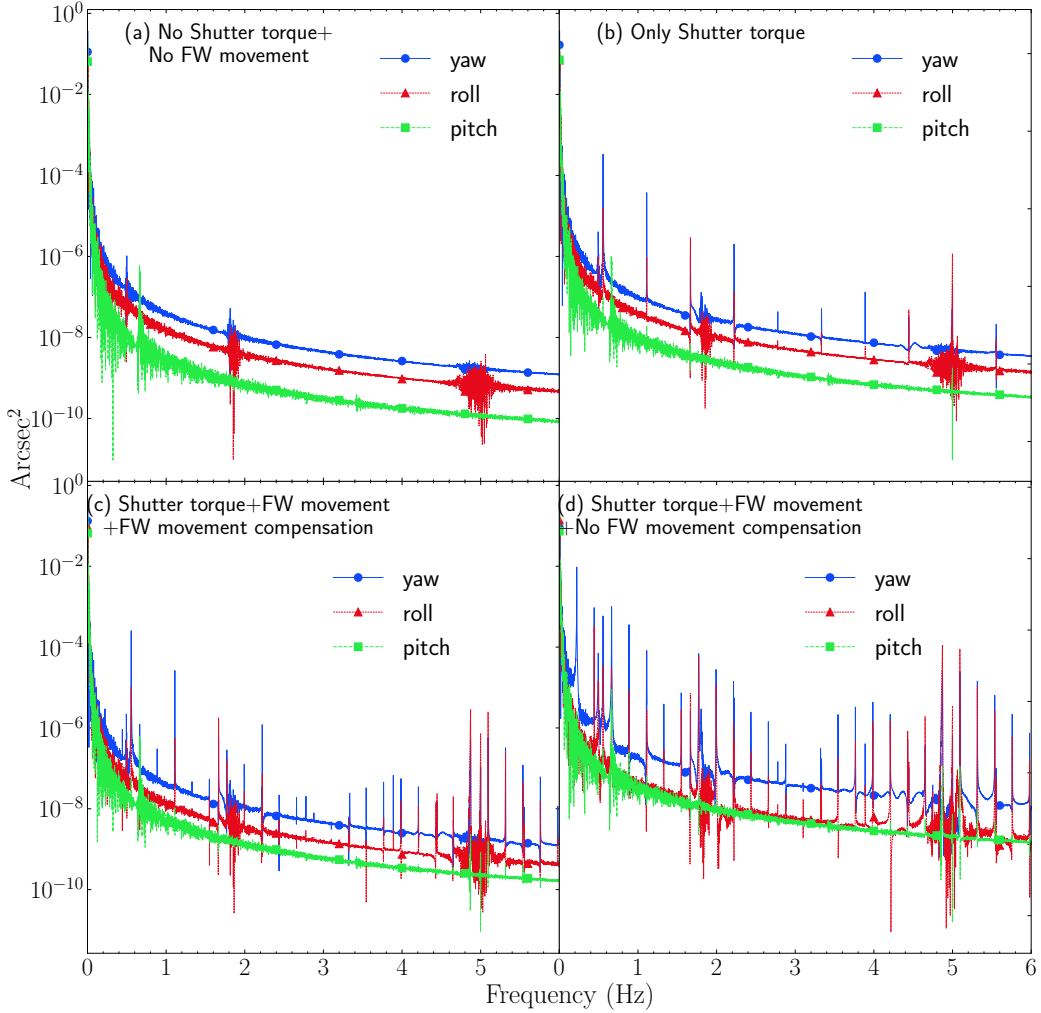


Figure 5.4: Fourier Transform of the simulated drift for the yaw (blue circle), roll (red triangle) and pitch (green square) axis of the payload as a function of time for the aforementioned four cases in §?? in the four panels respectively as marked.

pared with a throughput model to validate the consistency between experimental and simulated results. This validation process is crucial for determining exposure times for the payload across the eleven science bandpasses in different operational modes.

The throughput of *SUIT* is modeled using the Sun-as-a-Star spectrum to predict counts for specific science filter combinations. The measured wavelength responses of individual components are utilized to estimate these counts. If the photon flux incident at the entrance aperture is denoted by $P(\lambda)$, then the recorded data number in the images can be expressed as:

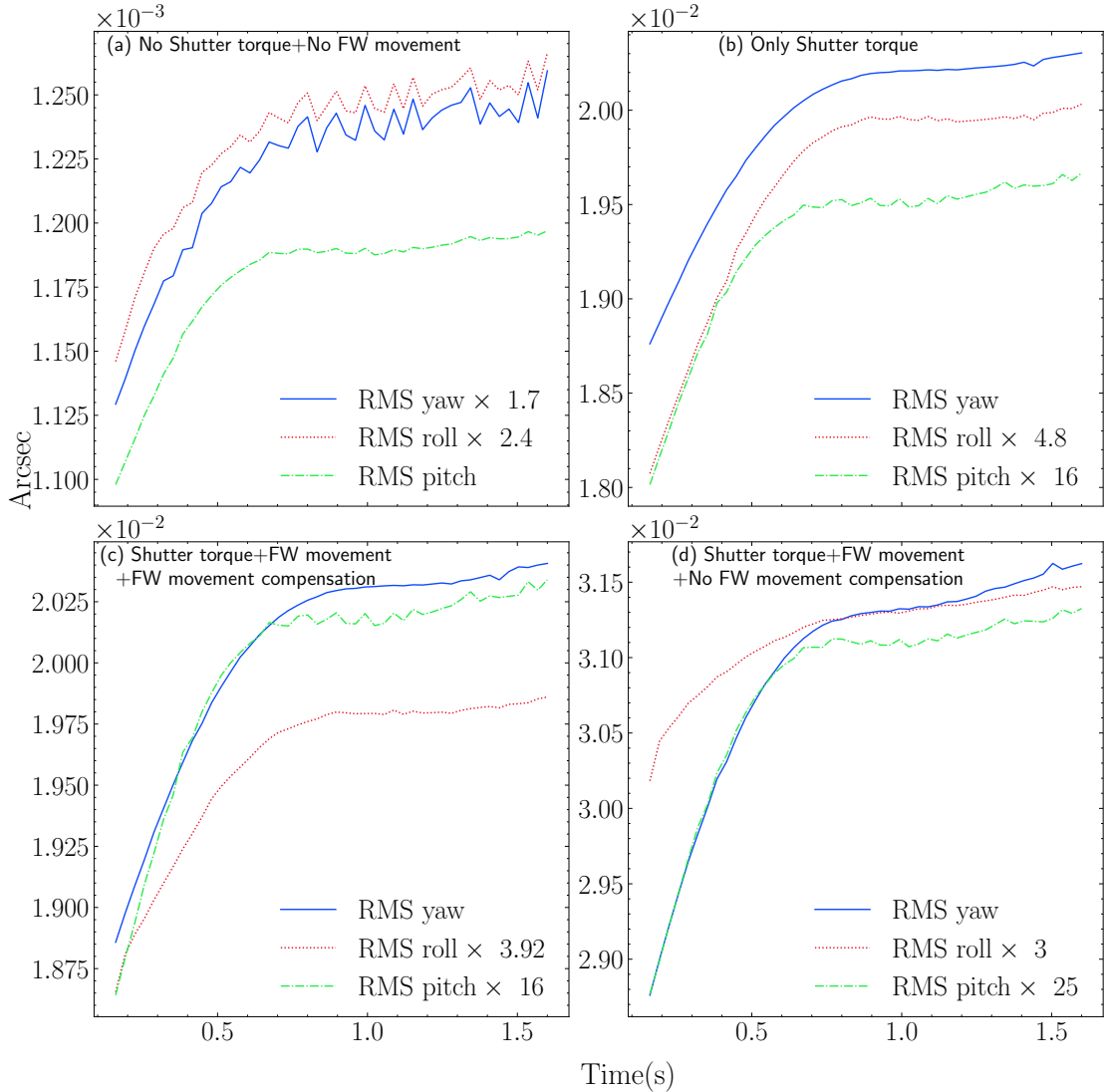


Figure 5.5: The RMS jitter at various timescales for the four scenarios of operation as labelled.

$$DN = \int P(\lambda) R(\lambda) t d\lambda \quad (5.1)$$

where $R(\lambda)$ is the effective area for the specific science filter combination, and t is the exposure time for that filter. The effective area $R(\lambda)$ is derived by multiplying the measured response of all the optical sub-assemblies in the beam path-

$$R(\lambda) = TF(\lambda) \times PM(\lambda) \times SM(\lambda) \times SF_i(\lambda) \times SF_j(\lambda) \times L(\lambda) \times QE(\lambda) \times A \quad (5.2)$$

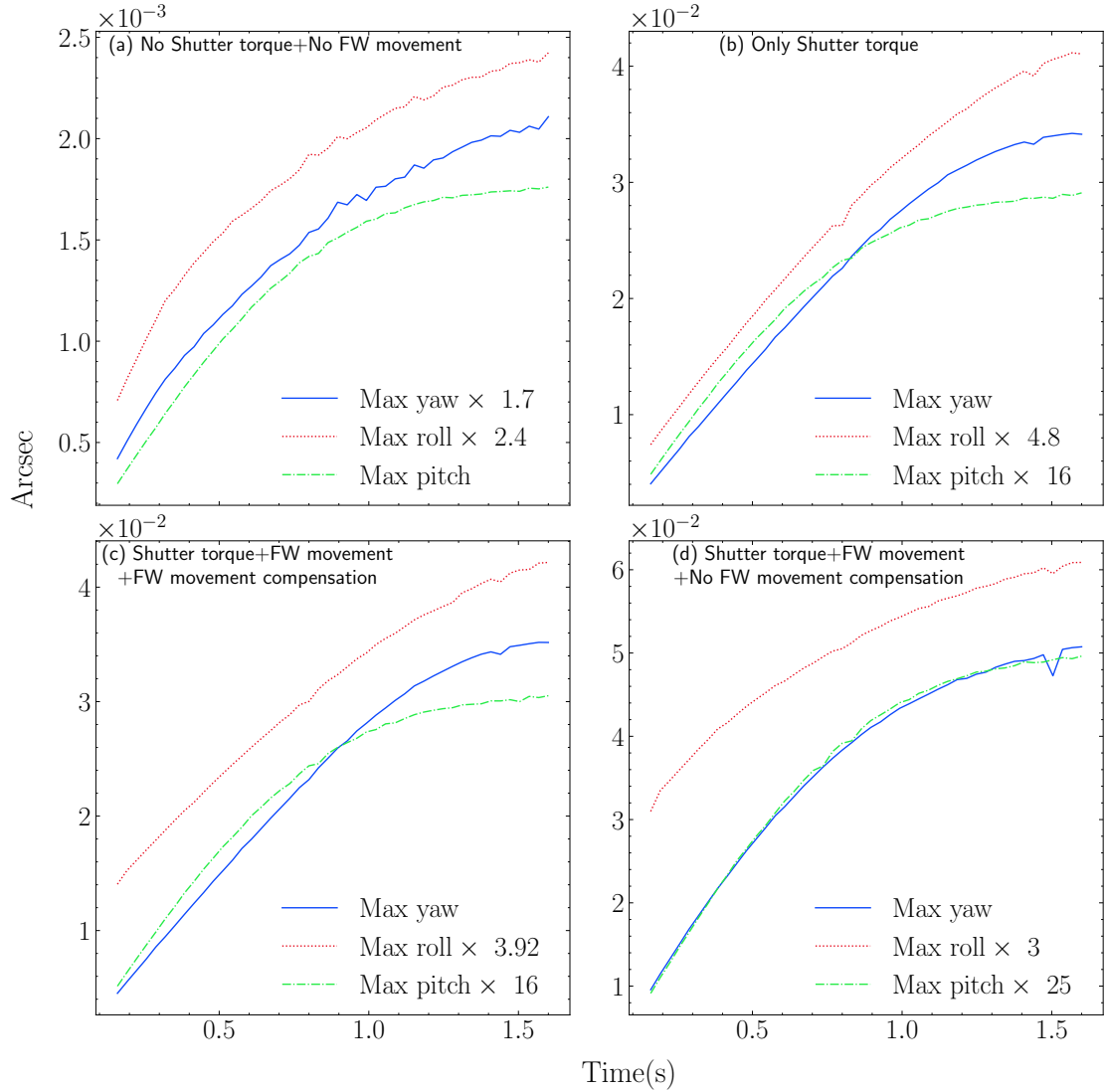


Figure 5.6: The Maximum jitter at various timescales for the four scenarios of operations as labelled.

where $TF(\lambda)$, $PM(\lambda)$, $SM(\lambda)$, $SF_i(\lambda)$, $SF_j(\lambda)$, $L(\lambda)$ and $QE(\lambda)$ are the measured responses as a function of wavelength of thermal filter, primary mirror, secondary mirror, filters in filter wheel 1 and 2, field corrector lens and the quantum efficiency of the CCD. The effective area curves for each filter are shown in Fig. ??.

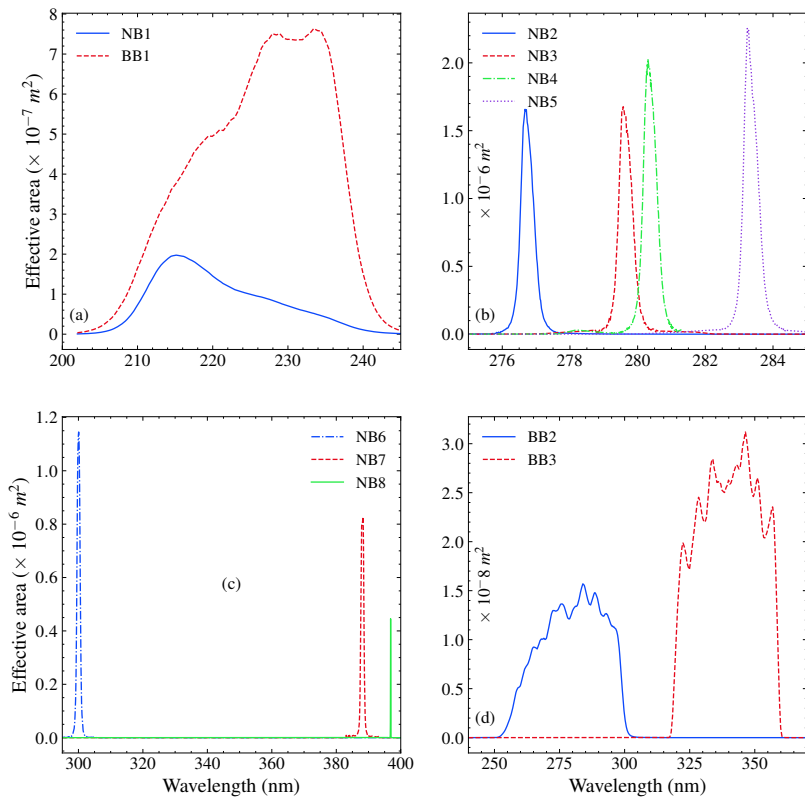


Figure 5.7: The effective area curves for SUIT science filters.

5.4 Choice of Science filters for *SUIT*

One of the key uses of the throughput model is that it allows us to predict the average count from a Sun as a star spectra. under certain assumptions, we can then estimate how much SNR we can expect from the darkest features, *e.g.* sunspots on the sun. The science filters for *SUIT* were manufactured by Materion Corp. As mentioned in Tb. ??, the eleven bandpasses are achieved by combining eight science filters with four distinct combination filters (three bandpasses and two science filters combined with themselves). Materion manufactured several copies of each filter. We chose the best-performing ones out of these, which would eventually mounted on the payload. The selection for the filters was mainly based on the following three criteria:

- The cosmetics of the filters. The intended transmission for individual filters is achieved with custom coating. We would like to choose filters with the least amount of pinholes, scratches and digs, *i.e.* cosmetic damages on the coating. Along with this, we also do not use the filters that have pinholes in the same location on both sides of the filter.
- The average SNR for a Sun as a star observation. We choose the filters with higher average SNR for the filter combinations.

CHAPTER 5. SUIT PREPARATORY ANALYSIS

- We choose the filters with the least amount of out-of-band flux. The out-of-band is defined by wavelength range outside of the 99% effective area about the peak wavelength.

The choice of filter profiles should be an optimization of these 3 criteria.

5.4.1 Exposure Time Calculation

One of the key requirements to calculate the SNR for any science filter combination is to calculate the necessary exposure time, for that specific combination. For example, if we require an SNR of 100 in the dark regions and ‘N’ is the total photo electron count in some exposure time ‘ t_e ’, then,

$$\begin{aligned} \frac{N}{\sqrt{N}} &= 100 \\ \Rightarrow \sqrt{N} &= 100 \\ \Rightarrow N &= 10^4 \\ \Rightarrow \text{photoelctron per second in dark feauturs} \times t_e &= 10^4 \\ \Rightarrow t_e &= \frac{10^4}{\text{photoelctron per second in dark}} \end{aligned}$$

However, this does not take into account the amount of out-of-band leakage, which is going to contribute to the SNR being the dominant component in the noise. If we incorporate that into the calculation, we can increase the amount of exposure time required to reach the highest possible SNR as long as we do not exceed the maximum exposure time 1.4 seconds. So now,

$$\begin{aligned} \frac{N}{\sqrt{N} + \text{Leakage in dark}} &= \text{SNR}_{\max} \\ \Rightarrow \frac{\text{photoelctron per second in dark} \times t_e}{\sqrt{\text{photoelctron per second in dark} \times t_e} + \text{leak per second in dark} \times t_e} &= \text{SNR}_{\max} \\ \Rightarrow \frac{\text{photoelctron per second in dark} \times \sqrt{t_e}}{\sqrt{\text{photoelctron per second in dark} + \text{leak per second in dark}} \times \sqrt{t_e}} &= \text{SNR}_{\max} \\ \Rightarrow t_e &= \frac{\text{SNR}_{\max}^2 \times \text{photoelctron per second in dark}}{(\text{photoelctron per second in dark} - \text{SNR}_{\max} \times \text{leak per second in dark})^2} \end{aligned} \tag{5.3}$$

In the limit,

$$\text{leak per second in dark} \rightarrow 0$$

this expression reduces to $t_e = \frac{\text{SNR}_{\max}^2}{\text{photoelctron per second in dark}}$. With this definition of exposure time we calculate the SNR for all the filter combination.

5.4.2 Filter Choice for BB2

This section details the selection process for the BB2 filters, which was also applied to the other passbands. Figure ?? presents the cosmetics spreadsheet provided by the vendor. The defects in the coating were characterized based on their nature and size, such as digs, pinholes, and scratches. In Figure ??, several pinholes are marked with red circles for BB2 filter serials #1, 2, and 5. Filters #3 and 4 are in better condition in terms of the cosmetics of the coating.

The table ?? shows the SNR at the dark features on sun, calculated using a sample spectra and measured response for BB2 filters. Based on the cosmetic quality rest of the BB2 filters #3 and 4 were already more preferred. Similarly in this case also they show a better SNR compared to the rest of the filters. A similar cosmetic quality inspection was done for BP3 filters. After combining all these information, finally BB2 #3 was chosen to be mounted on the spacecraft. Similar analysis was done for all possible combinations of the science filters to finally choose the ones to be mounted.

BP4 Filter choice	BB2 #1	BB2 #2	BB2 #3	BB2 #4	BB2 #5
#4	48	66	68	67	66
#2	47	64	66	66	64
#3	48	65	67	67	65

Table 5.2:: SNR for various choices of BB2 filters

5.5 Stellar Calibration of *SUIT*

To address these scientific objectives as outlined in §??, the necessity of absolute stellar calibration is manifold. *SUIT*, with its capabilities, images the Sun and dynamic processes such as solar flares and jets occurring in the solar atmosphere, including eruptions of various scales. Additionally, these images assist us in measuring solar spectral irradiance across 11 different passbands in the NUV. With absolute calibration, we would be able to probe the underlying physical mechanisms driving these processes and can derive the spectral energy distribution in absolute units.

Many properties of white-light flares are also observable in the near-ultraviolet (NUV) regime. Typically, there are significant correlations between different flare quantities in white light and X-ray emissions, such as white-light excess and soft X-ray flux (??). These correlations enable us to infer underlying mechanisms that likely drive the correlation between these quantities, such as the mechanisms responsible for transferring energy and mass across different layers of the Sun. In our case, *SUIT* would observe the Sun alongside HEL1OS and SoLEXS (?). For comparative purposes across observations from three different instruments, absolute calibration becomes essential.

Furthermore, in conjunction with *SUIT*, the HEL1OS and SoLEXS data provide broad coverage of the electromagnetic spectrum from hard X-rays to the NUV. This comprehensive coverage allows us not only to study the initiation and triggering of eruptive events but also

CHAPTER 5. SUIT PREPARATORY ANALYSIS

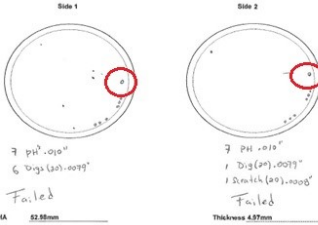
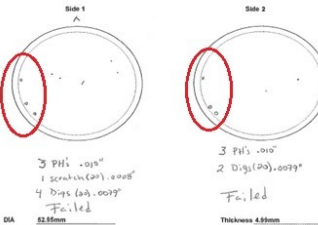
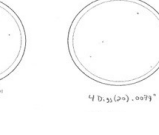
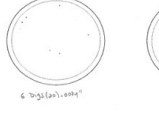
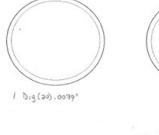
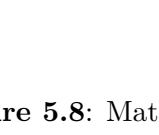
MATERION		MATERION	
Materion Precision Optics and Thin Film Coating Inc. Customer: IJCAA SN: 1 Part #: F-WB-0016021 S/D Spec. 40/20 MIL-C-48497A BB2 (27746nm) 53 μm Lot#: 170328 Inspected by [REDACTED] WOF: 170328/1 Date: 3/26/2020		Materion Precision Optics and Thin Film Coating Inc. Customer: IJCAA SN: 2 Part #: F-WB-0016021 S/D Spec. 40/20 MIL-C-48497A BB2 (27746nm) 53 mm Lot#: 170328 Inspected by [REDACTED] WOF: 170328/1 Date: 3/26/2020	
 <p>Side 1</p> <p>Thickness: 4.57mm</p> <p>Thickness: 4.57mm</p> <p>DIA: 62.50mm CA: 49mm</p> <p>Defects: 1 PH .010", 6 Digs (2x), .0079", Fail</p>		 <p>Side 1</p> <p>Thickness: 4.55mm</p> <p>Thickness: 4.55mm</p> <p>DIA: 62.50mm CA: 49mm</p> <p>Defects: 3 PH .010", 1 Scratches (2x), .0088", 4 Digs (2x), .0079", Fail</p>	
 <p>Side 2</p> <p>Thickness: 4.57mm</p> <p>Thickness: 4.57mm</p> <p>DIA: 62.50mm CA: 49mm</p> <p>Defects: 6 Digs (2x), .0079", Fail</p>		 <p>Side 2</p> <p>Thickness: 4.55mm</p> <p>Thickness: 4.55mm</p> <p>DIA: 62.50mm CA: 49mm</p> <p>Defects: 4 PH .010", 2 Digs (2x), .0079", Fail</p>	
OPTIC INSPECTION			
MATERION		MATERION	
Materion Precision Optics and Thin Film Coating Inc. Customer: IJCAA SN: 3 Part #: F-WB-0016021 S/D Spec. 40/20 MIL-C-48497A BB2 (27746nm) 53 μm Lot#: 170328 Inspected by [REDACTED] WOF: 170328/1 Date: 3/26/2020		Materion Precision Optics and Thin Film Coating Inc. Customer: IJCAA SN: 4 Part #: F-WB-0016021 S/D Spec. 40/20 MIL-C-48497A BB2 (27746nm) 53 μm Lot#: 170328 Inspected by [REDACTED] WOF: 170328/1 Date: 3/26/2020	
 <p>Side 1</p> <p>Thickness: 4.56mm</p> <p>Thickness: 4.56mm</p> <p>DIA: 62.50mm CA: 49mm</p> <p>Defects: 6 Digs (2x), .0079"</p>		 <p>Side 2</p> <p>Thickness: 4.56mm</p> <p>Thickness: 4.56mm</p> <p>DIA: 62.50mm CA: 49mm</p> <p>Defects: 4 Digs (2x), .0079"</p>	
 <p>Side 1</p> <p>Thickness: 4.55mm</p> <p>Thickness: 4.55mm</p> <p>DIA: 62.50mm CA: 49mm</p> <p>Defects: 4 PH .010", 6 Digs (2x), .0079", Fail</p>		 <p>Side 2</p> <p>Thickness: 4.55mm</p> <p>Thickness: 4.55mm</p> <p>DIA: 62.50mm CA: 49mm</p> <p>Defects: 4 PH .010", 2 Digs (2x), .0079", Fail</p>	
OPTIC INSPECTION			
MATERION		MATERION	
Materion Precision Optics and Thin Film Coating Inc. Customer: IJCAA SN: 5 Part #: F-WB-0016021 S/D Spec. 40/20 MIL-C-48497A BB2 (27746nm) 53 μm Lot#: 170328 Inspected by [REDACTED] WOF: 170328/1 Date: 3/26/2020		Materion Precision Optics and Thin Film Coating Inc. Customer: IJCAA SN: 6 Part #: F-WB-0016021 S/D Spec. 40/20 MIL-C-48497A BB2 (27746nm) 53 μm Lot#: 170328 Inspected by [REDACTED] WOF: 170328/1 Date: 3/26/2020	
 <p>Side 1</p> <p>Thickness: 4.55mm</p> <p>Thickness: 4.55mm</p> <p>DIA: 62.50mm CA: 49mm</p> <p>Defects: 4 PH .010", 6 Digs (2x), .0079", Fail</p>		 <p>Side 2</p> <p>Thickness: 4.55mm</p> <p>Thickness: 4.55mm</p> <p>DIA: 62.50mm CA: 49mm</p> <p>Defects: 4 PH .010", 2 Digs (2x), .0079", Fail</p>	
OPTIC INSPECTION			

Figure 5.8: Materion provided cosmetics report for various option of BB2 filters.

CHAPTER 5. SUIT PREPARATORY ANALYSIS

to examine these quantities over a solar cycle and assess their contribution to changes in the solar spectral irradiance. Lastly, it's important to note that the Earth's atmosphere absorbs UV and X-ray emissions. UV radiation below 310 nm is largely absorbed by the atmosphere, while radiation beyond 310 nm can penetrate it. The absorption dynamics are primarily governed by oxygen (O_2) below 200 nm and ozone (O_3) beyond 240 nm, with both substances actively participating in the absorption process between 200 and 240 nm (?). Therefore, understanding the solar spectral irradiance in the 200-400 nm range is pivotal for comprehending the dynamics and chemistry of Earth's atmosphere, particularly the ozone-oxygen cycle. This data is a crucial input for atmospheric modelling and provides insights into the Sun-Earth atmosphere connection. With absolute stellar calibration, *SUIT* would furnish us with the solar irradiance in these bands and the radiance of various features on the solar disk before it encounters atmospheric attenuation.

SUIT is equipped with 16 calibration LEDs, 8 each emitting at peak wavelengths 258nm and 356nm, respectively. However, it's worth noting that LEDs may degrade over time and do not offer fluxes corresponding to each individual filter. We have obtained measurements of the flux-to-count ratio at various wavelengths within the extent of the science filter bands. This data will undoubtedly assist us in providing absolute calibration to *SUIT* observations. Nevertheless, while we can quantify how the overall throughput of the science filter combinations changes over time, we cannot quantify how the effective area of the science filter combination degrades as a function of wavelength. This degradation would impact the radiometric calibration using these measurements over time. Therefore, calibration through alternative methods is necessary, such as utilizing standard astronomical sources.

In an ideal scenario, the captured image would remain unaltered, devoid of any artefacts introduced by the instrument. However, in practice, the obtained image is influenced by the instrument response, which can degrade over time. Radiometric calibration involves quantifying the instrumental response and using it to predict the actual signal received from the source.

Furthermore, *SUIT* lacks in-band spectral resolution and lacks an accurate on-board calibration lamp corresponding to the wavelength coverage of each individual filter. Therefore, it becomes imperative to convert the total in-band photo-electron count to the corresponding energy in real units. This necessity arises because photons across a wide band possess varying energy levels, making it challenging, if not impossible, to ascertain the distribution of photo-electrons across a wavelength band.

In principle, for any astronomical source, we encounter,

$$DN(\lambda) = R(\lambda) \times F(\lambda)$$

where $F(\lambda)$, $DN(\lambda)$ and $R(\lambda)$ are the emitted **photon** flux, measured signal and the response of the system at the wavelength λ , respectively. Here, $R(\lambda)$ (instrument response)

will consist of the response from all the components of the telescope, namely the thermal filter, the primary and secondary mirrors, the science filter in conjunction with the bandpass filer, the focusing lens, the QE and the electronics efficiency of the detector (a CCD in this case). In the case of a standard source, we can write,

$$\begin{aligned} \text{DN}(\lambda)_{\text{calib}} &= R(\lambda)_{\text{calib}} \times F(\lambda)_{\text{calib}} \\ \implies R(\lambda)_{\text{calib}} &= \frac{\text{DN}(\lambda)_{\text{calib}}}{F(\lambda)_{\text{calib}}} \end{aligned}$$

where the subscript ‘calib’ denotes all variables related to the standard absolute calibration source. The parameter $R(\lambda)_{\text{calib}}$ represents a calibration factor acquired by observing a standard source using an instrument. Photon flux **from a source** can be straightforwardly computed from an absolutely calibrated spectrum $S(\lambda)$ **using the formula** $F(\lambda) = S(\lambda) \times \frac{\lambda}{hc}$.

Similarly, for the target source under observation, we have,

$$\begin{aligned} \text{DN}(\lambda)_{\text{target}} &= R(\lambda)_{\text{target}} \times F(\lambda)_{\text{target}} \\ \implies F(\lambda)_{\text{target}} &= \frac{\text{DN}(\lambda)_{\text{target}}}{R(\lambda)_{\text{calib}}} \end{aligned} \tag{5.4}$$

where, it is assumed that the instrumental response remains unchanged from the calibrated source to the target source being observed, and hence $R(\lambda)_{\text{target}} = R(\lambda)_{\text{calib}}$.

5.5.1 Requirements of the calibration source

In general, for radiometric calibration, on-board standard sources such as diodes, LEDs, etc., or astronomical sources like standard stars are employed. However, in a space-based mission, the on-board artificial sources themselves undergo significant degradation, which needs to be meticulously modeled. Therefore, it is preferable to utilize standard stars as calibration sources, provided they satisfy the essential conditions listed below (?).

- The calibration source must exhibit adequate brightness within the wavelength region of interest, which spans from 200 to 400 nm in the current context, to achieve the requisite photometric accuracy across all science filters. In our case, the thermal filter at the entrance aperture significantly attenuates in-band solar flux (along with nearly all out-band flux) reaching the detector to prevent pixel saturation. This mechanism applies equally to the calibration sources. Hence, the calibration source must possess sufficient brightness to attain an acceptable signal-to-noise ratio (SNR) within a reasonable observation time.

- Ideally, the standard calibration source should exhibit minimal variability, with any changes occurring over timescales significantly longer than the time required to accumulate a sufficient number of photons from the source to achieve the desired level of photometric accuracy.
- Preferably, the calibration source should not be integrated into a complex system. However, if it is, any accompanying components should be sufficiently weak so that the photon flux from them does not significantly contribute to the total flux of the system. Otherwise, it would be necessary to model the contribution of the companion(s) separately.

Any astronomical source that meets these criteria and has its spectral energy distribution (SED) studied and calibrated to absolute units would be suitable for radiometric calibration. Stars such as Sirius A (HD48915/HR2491) and Vega (HR7001) largely fulfill the aforementioned criteria, with the exception of Sirius A, which has a white dwarf companion known as Sirius B. However, the apparent magnitudes of Sirius A and Sirius B are -1.46 (?) and 8.44 (??) respectively, ensuring that the contribution from Sirius B is mostly negligible. The absolute calibrated spectra for both stars are depicted in Fig. ?? and are sourced from the CALSPEC archive, which contains composite stellar spectra used as flux standards in the Hubble Space Telescope (HST) system.

5.5.2 Exposure time for the calibration sources

A high level of photometric accuracy is essential for imaging the Sun and monitoring spectral irradiance. It's noteworthy that the total energy output from the Sun at wavelengths below 400 nm comprises only about 8% of the total solar irradiance (TSI). However, there is a recorded variability of over 60% in radiation below 400 nm over a solar cycle (?), whereas the variability in TSI over a solar cycle is approximately 0.1%. Photometric accuracy is defined as the ratio of the Poisson noise of the signal to the signal itself. The number of photo-electrons produced in a given exposure time is given by Eqn. ??,?. We aim for a photometric accuracy of 0.2%, which corresponds to a photo-electron count of $\sim 2.5 \times 10^5$. Considering this requirement, we compute the exposure times required for both Vega and Sirius A, which are given in Table ??.

5.5.3 Method for Calibration

With the exposure times calculated for all filters, for calibration purposes, we will assume a photometric accuracy of 0.2% across all bands for the calibration source. This implies that the Poisson noise arising from the total photo electron count is 0.2%, corresponding to a total photo electron count of approximately 2.5×10^5 . As described in Section ??, the flux from the target source is given by $F(\lambda)_{\text{target}} = \frac{S(\lambda)_{\text{target}}}{R(\lambda)_{\text{calib}}}$, where we assume that

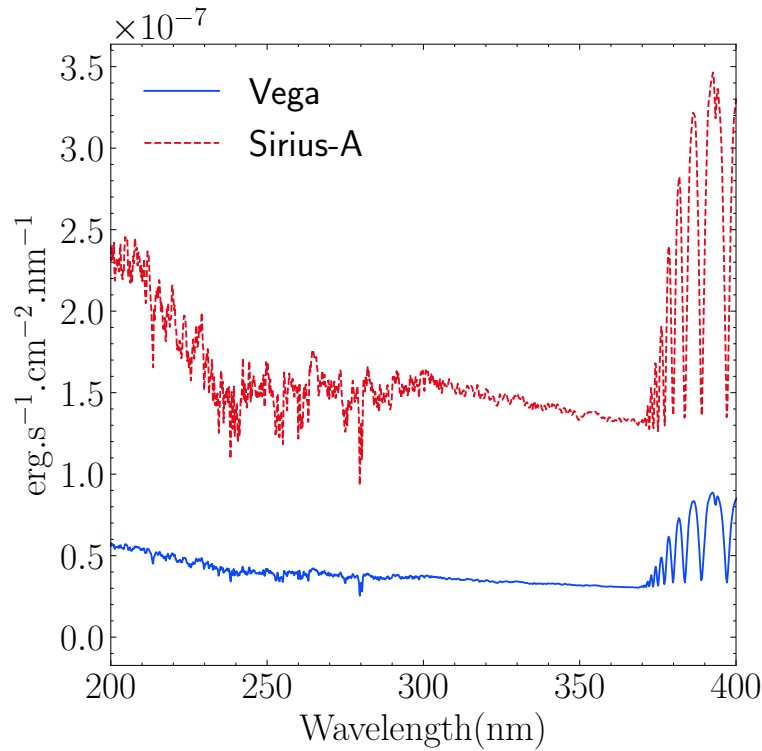


Figure 5.9: Calibrated spectra of Vega and Sirius A taken from [CALSPEC](#), Vega in Blue and Sirius A in Orange.

Band	Exposure time(minutes)	
	Vega	Sirius A
NB1	8	2
NB2	23	6
NB3	23	6
NB4	19	5
NB5	16.5	4
NB6	15	3.5
NB7	12	3
NB8	368	90
BB1	2	0.5
BB2	20	5
BB3	13	3

Table 5.3:: The exposure time required to obtain 2.5×10^5 photo-electrons to achieve 0.2% photometric accuracy in each of the science filters for both Vega and Sirius A.

CHAPTER 5. SUIT PREPARATORY ANALYSIS

the instrumental response $R(\lambda)_{\text{calib}}$ remains unchanged from the calibration source to the target source. Therefore, given a calibration source using the absolute spectra ($F(\lambda)_{\text{calib}}$) and the signal ($S(\lambda)_{\text{calib}}$) received from it, we can quantify the telescope responses at various bandpasses ($R(\lambda)_{\text{calib}}$).

In the case of *SUIT*, though there is no spectral resolution within the bands, and the only information we will obtain from an observation is the total number of photo electron counts from the bands for a given exposure time. The general method is as follows:

- Given the spectra of a calibration source one can create the photo electron count profiles using the instrument filter profiles.
- One can calculate the total number of photo electrons generated for some exposure time as:

$$DN_{\text{calib}} = \int P(\lambda)_{\text{calib}} R(\lambda) A t d\lambda$$

where, $P(\lambda)$ is the photon flux from the Calibration source.

- The inband energy from the spectra of the calibration source for the same exposure time can be calculated. The FWHM is taken to be the extent of each band while calculating the total energy.

$$T_{\text{calib}} = \int_{\text{inband}} F(\lambda)_{\text{calib}} A t d\lambda$$

- The ratio of these two quantities give the calibration constant, ‘C’ for each band, $C = \frac{T_{\text{calib}}}{DN_{\text{calib}}}$

To estimate how well this method performs, we use Vega (Sirius A) as the calibration source and produce the phtoelctron count profiles from Sirius A (Vega) and the Sun. The total count arising from each band multiplied by the calibration constant(C) should give the total energy from the spectra.

5.5.4 Sirius A as calibration source

Table ?? shows the performance of the method for a Sirius A as the calibrating source and sun as a target with 200s exposure in all bands. The uncertainties in the table ?? are obtained by propagating the uncertainties of the [CALSPEC](#) spectra. Key thing to note here, the comparisons for solar spectra are made with a sun as a star spectra, while *SUIT* is going to observe the full solar disk on $(4k \times 4k)$ CCD. We have to add the contribution from all the pixels to have the full disk contribution. In practice, in the stellar pointing calibration run *SUIT* will be re-pointed towards Sirius A and the measurements would be used for absolute calibration.

CHAPTER 5. SUIT PREPARATORY ANALYSIS

Band	$(C = \frac{T_{sir}}{DN_{sir}}) \times 10^{15}$ (J/DN)	DN/10 ¹³	Predicted Energy ($C \times DN$)	Energy from spectra(J)
NB1	(72.62 ± 0.88)	$(9.47 \pm 9.7 \times 10^{-7})$	(6.881 ± 0.083)	6.839
NB2	(5.164 ± 0.062)	$(20.6 \pm 1.4 \times 10^{-6})$	(1.065 ± 0.013)	1.072
NB3	(3.627 ± 0.044)	$(10.5 \pm 1.0 \times 10^{-6})$	$(3.854 \pm 0.043) \times 10^{-1}$	3.884×10^{-1}
NB4	(3.253 ± 0.039)	$(12.3 \pm 1.1 \times 10^{-6})$	$(4.003 \pm 0.048) \times 10^{-1}$	(4.001×10^{-1})
NB5	(3.160 ± 0.038)	$(40.6 \pm 2.0 \times 10^{-6})$	(1.284 ± 0.016)	1.307
NB6	(7.295 ± 0.088)	$(65.7 \pm 2.6 \times 10^{-6})$	(4.797 ± 0.058)	4.836
NB7	(8.715 ± 0.010)	$(123 \pm 4 \times 10^{-6})$	$(1.073 \pm 0.013) \times 10^1$	1.055×10^1
NB8	(17.71 ± 0.21)	$(5.01 \pm 7.1 \times 10^{-7})$	$(8.88 \pm 0.11) \times 10^{-1}$	8.93×10^{-1}
BB1	(28.50 ± 0.41)	$(46.0 \pm 2.1 \times 10^{-6})$	(13.114 ± 0.188)	13.113
BB2	(469.9 ± 5.7)	$(28.3 \pm 1.7 \times 10^{-6})$	(132.997 ± 1.607)	132.994
BB3	(221.1 ± 2.7)	$(176 \pm 4 \times 10^{-6})$	$(3.903 \pm 0.047) \times 10^2$	3.896×10^2

Table 5.4:: The performance of the method with Sirius A as calibrating source and sun as a target with 200s exposure in all bands.

5.6 Summary and Discussion

SUIT is our first full-disk eye on the Sun in Mg II window and Ca II h line and the various continuum channels onboard. The narrow band continuum and line channels provide us with a targeted view into various layers of the solar atmosphere, while the three broadband channels are designed to probe the radiance from the Sun to investigate the effect of NUV radiation on Earth’s atmosphere over the duration of a solar cycle. This chapter focused on the various initial preparatory analysis we carried out in anticipation of *SUIT*, and some of the calibration scheme planning initially carried on.

The initial jitter estimation was done from simulations provided by the ISRO URSC team. That exhibited the jitter to be minimal compared to *SUIT* exposure timescales, hence would have no noticeable effects on the imaging. Properly estimating the spacecraft jitter in orbit would be possible once the stellar calibration is done. During the stellar calibration, the long exposure of Sirius-A, , *i.e.* a point source, would be carried out in a series of short exposures. This would give us the opportunity to quantify the amount of jitter in the spacecraft.

The initial throughput model of *SUIT* was designed out of the necessity of a robust throughput model to estimate the expected SNR of various vendor-provided science filters, according to the scientific cases. It proved useful in finalizing the choice of the science filters to be mounted on the payload. The throughput model also proved useful in designing our stellar calibration scheme and provided a useful benchmark for validating the photometric performance of the payload on the ground. The spectral validation of the science filters is important primarily for verifying the science filter combinations are observing the necessary wavelength windows. The necessity of an accurate throughput model, spectral and photometric validation of the payload, and stellar calibration of the payload are intertwined with

CHAPTER 5. SUIT PREPARATORY ANALYSIS

one another. A full characterization of all of these quantities is only possible after stellar calibration is carried out.

CHAPTER 5. SUIT PREPARATORY ANALYSIS

Chapter 6

Effects of Solar flares on the local plasma environment from Mg II observations

This thesis chapter originally appeared in the literature as
The Evolution of the Ratio of Mg II Intensities During Solar Flares,
Roy, S., & Tripathi, D. 2024, ApJ, 964, 106, doi:[10.3847/1538-4357/ad2a46](https://doi.org/10.3847/1538-4357/ad2a46).

6.1 Introduction

Solar flares are the most energetic events on the Sun, where an enormous amount of magnetic free energy is released due to the reconfiguration of the coronal magnetic field. The released energy can cause particle acceleration, heating and flows in the solar atmosphere and a transient enhancement in solar radiative output. Notably, a significant portion of the radiated energy during flares originates from the dense chromosphere (??). Therefore, examining chromospheric lines during flares offers valuable diagnostic tools for understanding the physics of solar flares and their impact on the local plasma environment.

The chromosphere emits radiation across various ultraviolet (UV) and optical lines. While many optical lines, such as H α and Ca II, are routinely observed from ground-based telescopes, observations of the Mg II resonance lines have been relatively infrequent in the past. However, since the launch of the Interface Region Imaging Spectrograph (IRIS) (?), regular monitoring of these lines with excellent spatial and spectral resolution has become possible.

The Mg II k and h lines represent transitions to the ground state from finely split upper levels ($3p\ ^2P_{3/2}$ – $3s\ ^2S_{1/2}$ and $3p^2P_{1/2}$ – $3s^2S_{1/2}$), resulting in optically thick lines at wavelengths 2796.34 Å (Mg II k) and 2803.52Å (Mg II h). It has been suggested that the intensity

ratios of these lines can offer insights into the optical depth of the local environment (?).

The integrated intensity of a line transitioning from an upper level j to a lower level i depends on the collision strength Ω_{ij} for that transition, given by (??),

$$\Omega_{ij} = \frac{8\pi}{\sqrt{3}} \frac{I_H}{\Delta\epsilon_{ij}} g\omega_i f_{ij} \quad (6.1)$$

Here, I_H denotes the ionization energy of hydrogen, $\Delta\epsilon_{ij}$ represents the threshold energy for the transition, g is the Gaunt factor, ω_i is the statistical weight of the level, and f_{ij} stands for the oscillator strength. In optically thin conditions, the intensity ratio of the k to h line equals the ratio of collision strengths, as the escape probability of photons is unity. As the Mg II k and h lines share the same ionization state and originate from a transition to a shared lower level, and given that the statistical weight (ω_i) is the same in both cases, the line intensity ratio is simply the ratio of oscillator strengths (f_{ij}). Consequently, this ratio is expected to be 2:1 in optically thin conditions (??). **For further details on the ratio of the oscillator strengths please refer to §??.**

Under optically thick conditions the radiation is absorbed and re-emitted more effectively by the medium. As a result the radiation field in the medium becomes "thermalized", meaning the population of the energy levels are dictated by the Boltzmann distribution, rather than the specific radiative process or the specific line strengths. As a result the intensity of the lines are no longer individually dependent on their Einstein coefficients or the detailed radiative processes but are instead controlled by the overall temperature and the combined behavior of the radiation field in an optically thick medium. This leads to a situation where both the upper levels for the Mg II k and h lines are very similar, as they are formed at relatively similar heights. So the intensity ratio is closer to 1:1 (??). This ratio has been used before to comment on the opacity of the local plasma environment. It has been demonstrated from previous solar observations, that the Mg II lines exhibit no central reversal $\sim 6''$ above the limb, and $\sim 12''$ above the limb the line intensity ratio is 2:1, implying that the lines become optically thin (??). On the contrary, ? showed from sunspot spectra, although the Mg II lines show no central reversal, the ratio was still lower 2:1, implying optically thick conditions.

Moreover, the Mg II k and h lines can serve to estimate velocity in the middle and upper chromosphere, chromospheric velocity gradients, and temperature in the middle chromosphere (???). Emission from the Mg II triplets can help identify heating in the lower chromosphere (?). Various studies have demonstrated spatial variations in Mg II line profiles (??). For instance, ? associated the leading edge of flare ribbons with enhanced broadening and strong central reversal, interpreting this difference in profile as indicative of distinct heating mechanisms at different locations within flare ribbons. Similarly, ?? revealed differences in line profiles and energy input.

Using observations recorded by the OSO-8 LPSP instrument, (?) investigated the evolution of intensity ratios of Mg II h & k, Ca II h & k, and Ly α & β lines. They observed that the intensity ratio of the Ca II k/h lines increased from 1 to 1.2 during the ascending phase of a flare and returned to 1 during later phases. This correlated temporal behavior across various elements was interpreted as an indication of downward energy propagation, suggesting a potential decrease in opacity due to localized heating at the formation height of the Ca II line during the flare's rise phase.

Here, we investigate the evolution of intensity ratios of the Mg II h & k lines during three flares: C-class, M-class, and X-class. Specifically, we focus on the dependence of line ratios on the underlying magnetic field strength, a relationship that, to our knowledge, has not been explored previously. The remainder of this chapter is organized as follows. Section ?? presents the observations utilized in this study, followed by our data reduction and analysis methods, and the results in Section ??.

6.2 Observations

Event Date	Flare Peak (UT)	Flare Location (arcsec)	Raster Details	Raster Step (arcsec)	Raster Cadence (s)
Nov 4, 2015 (M-class)	13:52	[37",61"]	Coarse 16-step	2"	50
Oct 22, 2014 (X-class)	14:28	[-292",-302"]	Coarse 8-step	2"	131
Feb 3, 2015 (C-class)	22:55	[198",213"]	Dense 16-step	0.35"	33

Table 6.1:: List of flares studied in this chapter.

For this study, we selected three flares of M, X, and C classes, as listed in Table ?? by IRIS. IRIS is a NASA small explorer-class solar observation satellite that obtains UV spectra with high spatial (0.33–0.4" per pixel), temporal (1s), and spectral resolution (\sim 26 and \sim 53 mÅ). The primary lines regularly observed by IRIS include C II, Mg II, and Si IV. In the imaging channel, it typically observes in Mg II and Si IV. In our study, we utilized observations recorded in the Mg II h& k lines.

As mentioned earlier, this study aims to analyze the evolution of intensity ratios concerning magnetic flux density during the flares of various classes. To achieve this, we incorporated line-of-sight (LOS) magnetic field measurements from the Helioseismic and Magnetic Imager (HMI; ?) on the Solar Dynamics Observatory (SDO; ?). We utilized observations taken at 1600 Å by the Atmospheric Imaging Assembly (AIA; ?), also onboard SDO, to co-align the IRIS observations with those from AIA and subsequently HMI.

6.3 Data analysis and results

6.3.1 M3.7 Flare Observed on Nov 4, 2015

NOAA AR 12443 generated a multi-ribbon GOES class M3.7 flare on November 4, 2015, which commenced around 13:31 UT and peaked at approximately 13:52 UT, as observed from the GOES Soft X-ray (SXR) 1–8 Å flux (Fig.??a). This event occurred at approximately [37'',61''] heliographic position and was extensively observed by IRIS, AIA, and HMI. Fig.??a illustrates the GOES flux plot of the flare in the 0.5–4 Å range (blue) and the 1.0–8.0 Å range (red). Fig.?? b depicts AIA 1600Å image of the flaring region, showing two ribbons indicated by arrows. In panel (c), we present the line-of-sight (LOS) magnetic flux density map obtained from HMI, recorded nearly simultaneously with the AIA image shown in panel (b). The white (black) box overlaid on Fig.??(b) (c) represents the IRIS SJI (Slit-Jaw Imager) field of view (FOV). The white dot-dashed (magenta dashed) box in Fig.??b (c) indicates the IRIS raster FOV. The FOV of the SJI (approximately [120'' × 119'']) covers the central part of the flaring region, with a spectral sampling of approximately 0.05 Å/pixel. ? investigated the dynamics of the ribbons for this flare, while ? studied the associated radio bursts.

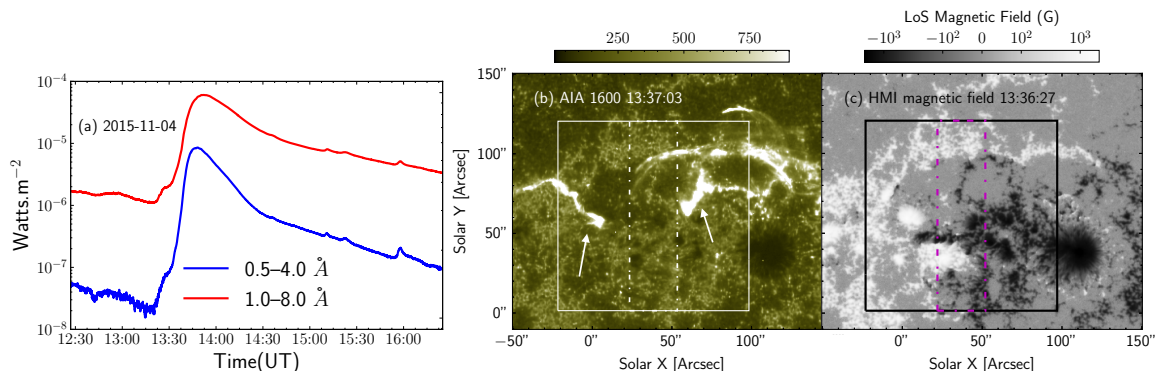


Figure 6.1: The M3.7 flare observed on November 4th, 2015. Panel a: GOES flux plot in 0.5–4 Å (blue) and 1.0–8.0 Å (red). Panel b: AIA 1600 Å image of the flaring region. Arrows locate the primary ribbons. Panel c: LOS magnetic flux density map obtained from HMI near the peak of the flare. The over-plotted white (black) boxes in panel b (c) represent the IRIS SJI FOV. The over-plotted white dot-dashed (magenta dashed) box in panel b (c) shows the IRIS raster FOV.

Figure ?? illustrates the evolution of the flare in AIA 304 Å. The flare is connected with a pre-existing filament that undergoes an eruption, splitting into two structures denoted as F1 & F2 in Fig.??(b) & (c). These two filament structures diverge from each other in opposite directions. The flare generates two primary flare ribbons, labeled as R1 & R2 in Fig.??(b), (c) & (d). Starting around 13:32 UT, R1 travels southeastward, crossing the IRIS raster FOV, indicated by the white dotted box in Fig.??(a), (b), (c) & (d). The IRIS

raster monitors the movement of the northern ribbon R1 and the eastern edge of R2. An animated version of Fig.?? is available in the online journal for further details.

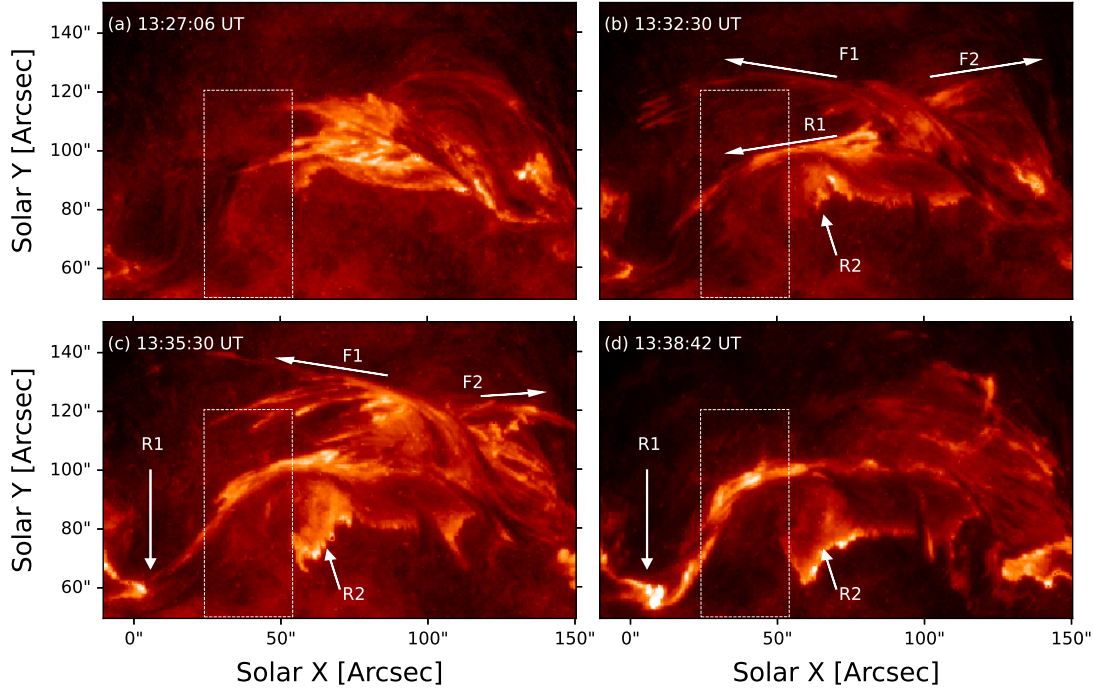


Figure 6.2: Sequence of AIA 304 Å images for the Nov 4th, 2015 flare. The white dotted box shows the portion of the IRIS raster FOV which scanned the ribbons. In panels b (c) F1 and F2 are the filament material, which move away from each other as the flare progresses. R1 and R2 in b (c,d) show the primary ribbons which move through the IRIS raster FOV. An animation of this image sequence is available in ?.

Fig.?? presents the same region as depicted in Fig.?? across the six coronal channels (i.e., 94, 131, 171, 193, 211, 335 Å) of SDO/AIA, recorded at the peak (top two rows) and during the decline phase (bottom two rows) of the flare. Post-eruption arcades (?) are clearly observable in all the channels, displaying slightly varied morphologies. These arcades contain evaporated thermal plasma and exhibit loop top brightening, likely due to colliding evaporation flows (see, e.g., ??).

We begin by aligning the HMI observations with the IRIS observations using the 1600 Å data recorded by AIA. Given that the observation involves an active region undergoing flaring, the magnetic field may also be rapidly changing (???). Therefore, we utilize a series of co-aligned full-disk maps from AIA and HMI to derive a rastered line-of-sight (LOS) map of magnetic flux density that precisely corresponds to the location and time of IRIS rasters. This procedure is outlined below.

Initially, we align the AIA 1600 Å observation with the HMI observation closest in time

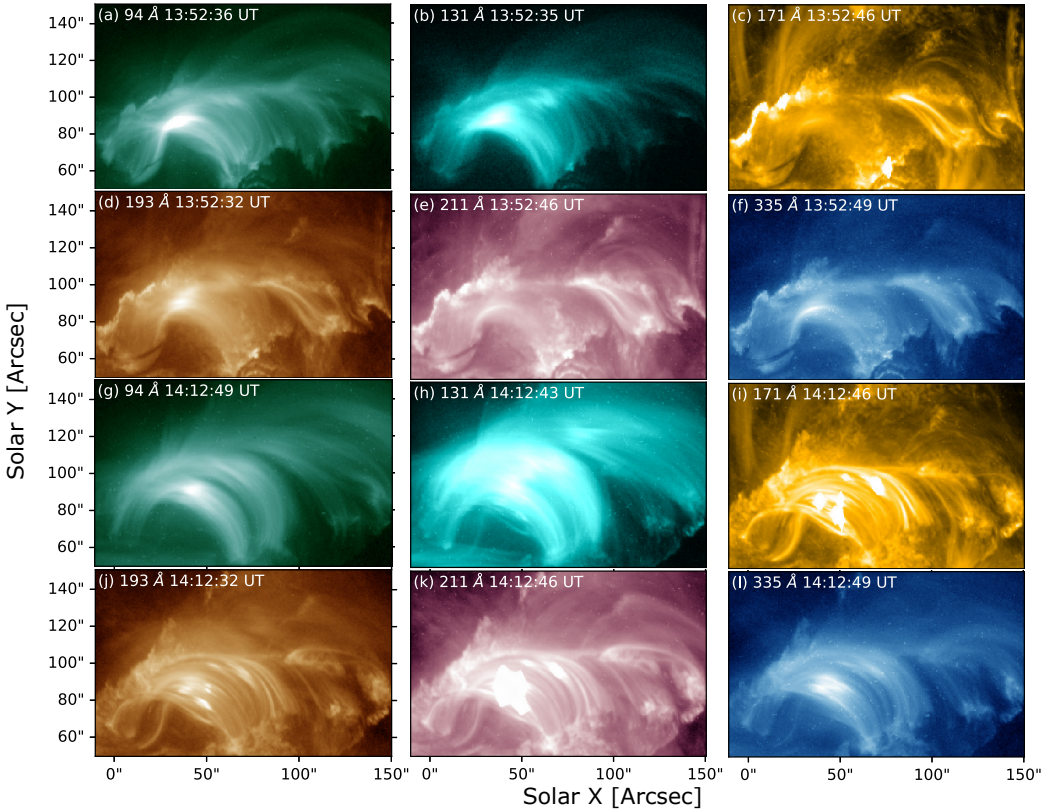


Figure 6.3: The Nov 4th, 2015 flare in the six Coronal channels of the SDO/AIA at the soft X-ray peak (panels (a)-(f)) and during the decline phase (panels (g)-(l)) of the flare.

to the IRIS SJI (Slit-Jaw Imager) and raster observations. Using the ‘aia_prep’ tool available in the *sswidl* distribution, we process the level 1 images to perform image registration and align AIA and HMI observations. Subsequently, we calculate the shift between AIA 1600 Å and the SJI 1400 Å. Using these calculated offsets, we co-align the magnetograms with the IRIS SJI 1400 Å observations, given that the AIA 1600 Å observation was already aligned with the HMI observations. We typically observe an offset of approximately $\sim 1.5''$ between HMI and IRIS. These co-aligned HMI maps are then utilized to derive the rastered magnetograms, which can be directly compared with IRIS raster observations.

For analyzing the properties of the Mg II lines, we fit a double Gaussian profile to both the k and h lines with a linear background symmetric about the line core. If excess emission is detected compared to the fitted background and line profile for wavelengths lower than 2792 Å and in-between 2798 Å to 2800 Å, we infer the presence of Mg II triplets in emission. A single Gaussian profile is fitted to the excess emission. It’s important to note that this approach may overlook the triplets unless the emission is sufficiently strong. However, this method serves our purpose since our primary objective is to characterize the Mg II k and h line profiles.

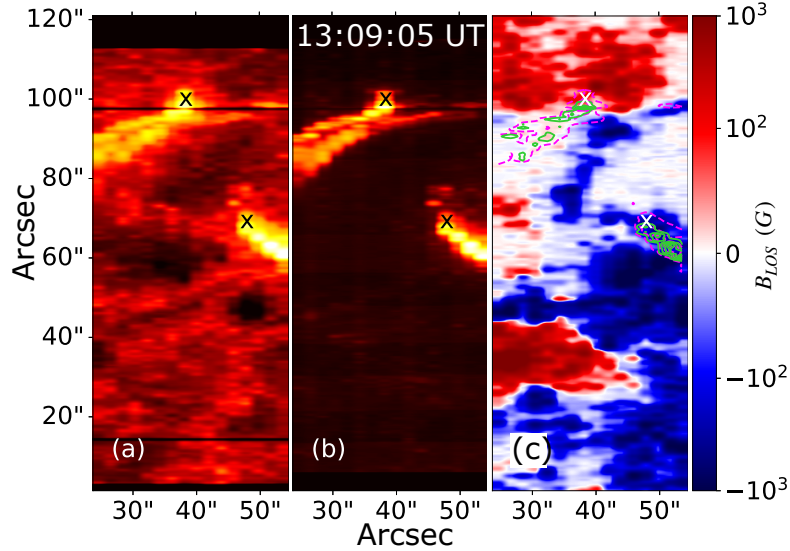


Figure 6.4: Obtained images in Mg II h (panel a) and k (panel b) and corresponding co-aligned and artificially rastered HMI LOS magnetic field map (panel c) for the M3.7 flare observed on November 4th, 2015. The magenta and lime green contours on panel c show the contours of Mg II h (panel a) and k (panel b) intensity.

Additionally, we exclude any pixels showing saturation in either of the lines. The uncertainty of the observed intensities is measured in DN (Data Numbers) using the method outlined in §2.1 of ? and subsequently applied in the fitting procedure. The uncertainties of the fitted Gaussian profiles are incorporated while integrating the profile to obtain the uncertainty of the line intensities.

In Figure ??, we present intensity maps obtained in Mg II h & k (panels a & b) alongside the rastered line-of-sight (LOS) magnetic field map in panel (c). The dashed magenta and solid green contours on the magnetic field maps represent the intensity from panels a and b, respectively. To investigate the Mg II k to h intensity line ratios over time, we selected two pixels one in the northern ribbon and another in the southern ribbon, as indicated by crosses. Fig. ?? displays the spectra overlaid with fits for the two pixels taken in the northern ribbon (top panel) and southern ribbon (bottom panel) obtained at different times.

We illustrate the Mg II k to h line intensity ratio derived from the two locations in the

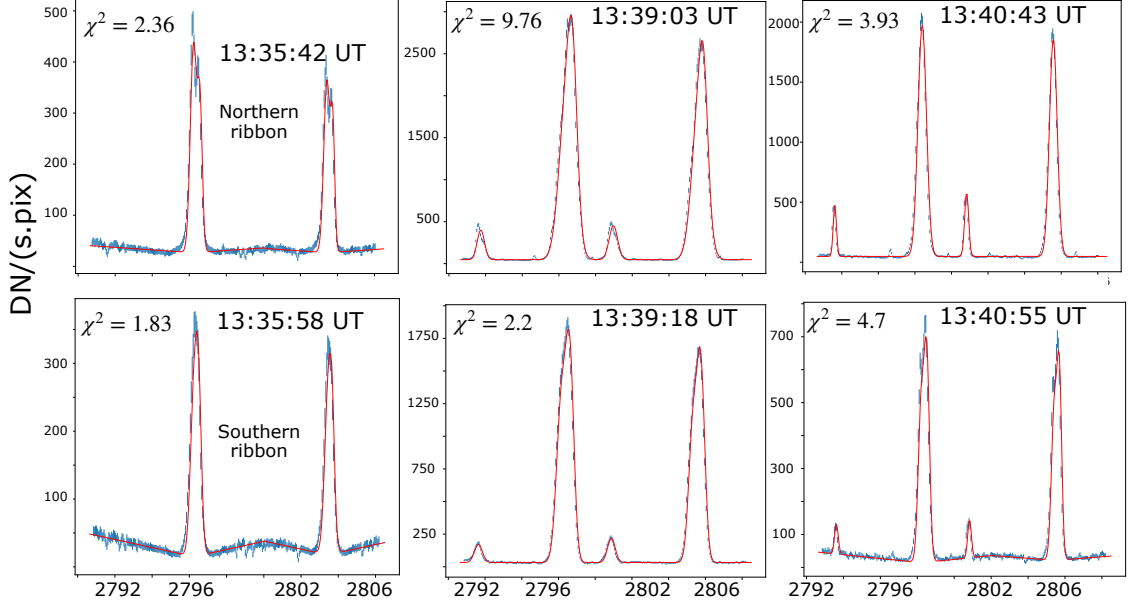


Figure 6.5: Fit of the Mg II window for the pixel marked in northern ribbon (southern ribbon) in Fig. ?? in top panel (bottom panel) from various times during the evolution of the flare.

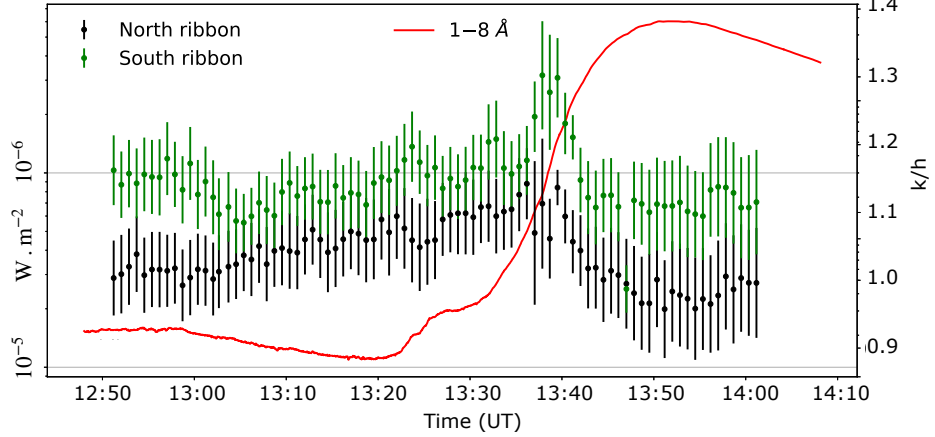


Figure 6.6: The 1–8 Å GOES light curve of the flare over-plotted with the time variation of Mg II k/h line intensity ratio for the northern (black) and southern (green) asterisks marked in panels a, b & c.

northern (black) and southern ribbons (green) in Fig. ???. Additionally, we overlay the GOES light curve of the flare obtained in 1.0–8.0Å (red solid line). Our observations indicate that the intensity ratios exhibit a slightly increasing trend, albeit within the margin of errors, during the early phase of the flare. The ratio demonstrates a distinct peak around the

midpoint of the impulsive phase, lasting for a very brief duration of approximately 150 seconds, before beginning to decrease. It's worth emphasizing that the pixel-by-pixel fitting of the Mg II h & k line profiles provided a sufficient signature of the time evolution of the k/h line intensity ratio during the flare.

6.3.2 Investigating the dependence on the local magnetic field in the Mg II lines

To explore the time evolution of the intensity ratio and its potential relationship with the photospheric magnetic field, we binned the spectra into various magnetic field bins from different flaring pixels. We selected the flaring pixels based on an intensity threshold relative to the peak intensity observed in IRIS rasters. A double Gaussian fit with a constant background was performed in a smaller wavelength window for both the Mg II h and k lines separately. This step was essentially carried out to mitigate the effects of the background and potential contributions from other spectral features.

Fig. ?? displays the Mg II k line profiles obtained at different times and averaged over different magnetic field bins. Each plot denotes the observation time and the magnetic field strength over which the spectra were averaged and fitted with a double Gaussian. Line intensities were computed by integrating the fitted Gaussian.

In Fig. ??, we present the k to h intensity ratios obtained in various bins of magnetic flux density at different times corresponding to different flare phases. The curve corresponding to 13:07:05 UT (red) represents the pre-flare phase, where the ratio is approximately 1.2. The ratio shows an increase during the impulsive phase, i.e., the curves corresponding to 13:23:44 UT (blue dotted) and 13:32:04 UT (green dashed). The ratio measured at 13:41:11 UT (magenta dashed), which is closest to the UV peak of the flare, exhibits the largest value across all magnetic field bins. Subsequently, during the decline phase, the ratio measured at 13:57:23 UT (black solid) falls below the values observed during the pre-flare phase. Additionally, it's noteworthy that there are no significant differences among the k to h ratios obtained in different bins of magnetic flux density at all times (including pre-flare, impulsive, peak, and decline phases) of the flare.

To explore further, we study the evolution of k to h intensity ratio as a function of time during the flare. In Fig. ??, we plot the time evolution of the k to h line intensity ratio averaged within the bins of different magnetic flux densities as a function of time. For better visibility the 20.9–184.4 G and 348.9–513.3 G points are offset by 30s and -30s, respectively. We also plot the GOES 1–8 Å light curve with the red solid line. These plots conspicuously reveal that the intensity ratios rise sharply during the impulsive phase, from ~ 1.20 to ~ 1.28 right before the soft X-ray flux peaks as seen from GOES, and decreases very rapidly thereafter, to lower than pre-flare values ~ 1.12 . The typical uncertainty value for the line intensity ratio is ~ 0.02 . We further note that the evolution of the Mg II k to h intensity ratio is remarkably similar across various strengths of magnetic flux densities.

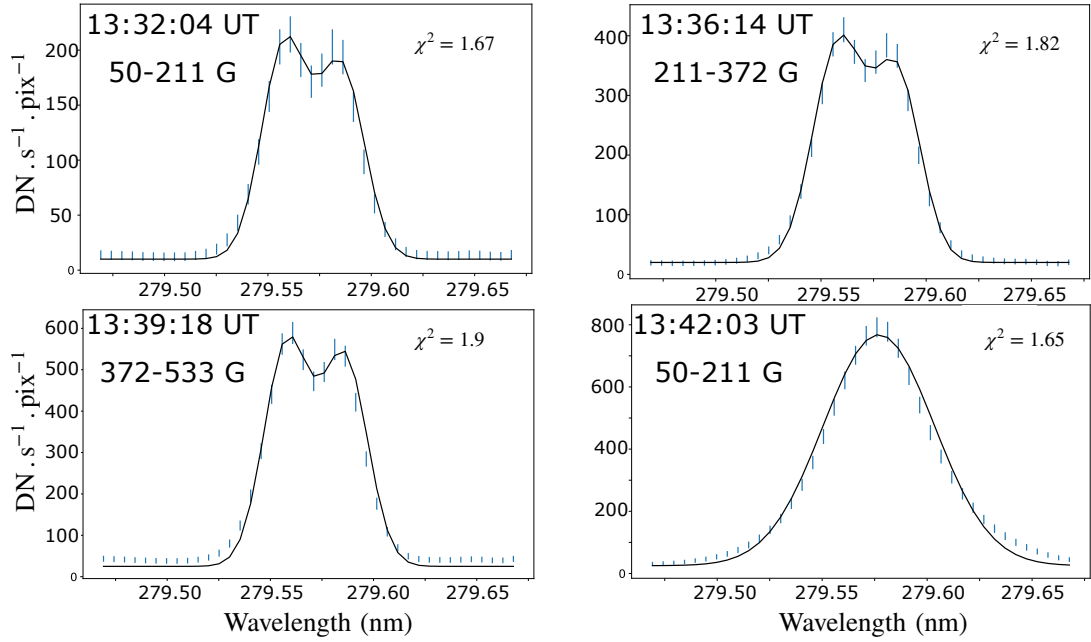


Figure 6.7: Fitted line profiles for the binned spectra for various magnetic field strengths from various times.

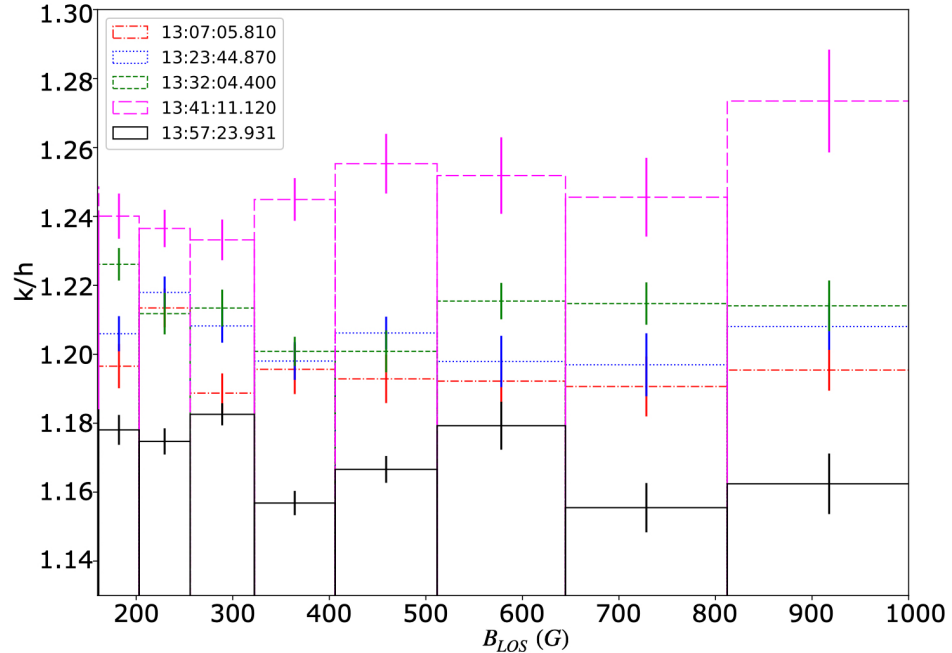


Figure 6.8: Mg II k to h line intensity ratio for various magnetic flux density bins at various time steps during the evolution of the flare.

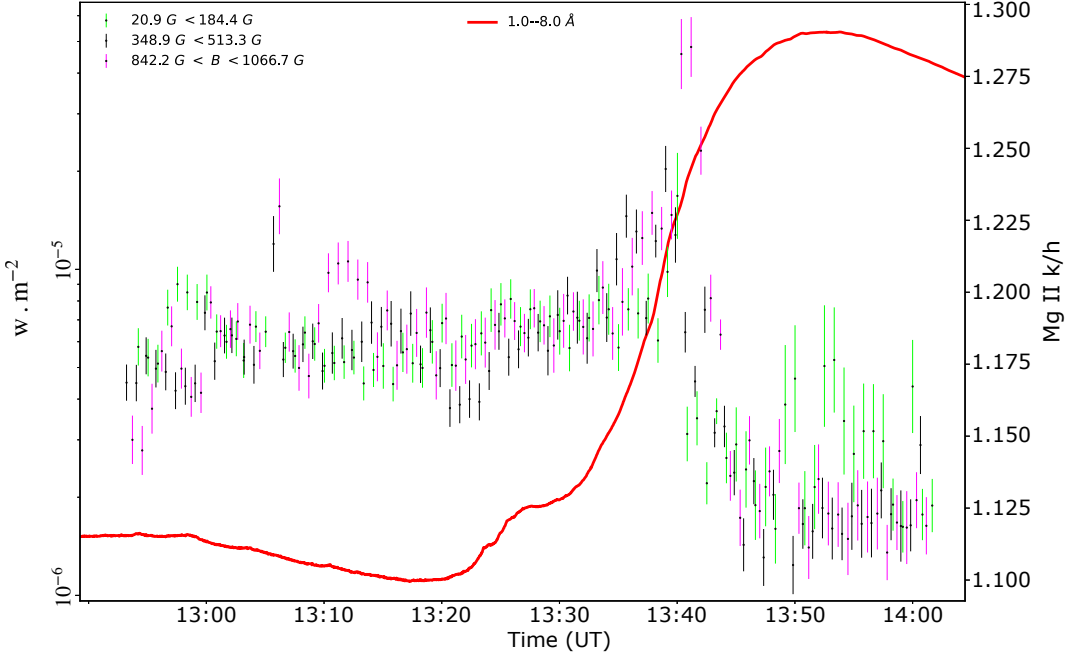


Figure 6.9: Time evolution of the Mg II k to h line intensity ratio obtained from averaged spectrum over the corresponding magnetic flux bin as labeled for the Nov 4, 2015 flare. For better visibility, the 20.9–184.4 G and 348.9–513.3 G points are offset by 30s and -30s respectively. Over-plotted red solid line displays the 1–8 Å GOES X-ray light curve.

6.3.3 X1.6 Flare Observed on Oct 22, 2014

An X 1.6 flare occurred on October 22, 2014, observed in AR 12192. The flare commenced at 14:02 UT and peaked at 14:28 UT as observed by GOES. Fig. ??(a) illustrates the GOES flux plot of the flare in the 0.5–4 Å range (blue) and the 1.0–8.0 Å range (red). Figs. ??(b) & (c) display an AIA 1600Å image and the line-of-sight (LOS) magnetic flux density map obtained from HMI, respectively. The overlaid boxes in panels (b) and (c) indicate the IRIS SJI (Slit-Jaw Imager) field of view (FOV). IRIS observed this flare with a large 8-step coarse raster covering a FOV of [14'', 174'']. It's worth noting that the IRIS SJI FOV and the slit direction were rotated by approximately 45° relative to the center of the HMI observation.

The flare manifests two ribbons in AIA 1600 Å, as indicated by the arrows. The eastern ribbon extends around a negative field region and is entirely covered by the IRIS SJI FOV. Conversely, the western ribbon extends around a positive field region, with only a portion of it covered by the IRIS SJI FOV, as depicted in panel (b). In Fig. ??, we present intensity maps obtained in Mg II h & k (panels a & b) alongside the rastered line-of-sight (LOS) magnetic field map (panel c). The black & green dashed contours in the LOS magnetic field map (panel c) indicate the intensity contours of Mg II h & k (panels a & b).

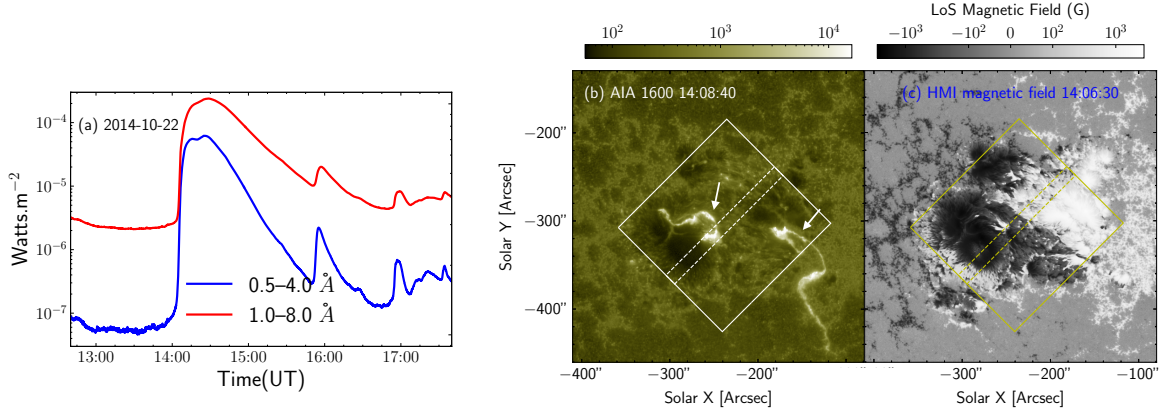


Figure 6.10: The X class flare observed on October 22, 2014. Panel a: GOES flux plot in 0.5–4 Å (blue) and 1.0–8.0 Å (red). Panel b: AIA 1600 Å image taken at the peak of the flare. Arrows locate the primary and secondary ribbons. Panel c: LOS magnetic flux density map obtained from HMI at the peak of the flare. The over-plotted white (black) box in panel b (c) represents the IRIS SJI FOV, and white dot-dashed (dashed) box in panels b (c) represents the IRIS Raster FOV.

Similar to the M-class flare studied in the previous section, we derive the Mg II k to h line intensity ratio for various bins of the magnetic flux density within the flaring region and study their time evolution. In Fig.?? right panel, we plot the intensity ratio in black and magenta colors for two different magnetic field bins. In the same panel, we also overlay the 1–8 Å GOES light curve (red solid line). We note that, unlike the M-class flare, we do not observe any noticeable change in the intensity ratio during the flare. There are approximately two to three data points showing an enhancement in the ratio, but these occur well before the onset of the flare.

6.3.4 C3.5 Flare Observed on Feb 03, 2015

On February 3, 2015, AR 12277 generated a C-class flare that peaked at 22:55 UT. Fig.?? depicts the GOES flux plot of the flare in the 0.5–4 Å range (blue) and the 1.0–8.0 Å range (red) in panel (a). Fig.??(b) & (c) displays an AIA 1600 Å image and the line-of-sight (LOS) magnetic flux density map obtained from HMI, respectively, recorded near the peak of the flare.

The overlaid white (black) box in panel (b) ((c)) indicates the IRIS SJI (Slit-Jaw Imager) field of view (FOV). The over-plotted white dot-dashed (magenta dashed) box in panel (b) ((c)) indicates the IRIS raster FOV. IRIS observed this flare with a large dense 16-step raster with a FOV of 5" × 119" and a step size of 0.35". The flare exhibits a double ribbon structure, with the east ribbon elongating earlier and merging into the west ribbon.

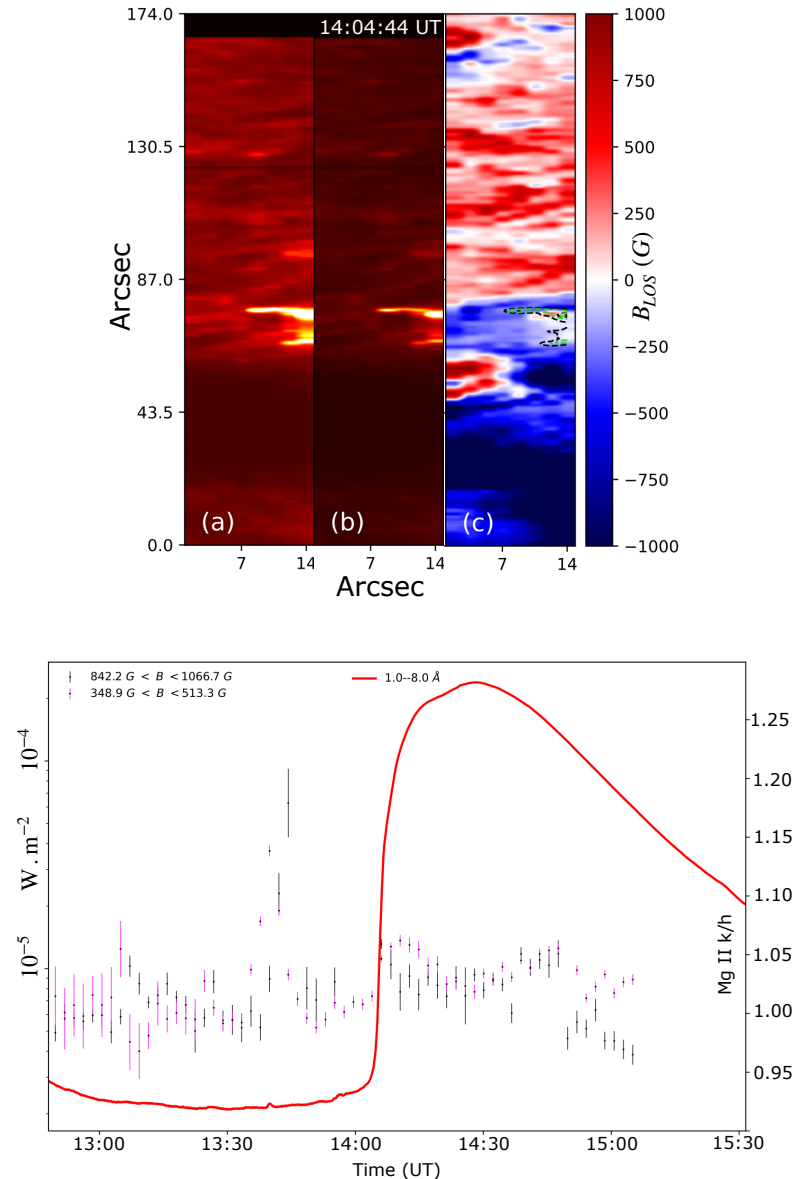


Figure 6.11: Obtained intensity maps in Mg II k (panel a) and h (panel b) lines at the peak of the flare. The rasterized HMI LoS magnetic field density map is shown in panel c. The black and lime green contours on panel c show the contours of Mg II k (panel a) and h (panel b) intensity. Bottom panel: Time evolution of the Mg II k to h line intensity ratio obtained from averaged spectrum over the corresponding magnetic flux bin as labeled for the Oct 22, 2014 flare. The over-plotted red solid line displays the 1–8 Å GOES X-ray light curve.

The IRIS raster scans through the west edge of the west ribbon through its eruption and merging with the east ribbon. Fig. ?? displays the intensity maps obtained in Mg II h & k (panels a & b). The rasterized LOS magnetic field map is shown in panel (c). The black &

green dashed contours in the LOS magnetic field map (panel c) depict the intensity contours of Mg II h & k (panels a & b).

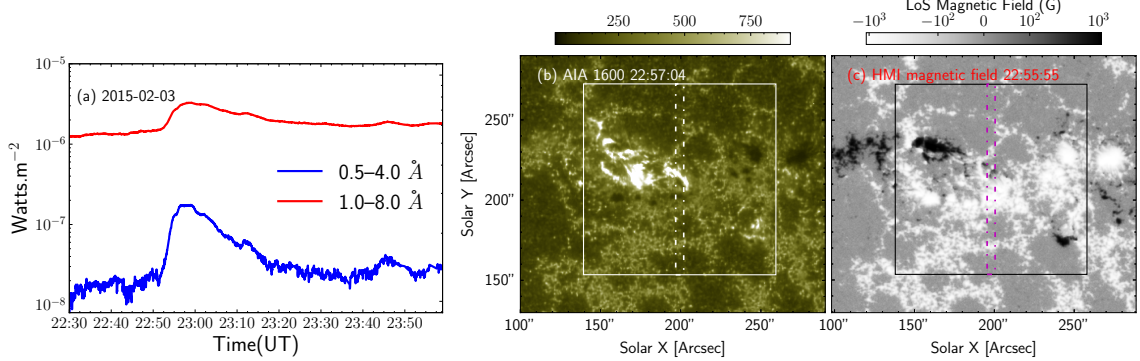


Figure 6.12: The C class flare observed on February 3rd, 2015. Panel a: GOES flux plot in 0.5–4 Å (blue) and 1.0–8.0 Å (red). Panel b: AIA 1600 Å image of the flaring region. Panel c: LOS magnetic flux density map obtained from HMI near the peak of the flare. The over-plotted white (black) boxes in panel b (c) represents the IRIS SJI FOV. The over-plotted white dot-dashed (magenta dashed) box in panel b (c) show the IRIS raster FOV.

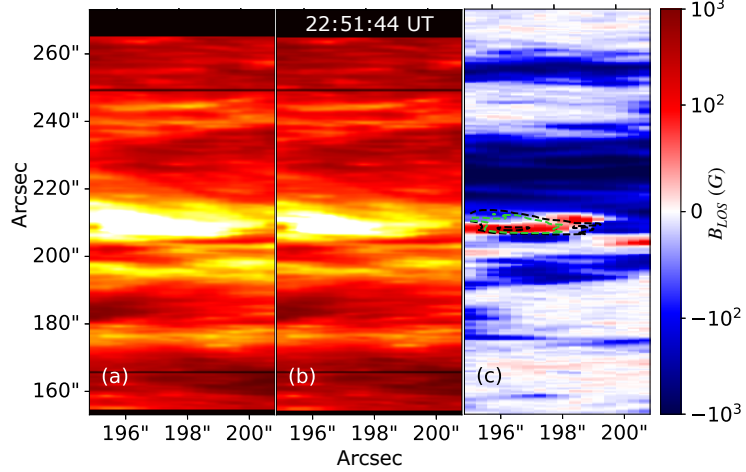


Figure 6.13: Obtained intensity maps in Mg II k (panel a) and h (panel b) lines at the peak of the flare. The rasterrered HMI LOS magnetic field density map is shown in panel c. The black and lime green contours on panel c show the contours of Mg II k (panel a) and h (panel b) intensity.

We present the GOES 1–8 Å light curve (red solid line) alongside the time evolution of the Mg II k to h line intensity ratio averaged within the bins of two different magnetic flux densities as a function of time in Fig. ???. The Mg II k to h line intensity ratio exhibits a similar variation as observed in the M-class flare. It peaks during the impulsive phase ($k/h \sim 1.12$) and decreases to preflare values ($k/h \sim 1.09$) during the decay phase of the

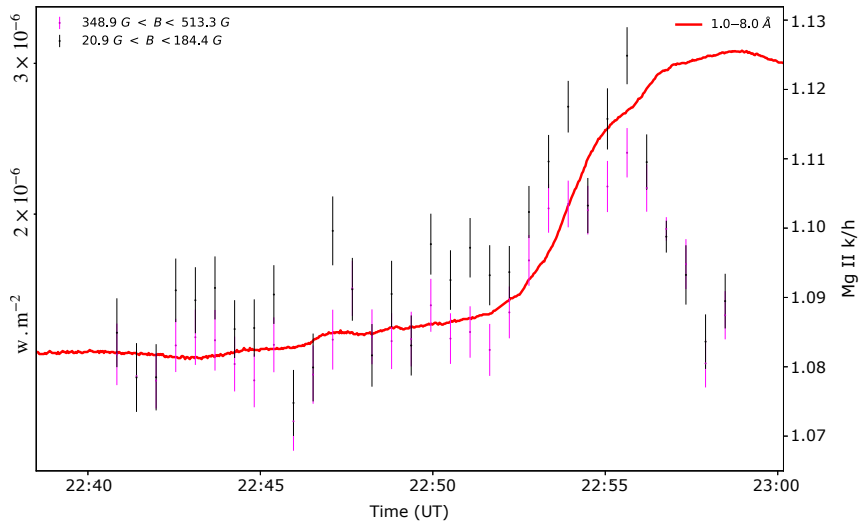


Figure 6.14: Time evolution of the Mg II k to h line intensity ratio obtained from averaged spectrum over the corresponding magnetic flux bin as labeled for the Feb 3, 2015 flare. The over-plotted red solid line displays the 1–8 Å GOES X-ray light curve.

flare, coinciding with the peak of the GOES light curve. It's worth noting that the change in the Mg II k to h line intensity ratio is less pronounced for this flare compared to the M-class event. However, we also observe that the ratio shows a persistent increase from the onset of the flare.

6.4 Summary and Discussion

The Mg II k to h line intensity ratios serve as a valuable diagnostic for assessing the opacity of the local plasma and can provide insights into changes in the local plasma environment within the solar chromosphere during flares. In this study, we investigated the temporal variation of Mg IIk to h line intensity ratios during the evolution of three X-class, M-class, and C-class flares. We also examined the variation of intensity ratios across different magnetic flux density bins, utilizing observations from IRIS and HMI. Co-alignment of IRIS and HMI observations was achieved using 1600Å images recorded by AIA.

It's well-documented that Mg II profiles exhibit significant spatial variations within flaring regions (??). As we binned the IRIS observations based on magnetic field strength, it's important to note that any spatial variation is averaged out and not addressed in our analysis.

Our findings reveal that Mg II k to h line intensity ratios undergo changes during flares. For M-class and C-class flares, the ratio starts increasing at the onset of the flare,

peaks roughly halfway through the impulsive phase, and then steeply declines thereafter (see Figs.?? & ??). Moreover, the ratios drop even below pre-flare levels during the later stages of the flare (peak and decline phase). However, this behavior is observed only in M and C-class flares, not in X-class flares.

Our observations did not reveal any correlation between line intensity ratios and magnetic flux density. The line intensity ratios for different magnetic field strengths illustrated in Figs.??,?? right panel,?? indicate a consistent behavior from weak to strong magnetic field strengths. This suggests that the magnetic field similarly affects both Mg II k and h lines, and such effects cancel out when taking the ratios.

? studied Mg II k to h line intensity ratios and their temporal variation for individual pixels in both quiet Sun regions and flare locations. While no change in ratios was observed for the quiet Sun region, variations were noted in flaring pixels, suggesting possible differences in heating conditions between non-flaring and flaring atmospheres. However, no correlated change in the ratio with respect to the flare light curve was observed.

Our results align with those of ?, wherein they also observe the highest change in the ratio during the impulsive phase of the flare, decreasing before the flare reaches its maximum in GOES 1–8 Å observations. Such variations in the ratio may indicate changes in the optical depth of the local medium. During the impulsive phase, decreased optical depth might be attributed to localized heating and chromospheric evaporation, while during the decay phase, increased optical depth could be due to condensation and downflows. However, this interpretation remains speculative, particularly as we did not observe such effects in X-class flares.

The results obtained for M-class and C-class flares can be explained by the aforementioned scenario, but the findings for X-class flares are more ambiguous. We couldn't establish a clear distinction in the general properties of these three flares. Notably, while the C-class flare is confined, both M and X flares are eruptive. Therefore, it's plausible that in X-class flares, energy deposition occurs more impulsively and on a shorter timescale than can be sampled. This high impulsiveness may lead to a greater degree of ionization of the medium compared to the other two flares, as supported by the large number of saturated pixels in the data that were discarded. A more definitive conclusion would necessitate analysis of additional such flares, including numerical and theoretical modeling.

The SUIT has four separate narrow band filters for the Mg window, namely NB2 (Blue wing of Mg II k), NB3 (Mg II k), NB4 (Mg II h) and NB5 (Red wing of Mg II h). As mentioned in chapter ?? SUIT observes the full-disk Sun continuously in NB4 with \sim 1 minute cadence and full-disk observations in all eleven science filters every 90 minutes. With the full disk observations in all science filters, we can investigate the opacity variations continuously across various solar features with a cadence of 90 minutes with the NB3 and NB4 ratio. In flare mode, the observing filter sequence is customizable. With high cadence observations in NB3 and NB4, we can investigate the effect of flare heating on the local

plasma environment via its manifestation in opacity.

Chapter 7

First flares observed by *SUIT*

This thesis chapter originally appeared in the literature as

Near- and Mid-ultraviolet Observations of X-6.3 Flare on 2024 February 22 Recorded by the Solar Ultraviolet Imaging Telescope on board Aditya-L1, Roy, S., Tripathi, D., Padinhatteeri, S., & Ramaprakash, A. N., et. al., 2024, ApJL, 981, L19, doi:[10.3847/2041-8213/adb0be](https://doi.org/10.3847/2041-8213/adb0be).

7.1 Introduction

As alluded to earlier in chap. ??, flares manifest differently across various wavelengths. It is known that the foot-points of the post-flare loops are observed in hard X-rays (due to electrons) and γ rays (due to ions). However, the post-flare loops themselves are observed in soft X-ray and Extreme Ultraviolet (EUV) (??). The corresponding white light and Near Ultraviolet (NUV) counterparts are believed to arise due to changes in ionization and local opacity in the photospheric and chromospheric heights. The NUV and white light emission have also been demonstrated to be co-spatial and co-temporal with hard X-ray (??).

One of the major puzzling aspects regarding the origin and energetics of solar flares is the origin of the white light (WL) continuum. According to the standard model of flares, the energetic electrons are accelerated along the loops and are stopped via numerous collisions and thermalization when the ambient medium has enough density, usually known as the ‘thick target’ model (see ???, for further details). It is believed that such densities are already present within the chromosphere, explaining the co-spatiotemporal nature of WL and Hard X-ray emission. The theoretical estimations, on the other hand, predict that parts of the WL emission may originate in the upper photosphere, i.e., depths which are inaccessible to electrons in the standard ‘thick-target’ model.

There have been various attempts to modify the thick target model to account for various observations from solar flares, e.g., a warm target model (??), local re-acceleration

of electrons (?), acceleration of protons along with electrons which are expected to penetrate deeper. There were also attempts to explain the source of WL with photospheric ‘back-warming’ (?), where the upper photosphere is ionized via energy transported radiatively from the chromosphere. There have been several observations where the WL emission has been associated with enhancement observed in the 2832 Å continuum of IRIS SJI (?????).

In this chapter, we discuss the X-class flare recorded by the Solar Ultraviolet Imaging Telescope (SUIT; ??) on board Aditya-L1 (?) on February 22, 2024. This is the first flare that was localized and observed with the onboard flare detection module. The rest of the **chapter** is structured as follows: in §??, we discuss the observations of the flare and the dataset used for its study. §?? we discuss the data analysis and results. Finally, in §??, we summarize, conclude and discuss the importance of these observations in flare studies.

7.2 Observations and Data

Active Region NOAA 13590 appeared on Feb. 18, 2024, at the northeast limb of the solar disk. On Feb. 22, 2024, it was located at N17E26 with $\beta\gamma\delta$ configuration and produced multiple flares, including the M4.8, X 1.7 and X6.3.

Using the onboard flare detection algorithm based on intensity thresholding (?), SUIT detected, localized and observed the X6.3 flare in flare mode. SUIT instrument carries 11 filters (8 narrow bands and 3 broad bands) tuned to observe the solar photosphere and chromosphere at various wavelengths in 200-400 nm wavelength range (see Table ??). SUIT provides images at a pixel size of 0.7''. The four out of eight narrow band filters are tuned to observe the Mg II blue wing continuum (NB2), Mg II k (NB3), Mg II h (NB5) and Mg II red wing continuum (NB5). The NB6 and NB7 continuum filters are towards the blue and red sides of the Balmer jump (364.5 nm), respectively.

It provides both full disk and region of interest (ROI) observations as per the observational sequence being used. While in regular observations, the ROI is defined using ground commands, flare mode automatically defines the ROI based on the detected location and observes in the eight narrowband filters. Under this observation mode, the temporal cadence is \approx 1 min. SUIT did not detect the X1.7 as the spacecraft was off-pointed for the stellar calibration sequence. The X6.3 flare that SUIT detected started at 22:08 UT and peaked at 22:34 UT. In the flare mode, it was observed in all eight narrowband filers. The flares were also observed by GOES, *SDO/AIA*, *SO/STIX*, GONG H α . In this study, we have used AIA 1600 & 1700 Å, GONG H α images and full disk integrated GOES soft-ray (1–8 Å) and STIX Hard X-ray (25–50 keV) along with SUIT observations.

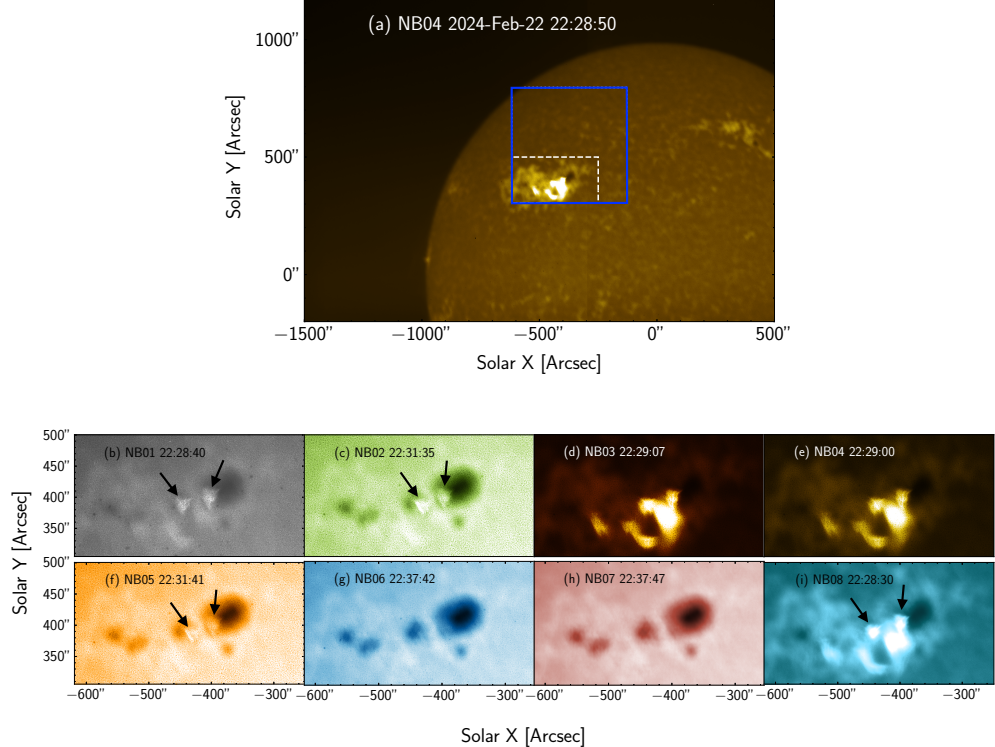


Figure 7.1: (a) Parts of the full-disk ($2k \times 2k$) observation in NB4 (Mg II h) showing the flaring region and sunspot. The over-plotted blue box shows the RoI localized by the onboard flare detection algorithm, and the white dashed box locates the region used for the subsequent analysis. (b) SUIT Narrowband images recorded at the peak of flares in the respective filters. The size of the images corresponds to the white-boxed region shown in panel a. The arrows mark the two bright umbral kernels.

7.3 Data Analysis and results

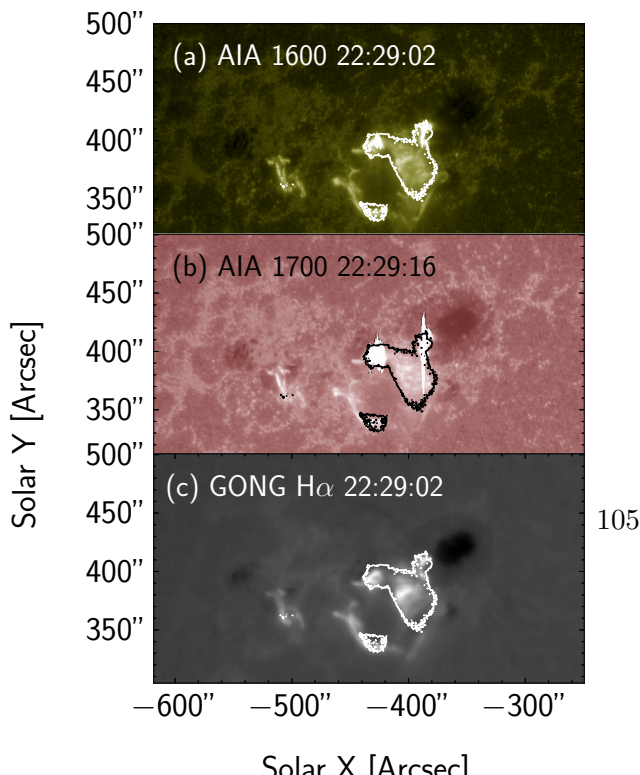


Figure ??a displays shows a cutout of the full-disk ($2k \times 2k$) image taken in NB4 (Mg II h) filter. The over-plotted blue box shows the region of interest automatically defined by the onboard flare detection algorithm. As we can see, the auto-defined RoI fully covers the flare. The flare detection algorithm is designed to define the RoI, which is centred on the flaring region. In the current observation, we can see that the RoI is not properly centred at the flare. However, since then, various parameters of the flare detection and localization algorithm

have been tweaked to achieve better detection and localization. The white dashed box locates the region we have considered for further study in this chapter. Fig. ??-b-i displays the flares in each narrow band filter at their respective peak. The field of view (FOV) corresponds to the dashed white box in panel a. As can be seen, the flare is observed in all the narrow band filters of SUIT, including the two flare kernels observed as penumbral brightening, which are located by black arrows.

In Fig. ??, we plot the flare as observed in each narrow band filter at the peak intensity in NB3(Mg II k). The over-plotted black contours represent 60% of the peak intensity observed in NB3. The features observed in NB8 (Ca II h) are very similar in morphology to those in NB3 and NB4. While there appears to be a hint of such features in other continuum channels, it is not clearly discernible.

To compare the SUIT observations with those from AIA and H α , in Fig. ??, we plot display AIA 1600 (panel a), AIA 1700 (panel b) and GONG-H α recorded at near simultaneous time to the peak of NB3 observations. The over-plotted contours are the same as those in Fig. ???. These images clearly reveal the presence of clear signatures of the flare kernels in AIA UV and H α observations, co-spatial to the NB3 (Mg II k) observations.

In order to understand the temporal evolution of the flare, we plot the lightcurves in Fig. ?? obtained from various filters of SUIT, GOES, STIX, AIA 1600 & 1700, and GONG H α , as labelled. Note that the GOES and STIX lightcurves are full Sun integrated, whereas those for other observations are obtained over the contoured region Figs. ?? & ??,

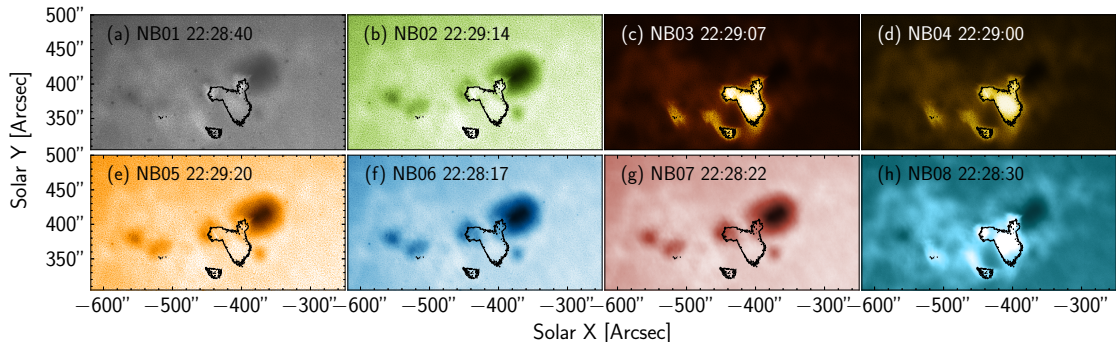


Figure 7.3: Flare as observed in all narrow band filters at the time of peak intensity in NB3. The over-plotted black contours show 60% of the peak intensity observed in NB3.

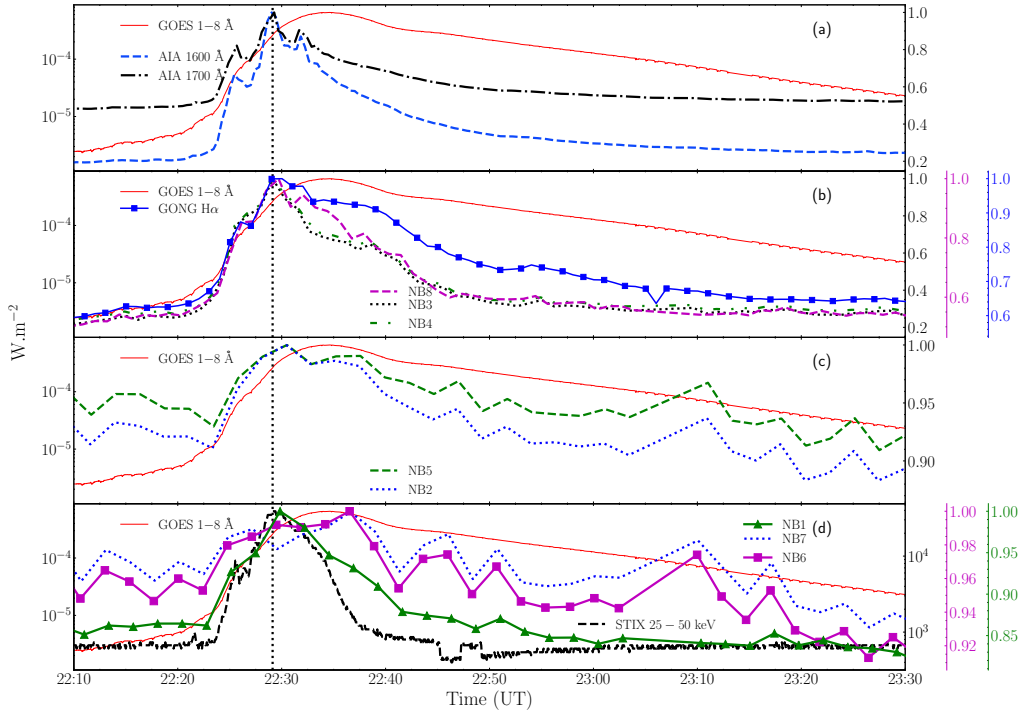


Figure 7.4: Light curves obtained over the contoured region from AIA 1600 (blue dashed), AIA 1700 Å (black do-dashed), NB3 (black dotted), NB4 (green dot-dashed), NB8 (magenta dashed), NB2 (blue dotted), NB5 (green dashed), NB1 (green triangles), NB6 (magenta squares) and NB7 (blue dotted) as labelled. For comparison, we have also over-plotted the light curves obtained from co-aligned GONG H-alpha observations (blue squares) in panel (a), full-sun integrated GOES/SXR in 1–8 Å (red solid) and STIX/HRX (black dashed) in panel (c).

and normalized to their respective max intensities. The vertical dotted black line across all the panels locates the peak intensity in NB3.

The lightcurves reveal that the flare peaks in all the SUIT channels (except NB6 and NB7), AIA 1600 & 1700, H α and STIX before it achieves its maximum intensity in GOES. The STIX peak coincides with that in SUIT NB1, NB3, NB4, NB8 as well as AIA and H α . Note that SUIT NB3, NB4 and NB8 primarily observe the chromospheric signatures, similar to GONG H α . Fig. ??,b, shows that the lightcurves of NB3, NB4, and NB8 peak at the same time around $\sim 22:29$ UT, which is similar to that H α . However, NB8 and *GONG-H α* show less contrast variation ($\sim 40\%$ change for NB8 (Ca II h) and GONG H α , compared to the $\sim 80\%$ change for NB3 (Mg II k) and NB4 (Mg II h)) than that shown by NB3 and NB4. This may be attributed to the larger enhancement in the continuum in NB8 (Ca II) and H α than that in Mg II.

Figure ??,c shows that the lightcurves of SUIT NB2 and NB5 (blue and red wing of Mg II) peak about 3 minutes after the NB3 peak (also STIX hard X-ray peak). This is also apparent in the images shown in Fig ???. Moreover, unlike other lightcurves, NB6 and NB7 lightcurves do not show a gradual increase and decrease. Instead, they exhibit a rather sharp rise, albeit very small ($\sim 0.03\%$), in intensity during the impulsive phase of the flare.

7.4 Summary and Discussion

In this **chapter**, we have performed a multi-wavelength study of the X-6.3 flare observed on Feb 22, 2024, using the observations recorded by SUIT, AIA, STIX and GONG. Moreover, this is the first flare detected and localized by the onboard algorithm for flare identification on SUIT and observed in flare mode. Below we summarize the obtained results.

- The flare is observed in all narrow band filters of SUIT. The flare was also observed in AIA 1700 and 1600, GONG H α , GOES soft X-rays (SXR) and STIX hard X-rays (HXR).
- The flare peak in all SUIT channels (except NB6 and NB7) and those in AIA 1600 & 1700 \AA , GONG H α and STIX HXR observations and is ~ 5 minutes prior to the GOES SXR peak. The flare peaks are observed in NB6 and NB7 after ~ 3 minutes after the GOES SXR peak.
- The flare peak in NB3 and NB4 coincides with that in AIA 1600 & 1700 \AA and STIX 25–50 keV observations.
- The flare attains its peak in NB2 and NB5, blue and red wing of Mg II lines, after about 3 minutes it does in NB3.

The results demonstrate that the flare signatures detected by SUIT in all its narrow band channels are very tightly related to HXR observations recorded by STIX. These results

CHAPTER 7. FIRST FLARES

highlight the first *SUIT* observations of an X-class flare. The observations of flare kernels and enhancement in the intensity in the red wing of the Mg II window, i.e., NB5 is similar to those observed by ??? using the observations recorded by the Interface Region Imaging Spectrometer (IRIS, ?). For the flare studied here, we also detect the bright kernels and intensity enhancements in the blue wing of the Mg window, i.e., in NB2 filter. To the best of our knowledge, this is the first such observation in the blue wing of Mg II. Unfortunately, we can not comment on the spectral nature of the bright kernels as *SUIT* is only an imager. Further exploration is necessary to comment on the spectral nature of the bright kernels and their possible origin. It is important to highlight that in the observation reported by ?, the appearance of flare kernel and intensity enhancement in SJI recorded at 2832 Å (similar to *SUIT* NB5 filter) corresponded with a plethora of photospheric absorption lines, mostly Fe II, turning into emission, which was attributed to photospheric heating. Therefore, no such analysis was possible.

Chapter 8

Echoes of the Solar Inferno: Summary and Future Prospects

Solar flares are the most powerful magnetic events in the solar system, characterized by sudden, localized brightening in the solar atmosphere. The energy released during a flare can affect space weather and disrupt systems such as satellite communications, GPS, power grids, etc., including serious risks to astronauts and spacecraft in orbit. Studying the underlying physics of solar flares helps us better predict these events and mitigate their impacts, which is critical for the safety of both space-based infrastructure and terrestrial technology. The extensive observations of flares, especially in soft X-ray, hard X-ray, and EUV wavelengths, we have developed a tremendous understanding of the physical processes at work in flares. However, numerous important questions about the origin and evolution of thermal and non-thermal energies in solar flares, their spectral distribution, and the precise mechanisms behind flare initiation remain.

The primary aim of this thesis is to perform a multi-wavelength study of solar flares using existing observations and also contribute towards the development of the new observing facility, the Solar Ultraviolet Imaging Telescope (SUIT) onboard Aditya-L1 that provides crucial data for flare studies. The thesis is structured in two parts. In the first part, we address some of these questions by analyzing the temporal evolution of thermal and non-thermal energies in solar flares using EUV and X-ray data from multiple vantage points. In the second part, we conduct preparatory studies for SUIT that include modeling the instrument's performance, assessing spacecraft jitter profiles, establishing calibration methods using stellar observations, and forward modeling of mock SUIT observations. Below, we provide a detailed summary of the work and results that were obtained.

1. The partition between the thermal and the non-thermal energies in solar flares informs us about the relevant physical process taking place during the evolution of the flare. As discussed in §??, several statistical studies of solar flare energetics (e.g.,

???????) have reported on the partition between the thermal and non-thermal energies of the flares. It can be inferred that for bigger flares (e.g., M and X class), there is enough non-thermal energy in electrons to power the thermal radiation. In comparison, there seems to be a deficit in the non-thermal component for the smaller flares. This prompted speculation about a third energy source that could account for the deficit of energy needed to power the thermal component in smaller flares. One of the key similarities of all of these studies was the use of peak thermal energy as the representative of the total thermal energy of the flares. While that is a fair representation of the overall thermal energy budget of an event, it can miss several intricacies throughout the evolution of the flare. In this thesis, we study two flares, one on disk and the other off-limb. We use AIA and XRT observations to compute DEMs and infer the thermal properties of the flaring plasma. We use observations from AIA and EUVI, from a different vantage, to triangulate the LoS through the flaring plasma. We find that the thermal energy estimation for solar flares can be significantly affected by the volume estimates of the flaring plasma in the impulsive phase. For the November 29, 2020, limb event, we also demonstrated directly from the calculated thermal energy that the cooling pattern of fans is different than the post-flare loops, thereby indicating a possibly different heating mechanism. A hint of such observations has already been alluded to in various existing studies (e.g., ???).

2. Estimating the imaging performance of *SUIT* was one of the priorities to characterize and quantify the possible science cases. To this end, we designed a pipeline to create mock *SUIT* observations using simulated MURaM cubes. We incorporated lab-measured PSF in the pipeline to create realistic mock observations. The measured PSF across various channels show $\sim 2''$ radius of 80% FWHM for the PSF. This illustrates that the imaging from *SUIT* would be able to resolve features $\sim 2''$ apart with reliable photometric accuracy.
3. The intensity ratios of the Mg II k and h lines can be used to probe the characteristics of the plasma in the **lower solar atmosphere in chromosphere and transition region heights**. To obtain the plasma characteristics in flaring regions, we study the variation of Mg II k and h intensity ratio for three areas belonging to X-class, M-class, and C-class throughout their evolution. For this purpose, we used existing IRIS observations combined with those from AIA, HMI and GOES X-ray light curves. We co-aligned IRIS 2796 Å observations with those from HMI and obtained artificially rastered magnetic field maps corresponding to IRIS maps. This gives us the measure of the photospheric magnetic field for every pixel of the IRIS rasters. We use a double Gaussian function with a symmetric background about the line core to fit the Mg II k and h lines. In scenarios where the Mg triplet lines are in emission, they are fitted with separate Gaussian functions. We find that the intensity ratios show significant changes during flares, i.e., it peaks minutes before the GOES SXR peak and falls even below the pre-flare level during the peak and decline phase of the flare. A comparison with photospheric magnetic flux density suggests that the change in ratio is independent

of flux density. Given that the Mg II k to h line intensity ratio is representative of the opacity of the local plasma environment, these results are important in the light of heating and cooling of localized plasma and provide further constraint on the understanding of flare physics.

4. The several flares observed via *SUIT* give us a new perspective on observing various eruptions and how they interact with the local plasma environment. Here, we report the observation of the first flare X6.3 flare SOL2024-02-22T22:08:00 that was localized and observed with the eight narrow band (NB) filters of *SUIT*. We have also used the co-spatiotemporal observations from SDO/AIA, SolO/STIX and Global Oscillation Network Group (GONG) H α and GOES. We align and co-register *SUIT* observations with those from AIA 1600, 1700 Å and GONG H α observations and construct light curves from the same regions on them. We compare these light curves with the full-disk integrated GOES SXR and STIX HXR (25–50 keV) light curves. We find that all of the *SUIT* NB1, NB3, NB4, NB8 filters peak simultaneously with HXR and 1600, 1700 Å. In contrast, the NB3 and NB5 lines peak \sim 3 minutes later than the HXR peak. The flare peaks in NB6 and NB7 \sim 3 mintes after the GOES soft X-ray peak. To the best of our knowledge, this is the first observation of flare in these wavelengths (except in NB3, NB4 and NB5). Moreover, for the first time, we show the presence of bright kernel NB2. These results demonstrate the capabilities of *SUIT* observations in flare studies.

The results obtained in this thesis help us understand various puzzles of solar flares and provide a number of constraints on the modeling. Additionally, they open up several pathways to further explore the physics of flares. The observations from the *SUIT* instrument open up a new window for studying solar flares. Below we describe a few projects that naturally arise based on this study.

- Our results in Chap. ?? emphasize the critical role of accurate volume estimation in determining the thermal energy of solar flares. Discrepancies in volume estimation, particularly during the impulsive phase and thermal peak, may lead to overestimation of thermal energy because rapid changes in plasma volume occur during these stages. Therefore, we plan to automate the triangulation method to determine the LoS from earth vantage using observations from various instruments and conduct rigorous statistical studies across different flare classes to understand how volume estimation impacts thermal energy calculations.
- As alluded to in Chap. ??, we did not observe the correlated change in line intensity rations for the X-class flare. It is possible that the change was not observed for the X class flare, simply due to the cadence limitations of IRIS raster scan, along with which regions of the flare arcade are being scanned by IRIS because it is well known that the Mg II profiles vary significantly in shape and spatially within the flaring region (??). The other and more interesting possibility is that in some of the events, depending

CHAPTER 8. SUMMARY & OUTLOOK

on their "impulsiveness", there might be different degrees of ionization at play in the chromosphere. This may also indicate a different energy release mechanism during the pre-flare and impulsive phases of the flare.

- *SUIT* provides the first full-disk solar imaging in 11 filters in the wavelength range of 200–400 nm. There are previous flare observations in some of the imaging channels , *e.g.* NB3, NB4 and NB5 from *IRIS* and NB8 from *Hinode/SOT*, only in smaller spatial windows.

Appendix A

Calculation of Oscillator strengths for the Mg II k & h lines

For a transition from $u \rightarrow l$ the oscillator strengths can be expressed as:

$$f_{lu} = \lambda_{lu}^2 \times \frac{g_u}{g_l} \times C_1 \times A_{ul}$$

Where, λ_{lu} is the transition wavelength, g_u and g_l are the degeneracy of the upper and lower level and A_{ul} is the Einstein coefficient for spontaneous emission. Since the Mg II k and h line transitions happen to same lower energy state from two upper energy states of slightly different energy, this gives us:

$$\frac{f_k}{f_h} = \left(\frac{\lambda_k}{\lambda_h} \right)^2 \frac{g_k A_k}{g_h A_h} \quad (\text{A.1})$$

Both the k and h line transitions are dipole transitions. In case of dipole transitions, the Einstein A coefficient can be expressed as:

$$A_{ul} = \frac{C_2}{\lambda^3} |\langle l | r | u \rangle|^2 \quad (\text{A.2})$$

where, λ is the transition wavelength, J_u is the total angular momentum quantum number of the upper state. This gives us from eqn. ??,

$$\frac{f_k}{f_h} = \frac{\lambda_h g_k}{\lambda_k g_h} \frac{|\langle 3p \ ^2P_{3/2} | \vec{r} | 3s \ ^2S_{1/2} \rangle|^2}{|\langle 3p \ ^2P_{1/2} | \vec{r} | 3s \ ^2S_{1/2} \rangle|^2} \quad (\text{A.3})$$

Now the radial part of the states $3p \ ^2P_{3/2}$ and $3p \ ^2P_{1/2}$ would be same and cancel out. So, the ratio would depend on the angular part of the wavefunctions. The reduced matrix element for electric dipole transitions between fine-

APPENDIX A. OSCILATOR STRENGTH CALCULATION

structure states is related to the LS-coupled reduced matrix element by the Wigner-Eckhart theorem:

$$\langle n'l'j'| r^{(1)} |nlj\rangle = (-1)^{l'+s+j+1} \sqrt{(2j'+1)(2j+1)} \left\{ \begin{matrix} l' & j' & s \\ j & l & 1 \end{matrix} \right\} \langle n'l' | r^{(1)} |nl\rangle \quad (\text{A.4})$$

where $r^{(1)}$ is the radial part of the position vector operator. For Mg II the relevant quantum numbers are:

- $l = 0$ (S state), $l' = 1$ (P state)
- $s = 1/2$
- $j = 1/2, j' = 1/2$ or $3/2$

Evaluating the 6j symbols we get:

- For $j' = 3/2$: $\left\{ \begin{matrix} 1 & 3/2 & 1/2 \\ 1/2 & 0 & 1 \end{matrix} \right\} = 1/\sqrt{6}$
- For $j' = 1/2$: $\left\{ \begin{matrix} 1 & 1/2 & 1/2 \\ 1/2 & 0 & 1 \end{matrix} \right\} = -1/\sqrt{3}$

This gives us:

$$\frac{|\langle 3p^2 P_{3/2} | \vec{r} | 3s^2 S_{1/2} \rangle|^2}{|\langle 3p^2 P_{1/2} | \vec{r} | 3s^2 S_{1/2} \rangle|^2} = \frac{4 \cdot \frac{1}{6}}{2 \cdot \frac{1}{3}} = 1 \quad (\text{A.5})$$

Plugging this back into eqn. ?? we get,

$$\frac{f_k}{f_h} = \frac{\lambda_h}{\lambda_k} \times \frac{g_k}{g_h} = \frac{2 \cdot \frac{3}{2} + 1}{2 \cdot \frac{1}{2} + 1} = \frac{4}{2} = 2$$

where $\frac{\lambda_h}{\lambda_k} \simeq 1$.

Appendix B

Modifications of the cold thick target model

The regular observations of solar flares in Soft and Hard X-ray points towards the "thick-target" interpretation (?) of flare accelerated electron injection into the Chromosphere. ? coined the source-integrated density weighted mean electron flux $\langle nVF \rangle(E)$ [e⁻cm⁻²s⁻¹keV⁻¹]. The observed hard X-ray spectrum then can be expresses as

$$I(\epsilon) = \frac{I}{4\pi R^2} \int_{\epsilon}^{\infty} Q(\epsilon, E) \langle nVF \rangle(E) dE \propto \epsilon^{-\gamma} \quad (\text{B.1})$$

where R is the distance between the observed and the Sun, and $Q(\epsilon, E)$ is the angle-averaged bremsstrahlung cross section. The usual cold thick target model gives the relation between the mean electron flux and the injected electron rate as

$$\langle nVF \rangle(E) = \frac{E}{K} \int_E^{\infty} \dot{N}(E_0) dE_0 \quad (\text{B.2})$$

$K = 2\pi e^4 \ln(\Lambda)$ is the collision parameter, e is the electron charge in esu and $\ln(\Lambda)$ is the Coulomb logarithm(?). The limitations of the standard "thick-target model" becomes more evident when we try to define the accelerated electron spectrum from eqn. ?? and ?? we get

$$\dot{N}(E) = \dot{N}_0 \frac{\delta - 1}{E_c} \left(\frac{E}{E_c} \right)^{-\delta} \quad (\text{B.3})$$

where $\delta = \gamma + 1$. Here, E_c is an arbitrary reference energy called the low energy cutoff, to stop the total rate of injected electron, $\dot{N}_0 = \int_{E_c}^{\infty} \dot{N}(E_0) dE_0 [s^{-1}]$ from diverging. The associated total power in the electron is given as

$$P[keV.s^{-1}] = \int_{E_c}^{\infty} E_0 N(E_0) dE_0 = \frac{1}{\delta - 2} E_c^{2-\delta} [N(E_c) E_c^{\delta}] = \frac{\delta - 1}{\delta - 2} E_c \dot{N}_0 \quad (\text{B.4})$$

As a consequence various physical properties become very strongly dependent on the low energy cut off. The low energy cut off results in non-physical discontinuous electron distribution of a Maxwellian and power law electron distribution. There are several different attempts to mitigate the nonphysical divergence of the thick target power law injection of electrons at lower energies. ?? assumed a warm-target corona and cold chromosphere and included energy diffusion, transport and thermalization of the injected electrons through a warm layer of plasma on top of the cold target to rewrite eq. ?? as

$$\begin{aligned} \langle nVF \rangle(E) &= \frac{E}{2K} e^{-E/k_B T} \int_{E_{min}}^E \frac{e^{E_0/k_B T}}{E_0 G(\sqrt{E_0/k_B T})} dE_0 \times \int_{E_0}^{\infty} \dot{N}(E_0) dE_0 \\ &\simeq \Delta EM \sqrt{\frac{8}{\pi m_e}} \frac{E}{(k_B T)^{3/2}} e^{-E/k_B T} + \frac{E}{K} \int_E^{\infty} \dot{N}(E_0) dE_0 \end{aligned} \quad (\text{B.5})$$

where ΔEM is the "thermalized emission measure" which is created via the thermalization of the electrons and can be written as

$$\Delta EM \simeq \frac{\pi}{K} \sqrt{\frac{m_e}{8}} (k_B T)^2 \frac{\dot{N}_0}{E_{min}^{1/2}} \text{ where } E_{min} \simeq 3k_B T \left(\frac{5\lambda}{L}\right)^4 \quad (\text{B.6})$$

where $\lambda = (k_B T)^2 / 2Kn$ is the collisional mean free path of the injected electrons. The half loop length L, temperature T and number density n are the physical parameters associated with the coronal loops, through which the electrons are injected. This is known as the "warm target model". Although this model still features a low energy cutoff to the injected electron spectrum, the cutoff is now not ad hoc, and determined by the collisional parameters of the electrons through the coronal loops which in turn are determined by the physical thermal properties of the coronal loops. While the warm target model attempts to explain the physical significance of the low energy cutoff, the use of a κ -distribution injection of electrons has also proven to be very promising. The κ -distribution is regularly used to model the electron spectrum in in-situ observations and magnetic reconnection events in the Earth atmosphere (??).

Close to the low energy cut off usually it is expected that Langmuir waves will be generated and grow(??). The interaction between the waves and the injected electron would flatten the energy energy distribution around the low energy cut off. To reflect this various studies (???) have used the Kappa distribution, consisting of a Maxwellian core and smoothly merged power-law tail, along with a prominent thermal component to fit the observed X-ray spectrum. Apart from not requiring an arbitrary low-energy

APPENDIX B. KAPPA DISTRIBUTION FIT

cutoff E_c , the kappa distribution can provide crucial information on the finer details of the electron acceleration, including the physical conditions of the chromosphere (*e.g.* wave-particle interaction, beam-plasma interaction etc.) responsible for the origin of it. ?? demonstrated that, in presence of Coulomb collisions and velocity diffusion the stochastic acceleration of electrons during solar flares can result in κ -distribution. In addition, as the κ -distribution covers the complete energy spectrum and is well behaved throughout, it can provide information about the electrons at a very low energies, which is not sensitive to exchange instruments but can be observed via diagnostics from EUV observations.

? derived the κ -distribution as a result of stochastic acceleration in collisional plasma as

$$f_k(v) = \frac{n_k}{\pi^{3/2} v_{te}^3 \kappa^{3/2}} \frac{\Gamma(\kappa)}{\Gamma(\kappa - \frac{3}{2})} \left(1 + \frac{v^2}{\kappa v_{te}^2}\right)^{-\kappa} \quad (\text{B.7})$$

where $\kappa = \tau_{acc}/2\tau_c$ is the kappa index, the ratio of acceleration and collisional decelerations time scale, v_{te} is the thermal speed ($\frac{1}{2}m_e v_{te}^2 = k_B T_\kappa$). The injected electron rate spectrum and the velocity distribution of the injected electron is given by, $\dot{N}(E) dE = A v f_k(v) d^3v$, where A is the injection area. For an isotropic electron distribution ($d^3v = 4\pi v^2 dv$), plugging in eqn. ?? we get:

$$\dot{N}(E) = A \sqrt{\frac{8}{\pi m_e k_B T_\kappa}} \frac{n_k \Gamma(\kappa)}{\Gamma(\kappa - \frac{3}{2})} \frac{E/k_B T_\kappa}{(1 + E/\kappa k_B T_\kappa)^\kappa} \quad (\text{B.8})$$

where $n_k [\text{cm}^{-3}] = \int f_k(v) d^3v$ is the total electron number density. So, the total electron injection rate is given by

$$\dot{N}_0 = \int_0^\infty \dot{N}(E) dE = 2A n_k \sqrt{\frac{2k_B T_\kappa}{m_e}} \frac{\kappa^{1/2}}{(\kappa - 2) B(\kappa - 3/2, 1/2)} \quad (\text{B.9})$$

pluggin eqn. ?? back into eqn. ?? we get,

$$\dot{N}(E) = \frac{\dot{N}_0}{k_B T_\kappa} \frac{(\kappa - 1)(\kappa - 2)}{\kappa^2} \frac{E/k_B T_\kappa}{(1 + E/\kappa k_B T_\kappa)^\kappa} \quad (\text{B.10})$$

the associated total power in the electrons is given by,

$$P = \int_0^\infty E_0 N(E_0) dE_0 = \frac{2\dot{N}_0 k_B T_\kappa \kappa}{\kappa - 3} \quad (\text{B.11})$$

We fit the STIX spectra in the same time window as shown in Fig. ?? with a *vth+thick_warm* and *vth+thick_warm_kappa* model to compare the two models. We show the *vth* (solid green) + *warm kappa* electron injection model (solid yellow) fit in Fig. ?? top panel. Fig. ??

APPENDIX B. KAPPA DISTRIBUTION FIT

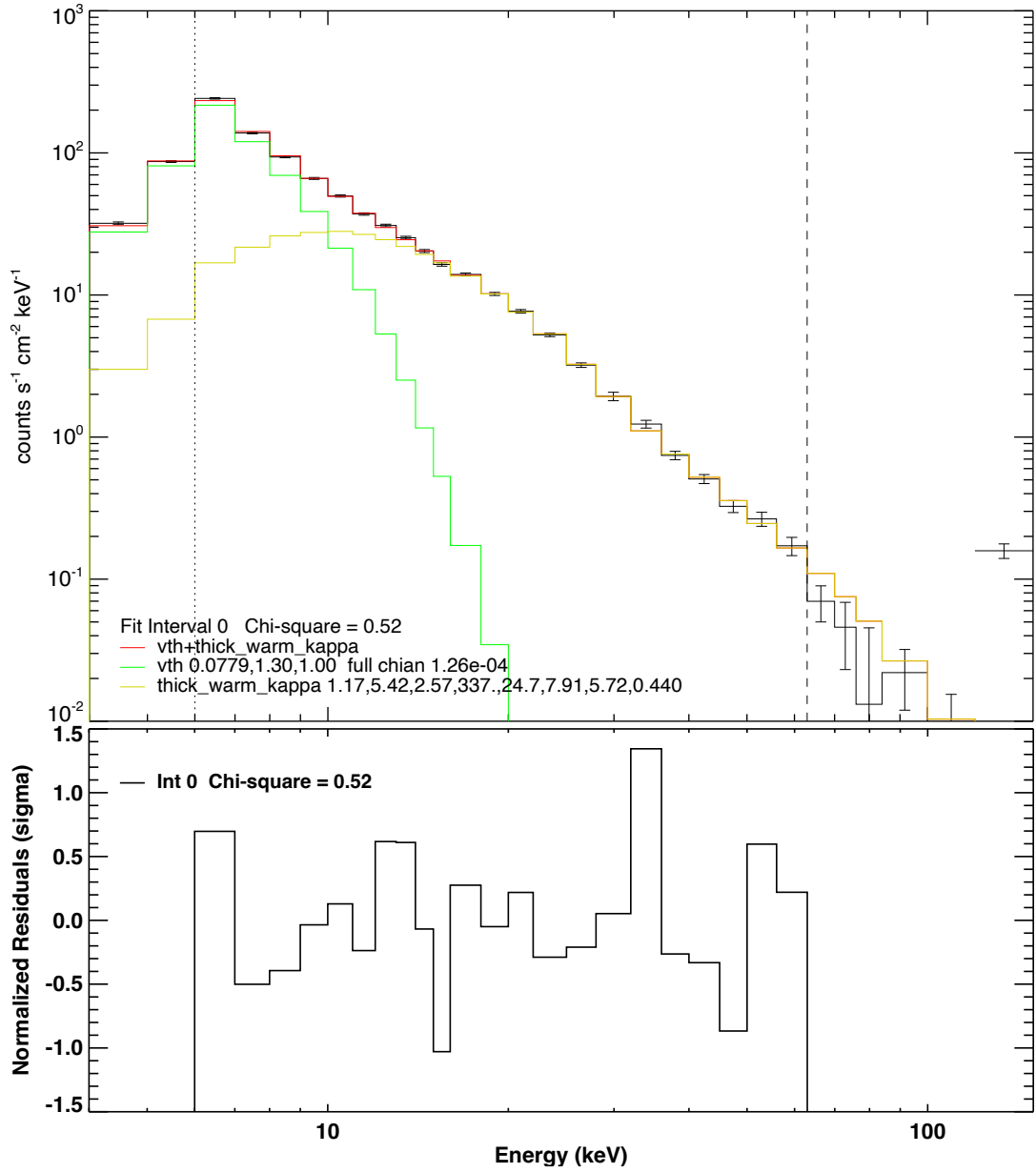


Figure B.1: Top panel: STIX spectra integrated between 15:27:00–15:27:10 UT during impulsive phase, fitted with ‘thcik_warm_kappa’ (solid yellow), ‘vth’ (solid green) and the complete fit function ‘vth+thick_warm_kappa’ (solid red line). Bottom panel: The residue of the fit of the STIX spectra.

APPENDIX B. KAPPA DISTRIBUTION FIT

lower panel shows the normalized residual of the fit. In Tab. ?? we list the relevant fit parameters from the two respective models. We show the inferred electron injection rate as a function of the electron energy for the *warm target+ power law-electron* injection (solid blue) and *warm target+ κ -electron* injection (dashed red) in Fig. ?? from the fit parameters listed in Tab. ?? for the two distinct electron models. The key thing to notice is the very similar behavior of the models at the higher energy end. The power law injection model goes to 0 very abruptly at the lower energy cutoff (E_c), while the kappa distributed electrons slowly taper off at the lower energy end, providing a more physical picture of the injected electron spectra.

Parameters	<i>vth+thick_warm_kappa</i>	<i>vth+thick_warm</i>
EM[10^{49} cm^{-3}]	0.078	0.078
$k_B T[\text{keV}]$	1.30	1.30
$\dot{N}_0[10^{35} \text{ e}^{-1}.\text{s}^{-1}]$	1.17	1.89
δ	NA	3.21
κ	5.42	NA
E_c	NA	.76
$k_B T_\kappa$	2.57	NA

Table B.1:: Comparison of various model parameters between "*vth+thick2*", "*vth+thick_warm*" and "*vth+thick_warm_kappa*" model for the same time window of STIX spectra as shown in Fig. ??.

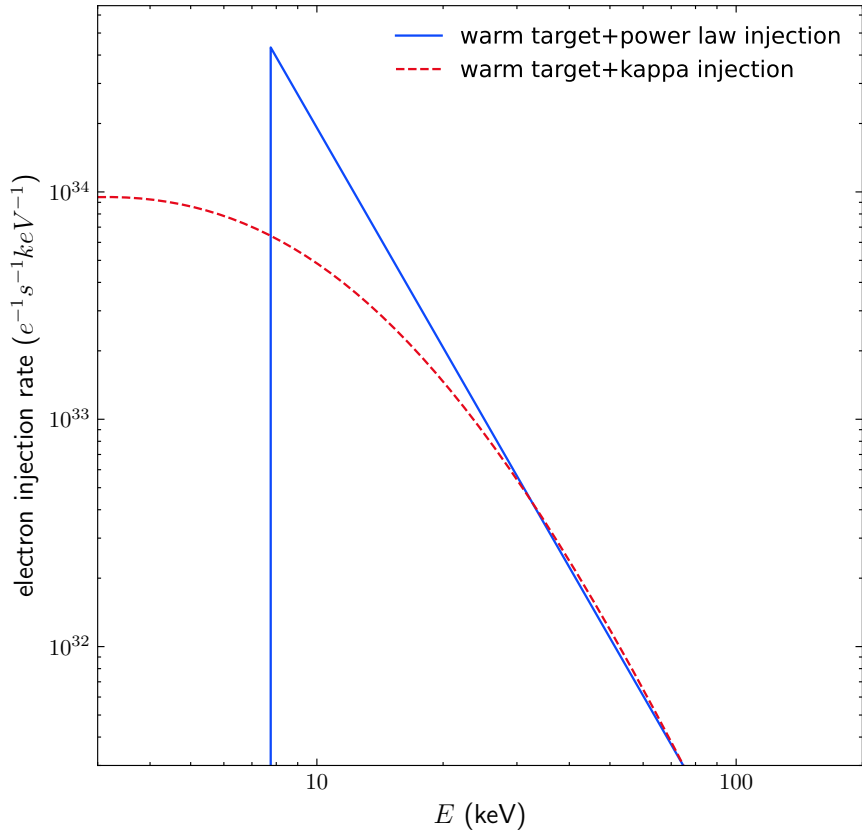


Figure B.2: Inferred electron injection rate as a function of energy for power law electron injection (solid blue) and κ -distributed electron injection (dashed red) from the fit parameters listed in Tab. ??.